

The modeling of
Blood Rheology
in small vessels

by

Matthew Scott

A thesis
presented to the University of Waterloo
in fulfillment of the
thesis requirement for the degree of
Doctor of Philosophy
in
Applied Mathematics

Waterloo, Ontario, Canada, 2005

©Matthew Scott, 2005

I hereby declare that I am the sole author of this thesis. This is a true copy of the thesis, including any required final revisions, as accepted by my examiners.

I understand that my thesis may be made electronically available to the public.

Abstract

Blood is a dense suspension of flexible red blood cells. In response to a background flow, these cells distribute themselves non-uniformly throughout the vessel. As a result, material properties that are well defined in homogeneous fluids, such as viscosity, are no longer so, and depend upon the flow geometry along with the particle properties. Using a simple model that accounts for the steady-state particle distribution in vessel flow, we derive an expression for the effective viscosity of blood and the suspension flow velocity field in a pressure-driven tube flow.

We derive the steady-state particle distribution from a conservation equation with convective flux arising from particle deformation in the flow. We then relate the particle microstructure to the overall flow through a generalized Newtonian stress-tensor, with the particle volume fraction appearing in the expression for the local viscosity. Comparing with experimental data, we show that the model quantitatively reproduces the observed rheology of blood in tube flow.

We reconsider the problem in an alternate geometry corresponding to the flow between two concentric cylinders. The steady-state particle distribution, suspension velocity field and the measured effective viscosity are all very different from their counterparts in tube flow, casting serious doubt upon the practice of using data from a Couette viscometer to parameterize constitutive models applied to vascular blood flow.

Finally, we calculate the effect of random fluctuations in the particle velocity on the averaged behaviour of the particle conservation equation. Using a smoothing method for linear stochastic differential equations, we derive a correction to the free Einstein-Stokes diffusion coefficient that is due to the interaction of the particles with their neighbours.

Acknowledgements

I would like to express my deepest gratitude to Pino Tenti who taught me what a scientist does, and more importantly how a scientist thinks. I would also like to thank Serge D'Alessio who recommended the text by L. G. Leal 'Laminar flow and convective transport processes' which clarified much of this material for me. I appreciate the financial support I received from the Ontario government through the Ontario Graduate Scholarship, assistantships from the Department of Applied Mathematics, as well as the financial support and encouragement of my co-supervisor, Wing-Ki Liu. I am grateful for the many corrections and useful clarifications suggested by Robert Owens and Francis Poulin, and I thank them for their careful reading of the dissertation.

Finally, I would like to thank my lovely wife Mona – after a lot of hard work, dedicating this to her is the easiest thing I've ever done.

The function of a constructional system is not to recreate experience but rather to map it . . . A map is schematic, selective, condensed and uniform. And these characteristics are virtues rather than defects. The map not only summarizes, classifies and systematizes, it often discloses facts we could hardly learn immediately from our explorations . . . This also suggests the answer not only to rampant intellectualism but to many another objection against the abstraction, poverty, artificiality and general unfaithfulness of constructional systems. Let no one complain that the turnpike is not red like the line on the map, that the dotted state boundaries are not visible in the fields, or that the city we arrive at is not a round black dot. Let no one suppose that if a map made according to one scheme of projection is accurate then maps made according to alternative schemes are wrong. And let no one accuse the cartographer of reductionism if his map fails to turn green in the spring.

-Nelson Goodman, *The Revision of Philosophy*

Contents

1	Introduction	1
1.1	Why Study Blood Flow?	1
1.2	Blood and Vascular Circulation	2
1.3	Flow Anomalies	5
1.4	Suspension Microstructure	7
1.5	Outline of the Thesis	8
2	Suspension viscosity	11
2.1	Homogeneous suspensions	11
2.1.1	Dilute suspensions	12
2.1.2	Concentrated suspensions	19
2.2	Multiple-fluid models	23
2.3	Constitutive models	29
2.4	Flow microstructure and local viscosity	32
3	Microstructure	33
3.1	Particle Redistribution	35
3.1.1	Migration of a Fluid Droplet - Chan & Leal 1979	36
3.2	Particle Conservation Equation	47
3.2.1	Steady-state Particle Distribution $\phi^{ss}(\hat{r})$	48
4	Overall suspension flow	52
4.1	Suspension flow and the effective viscosity	52

5	Comparison with experiments	59
5.1	Fitting of incomplete data	59
5.2	Semi-qualitative rheology	62
5.3	Predictive rheology	65
6	Couette geometry	70
6.1	Measuring viscosity	70
6.2	Steady-state rheology in a Couette viscometer	75
6.3	Trouble with constitutive models	83
7	Mean-field diffusion coefficient	86
7.1	Stochastic conservation equation for ϕ	86
7.1.1	Bouret's approximation	87
7.1.2	Conservation equation for $\langle\phi(\mathbf{x}, t)\rangle$	90
7.2	Connection to the empirical $D(\varepsilon, \phi_0)$	96
7.2.1	Semi-empirical derivation of the diffusion rate correction	98
8	Concluding remarks	101
8.1	Including the effect of inertia	102
A	Glossary	106
A.1	Glossary of Terms	106
A.2	Glossary of Symbols	108
A.2.1	Greek	108
A.2.2	Arabic	108
B	Pulsatile velocity field	110
C	Stability of suspension Couette flow	113

List of Tables

1.1	Blood constituents	2
1.2	Red blood cells and plasma properties	3
1.3	Physiology of the circulation	5
2.1	Popular constitutive models in blood rheology	31

List of Figures

1.1	The shape of red blood cells at rest and in flow	3
1.2	Reynolds number in the vasculature	4
1.3	Flow anomalies in blood	6
1.4	Red cell microstructure in low and high shear	7
1.5	Overview of the thesis	8
2.1	Energy dissipation in a dilute suspension	15
2.2	Concentrated polydisperse suspensions	20
2.3	Polydisperse and aggregated monodisperse suspensions	21
2.4	Effective viscosity of a concentrated <i>homogeneous</i> suspension	23
2.5	Core-annular flows	24
2.6	Velocity profile of a core-annular flow - 1	26
2.7	Velocity profile of a core-annular flow - 2	27
2.8	The origin of the stress tensor in the microscopic exchange of momentum	30
3.1	The relationship between microstructure and the apparent viscosity	34
3.2	Impossibility of cross-stream migration of a sphere in creeping flow	36
3.3	Coordinate system of Chan and Leal	38
3.4	Predicted droplet shape compared to red blood cells in flow	43
3.5	Steady-state particle distribution	49
3.6	Density plot of the steady-state distribution	50
4.1	Velocity profile of a concentrated suspension in tube flow	55
4.2	Effective viscosity of a concentrated suspension in tube flow	56

4.3	Contrast with the standard picture of blood rheology	57
5.1	Using ε as a fitting parameter-Wall shear stress	60
5.2	Using ε as a fitting parameter-Velocity profiles	61
5.3	Comparison with the data of Fahraeus and Lindqvist	62
5.4	Shear-thinning and cell hardening	63
5.5	The effect of shear on the volume fraction dependent viscosity	64
5.6	Empirical diffusion coefficient	67
5.7	Predictive comparisons	68
6.1	Various viscometers	71
6.2	A Couette viscometer	76
6.3	Steady-state particle distribution of a dilute suspension	78
6.4	Steady-state particle and velocity distribution of a concentrated suspension	80
6.5	Potential instability in Couette flow of concentrated suspensions	81
6.6	Effective viscosity of Couette flow	82
6.7	Parameterization of a constitutive model	84
7.1	Anisotropic diffusivity in tube flow	95
7.2	Velocity fluctuations due to particle-particle collisions	97
8.1	High-Reynolds number rise in the effective viscosity	103
8.2	Particle drift <i>away</i> from the axis at high Reynolds number	104
C.1	A Couette viscometer	114

Chapter 1

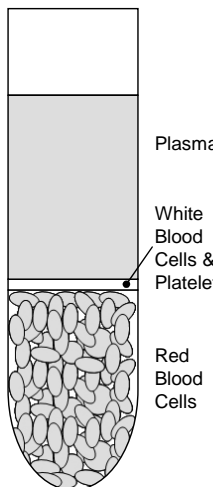
Introduction

1.1 Why Study Blood Flow?

Blood is essential to maintain life. It transports oxygen and nutrients to all parts of the body, relays chemical signals and moves metabolic waste to the kidneys for elimination. Yet despite more than 150 years of close study, a concise, predictive model of blood flow is still lacking.

A quantitative model of blood flow is important not only as it relates to clinical diagnosis of disease, but as an integral component of models of more complex structures like the brain. Furthermore, proper design of artificial organs demands a thorough understanding of blood rheology in order to avoid flow stagnation and clot formation.

In this introductory chapter, we provide some physiological background to give context to the theoretical model developed in later chapters. We touch upon unexpected flow behaviours of blood and discuss the role of flow-induced red blood cell structures that may account for experimental observations. Finally, we conclude with an overview of the remaining chapters and an outline of the thesis.



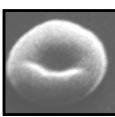
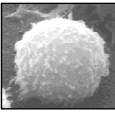
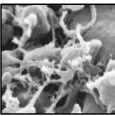
Cell Type	Shape	Number Density (per mm ³)	% Volume of Blood
Red Blood Cells Erythrocytes	Biconcave Disk 	$4-6 \times 10^6$	45
White Blood Cells Leucocytes	Spherical 	$4-11 \times 10^3$	1
Platelets	Various 	$250-500 \times 10^3$	

Table 1.1: **Blood constituents.** Data taken from [15].

1.2 Blood and Vascular Circulation

Blood is a dense suspension of blood cells and platelets. The dominant constituent is red blood cells which make up 45% by volume of whole blood. By contrast, the remaining particulate, white blood cells and platelets, occupy less than 1% by volume (Table 1.1).

Under normal flow conditions (*i.e.* in the absence of a wound or narrow constriction), the flow of blood is dominated by the interaction of the red blood cells with the vessel walls and the surrounding medium, called plasma, which is essentially water made slightly more viscous and dense by the presence of dissolved proteins (Table 1.2). Notice the low sedimentation rate (~ 1 cm/hr) of red blood cells in plasma. The flow rate is high and the vessel length is small in the vasculature of the body, so the red cells have very little time to sediment, and as a first approximation we may consider red blood cells as neutrally buoyant.

At rest, red blood cells are biconcave disks roughly $8\mu\text{m}$ in diameter and $2.5\mu\text{m}$ across at their thickest point. The cell membrane is quite flexible so that in flow, the red blood cell shape is less well defined, resembling a dimpled fluid droplet (Figure 1.1).

Red Blood Cells (Erythrocytes)		Plasma	
Surface Area:	138 μm^2	Content: <i>Water</i>	92 g / 100 mL
Volume:	94 μm^3	<i>Proteins</i>	7 g / 100 mL
Membrane Tension:	1×10^{-5} N / m	<i>Inorganic Salts</i>	1 g / 100 mL
Specific Gravity:	1.1	Viscosity (37°C):	1.2 mN s m ⁻²
Sedimentation Rate:	3 μm / s	Specific Gravity:	1.03

Table 1.2: Red blood cells and plasma properties. Data taken from [14] and [15].

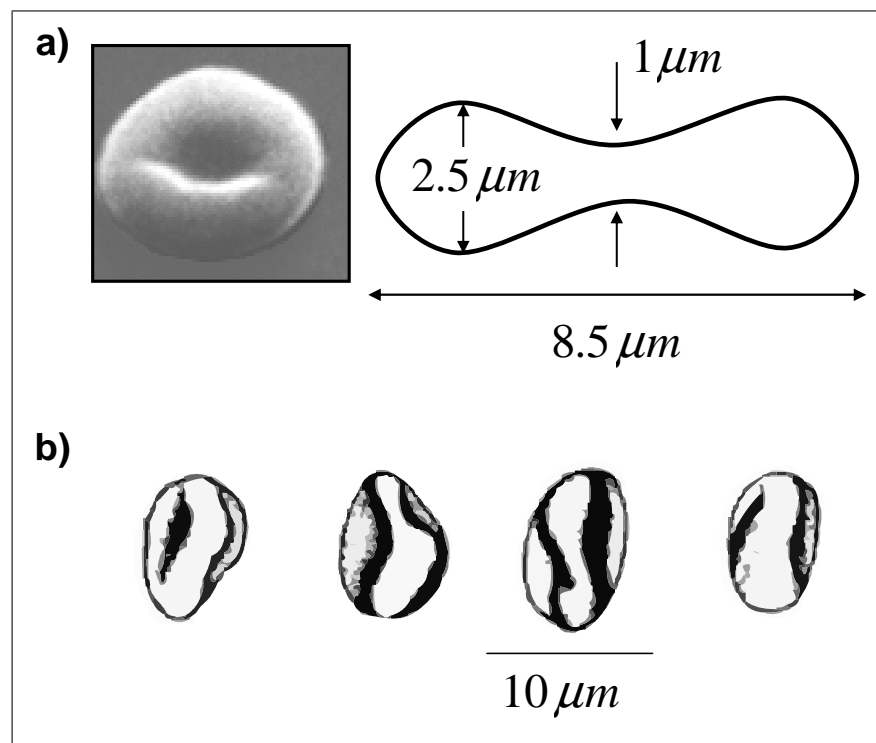


Figure 1.1: **The shape of red blood cells.** a) At rest the red blood cell is a biconcave disk. b) In flow, the blood cell looks more like a dimpled fluid droplet [40, 41].

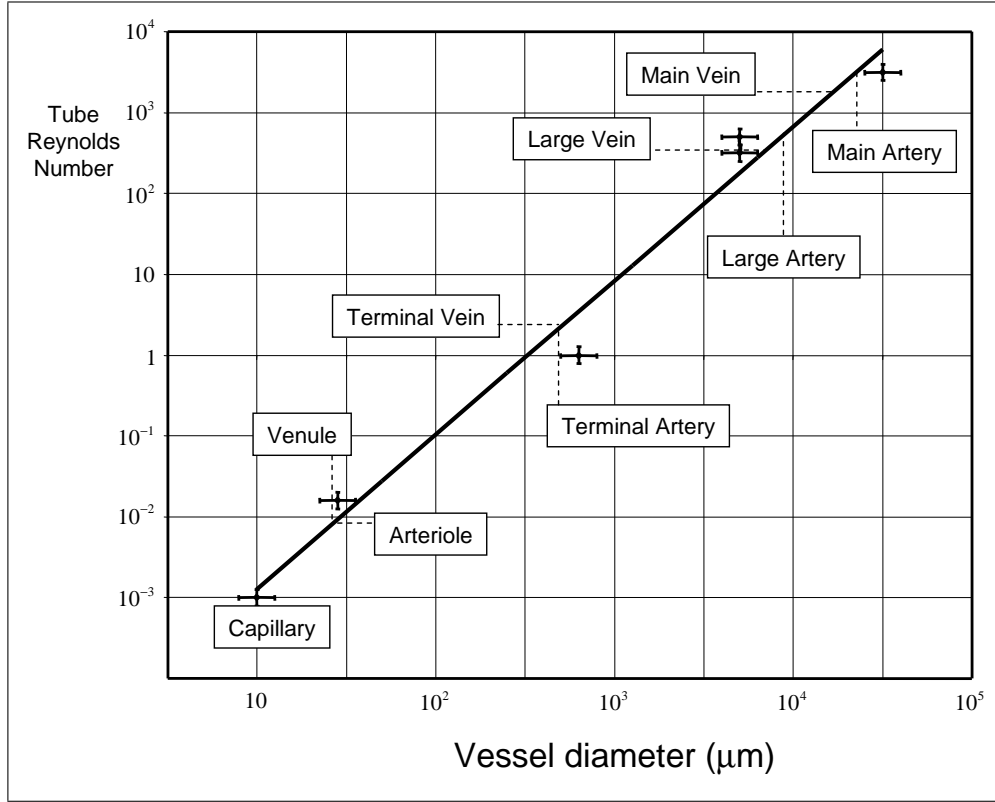
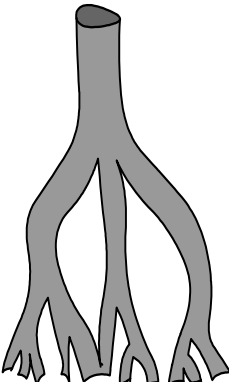


Figure 1.2: **Reynolds number in the vasculature.** Redrawn from [76].

Blood flow conditions vary greatly throughout the body, with the tube Reynolds number decreasing linearly with decreasing vessel diameter (Figure 1.2 and Table 1.3). Here the Reynolds number is defined in terms of the maximum centerline velocity V_{\max} , the vessel radius R , the density of the plasma ρ_0 and the plasma (dynamic) viscosity η_0 as

$$\text{Re} = \frac{V_{\max} 2R \rho_0}{\eta_0}.$$

In the present study, we focus upon the laminar flow regime thereby restricting our attention to flow in vessels with diameters $< 500 \mu\text{m}$. It is precisely under these conditions that blood deviates most from the flow behaviour of a Newtonian fluid, giving rise to observed flow anomalies.



Vessel	Internal Diameter (cm)	Peak Velocity (cm/s)	Wall Shear Rate (s^{-1})	Peak Reynolds Number
Ascending Aorta	1.5	120	320	4500
Descending Aorta	1.3	105	323	3400
Abdominal Aorta	0.9	55	244	1250
Femoral Artery	0.4	100	1000	1000
Arteriole	0.005	0.75	600	0.09
Capillary	0.0006	0.07	467	0.001

Table 1.3: **Physiology of the circulation.** Data taken from [20] and [15].

1.3 Flow Anomalies

A homogeneous isothermal Newtonian fluid is characterized by a constant viscosity, which is an intrinsic material property of the fluid. The viscosity is a measure of the fluid's resistance to flow, and does not change with confining geometry or flow conditions.

Blood is not a homogeneous fluid; it is a suspension. As a result, the viscosity is no longer a well-defined material property, but rather must be defined as an *observed* resistance to flow. Expressed in this way, the apparent viscosity of blood will depend upon the confining geometry, decreasing with decreasing vessel diameter; *i.e.*, it is easier to move blood through a narrow vessel. This is the most famous flow oddity associated with blood, and is called the Fahraeus-Lindqvist effect (Figure 1.3a).

The suspended blood cells accumulate at the axis in response to flow, resulting in a blunting of the velocity profile near the axis in contrast to the parabolic profile observed in homogeneous fluids (Figure 1.3b). As we shall discuss in the next chapter, this accumulation of blood cells along the axis leads to a favorable decrease in the suspension viscosity. The final flow anomaly we wish to highlight is the decrease in blood viscosity with increased shear rate, a characteristic called *shear-thinning* (Figure 1.3c).

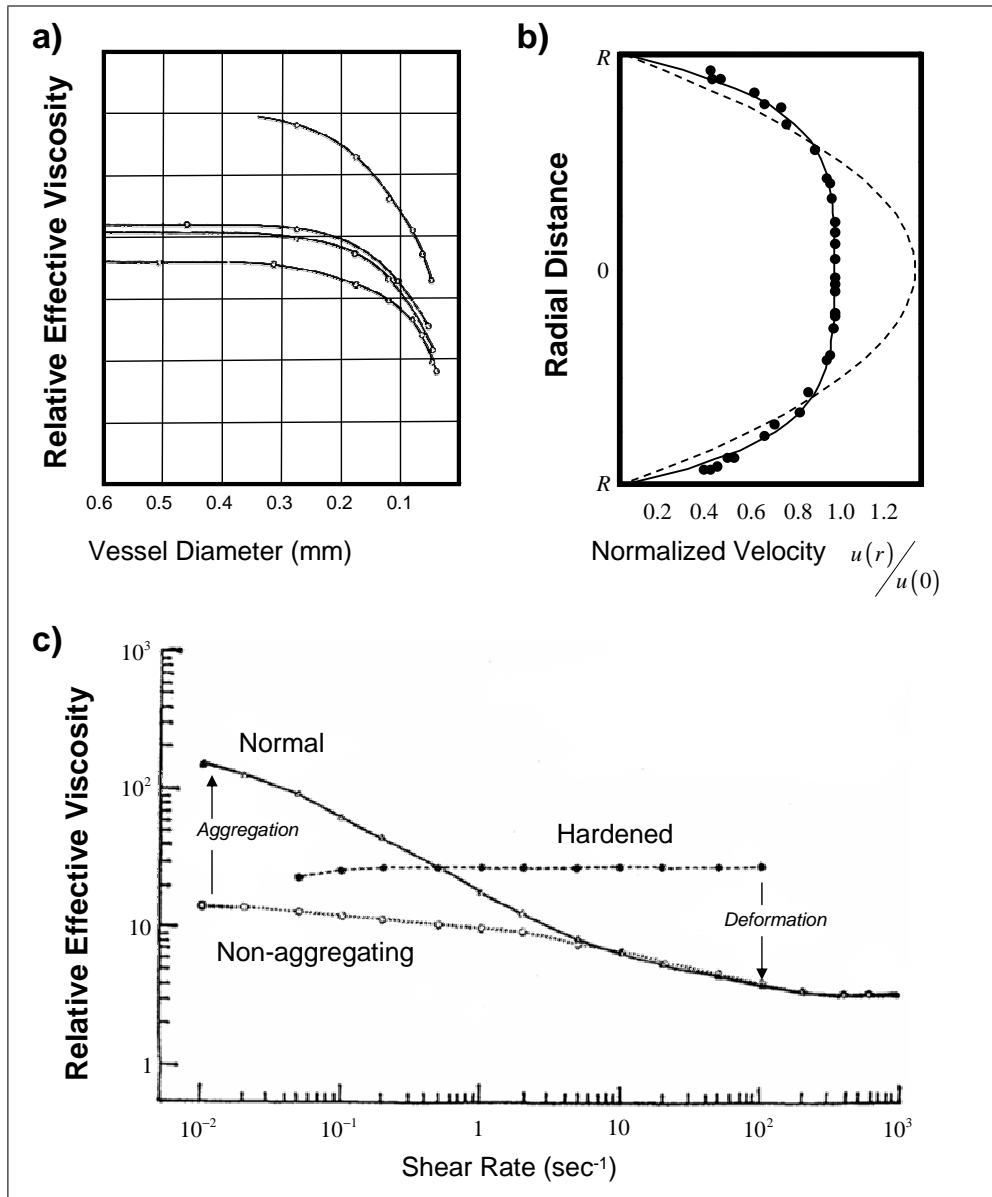


Figure 1.3: **Flow anomalies in blood.** a) **The Fahraeus-Lindqvist effect:** the apparent viscosity of blood *decreases* with decreasing vessel diameter [33]. b) **Non-parabolic velocity profile:** The velocity profile for flowing blood is blunted close to the tube axis. The dashed line shows a parabolic profile with the same volumetric flow rate [39]. c) **Shear-thinning:** The apparent viscosity of blood decreases with increasing shear rate [21].

1.4 Suspension Microstructure

The microscopic arrangement of the red cells in the vessel flow plays a leading role in the theoretical development of later chapters. We envision two qualitatively different microstructures in the flow: an extended network of red blood cell aggregates (Figure 1.4a) and a tightly packed core of blood cells surrounded by a plasma layer (Figure 1.4b). Shear gradients in the flow break-up aggregated clusters and individual red cells tend to migrate to regions of lower shear gradients. The background flow rearranges the suspended particles, and the distribution of particles, in turn, determines the suspension flow field and observed rheology. The present work will focus upon the behaviour of blood moving swiftly through narrow vessels where the dominant microstructure is a core of blood cells accumulated along the vessel axis.

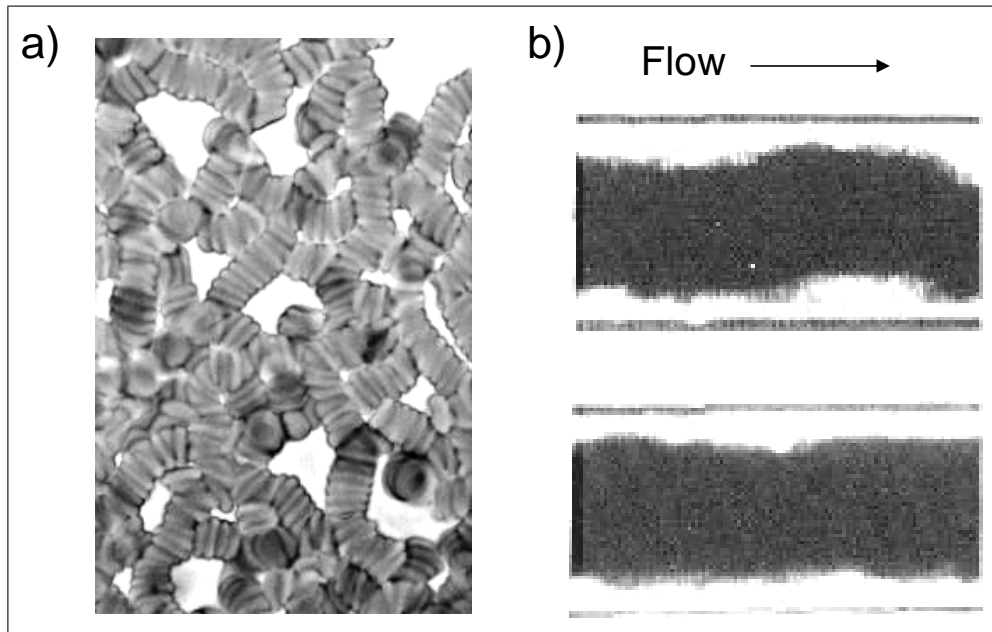


Figure 1.4: **Red cell microstructure in low and high shear.** **a)** An extended network of *rouleaux* at low shear. **b)** A dense core of red blood cells at high shear [1].

1.5 Outline of the Thesis

A broad overview of the thesis is presented diagrammatically in Figure 1.5. The flow induces a rearrangement of the red blood cells, with the red cell volume fraction ϕ governed by a conservation equation. The inhomogeneous distribution of particles leads to differences in the local properties of the suspension. We use a generalized Newtonian shear-stress¹ tensor $\tau(\phi)$ to relate the particle distribution to the overall suspension flow field \vec{u} by defining a local model viscosity η_ϕ .

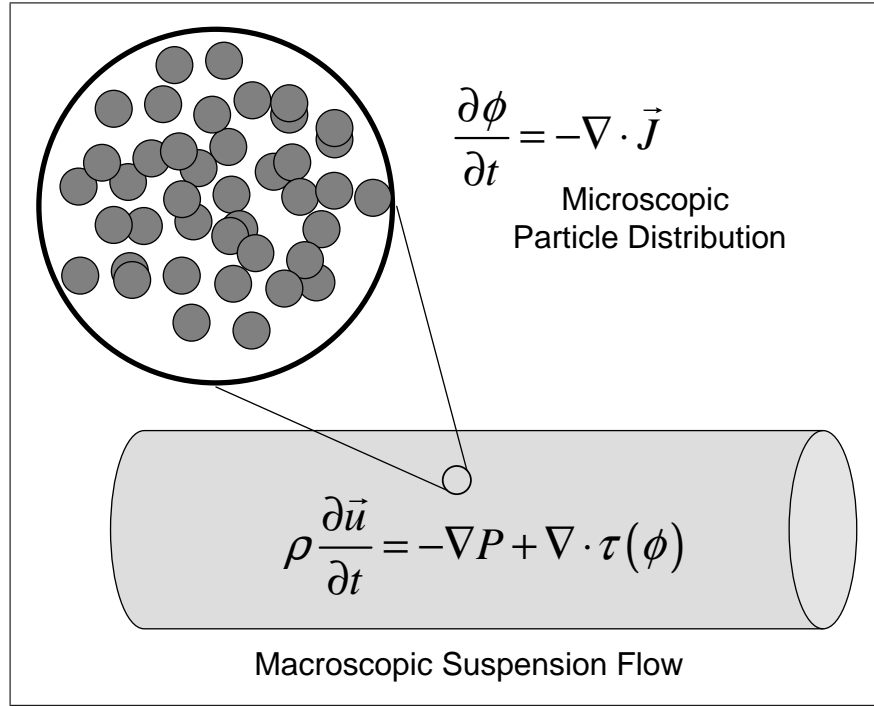


Figure 1.5: **Schematic overview of the thesis.** The overall flow \vec{u} is connected to the microstructure by a local shear-stress tensor $\tau(\phi)$.

¹Also called the *extra-stress* or *deviatoric stress* tensor.

Considering each chapter in more detail:

Chapter 2 - Suspension viscosity

Here we review past work, outlining three popular methods of approach to the modeling of suspension rheology. We begin with the seminal work of Einstein describing the viscosity of a homogeneous suspension. We then consider layered fluids and core-annular flows. Finally, following a brief discussion of constitutive models, we close by placing the present study in the context of past work.

Chapter 3 - Microstructure

Beginning with a qualitative view of low and high shear blood flow, we take advantage of the resemblance of a red blood cell in flow to an immiscible fluid droplet and use the results of Chan and Leal [18] to model the blood cell cross-stream migration velocity. The convective flux of particles toward the axis naturally leads to a characterization of the particle volume fraction in terms of a conservation equation. With a suitable choice for the diffusive flux, the steady-state particle distribution is calculated. It is a Gaussian parameterized by the initial particle volume fraction ϕ_0 and a dimensionless constant ε , which acts as a model *Péclet* number.

Chapter 4 - Overall suspension flow

Using the viscosity expression of Roscoe [75] derived for concentrated homogeneous suspensions, we replace the homogeneous volume fraction ϕ by our inhomogeneous distribution function $\phi(r)$ thereby arriving at an expression for the *local* suspension viscosity. Postulating a generalized Newtonian stress tensor $\tau = \eta_\phi(r) \frac{\partial u}{\partial r}$, we are able to connect the microscopic particle distribution to the macroscopic flow, calculating the suspension velocity field and corresponding flow rate from the creeping flow equations solved with non-constant viscosity. Comparing the suspension flow rate to the flow rate of an analogous homogeneous fluid, we define an effective viscosity for the flow as measured by a capillary viscometer.

Chapter 5 - Comparison with experiments

Having described the suspension flow with a minimum of parameters, we proceed to vindicate the model assumptions through comparison with experimental data. Leaving ε as a fitting parameter, we estimate wall shear-stress from incomplete imaging data. Next, using experimentally determined flow rates, we fix ε and successfully reconstruct the entire suspension flow field. Returning to the definition of ε in terms of physical parameters, we qualitatively reproduce the Fahraeus-Lindqvist effect and shear-thinning. Finally, defining an empirical diffusion coefficient $D(\varepsilon, \phi_0)$, we successfully predict *in vitro* and *in vivo* blood velocity flow fields from the centerline velocity u_m , the tube radius R and the hematocrit ϕ_0 alone.

Chapter 6 - Couette geometry

Couette viscometers are often used to carry out blood rheology experiments. We repeat our derivation in this new flow geometry and arrive at an essentially different relationship between physical parameters and the observed rheology, casting doubt upon the practice of validating *in vivo* models using Couette data.

Chapter 7 - Mean-field diffusion coefficient

The empirical diffusion coefficient $D(\varepsilon, \phi_0)$ of Chapter 5 is put on a more solid physical foundation by considering the microscopic velocity fluctuations in the particle conservation equation and their effect on the mean particle distribution.

Chapter 8 - Concluding remarks

We conclude with a summary of future work – suggesting a simple method for including inertial effects in the present model.

Chapter 2

Suspension viscosity

Blood is a suspension and it is this feature that leads to its unexpected flow behaviour. To develop a model for blood rheology and to understand how suspended particles affect the overall suspension flow, it is important to review successful past models. In this chapter, we review the classic work of Einstein who showed that in a dilute homogeneous suspension of hard spheres, the effective viscosity is always *increased* by the presence of particles. If we allow inhomogeneities in the particle distribution - in particular, if we consider the tube flow of a compact core surrounded by a deplete outer layer - we see a dramatic *decrease* in the overall viscosity of the flow. The central difficulty in modeling suspension flow is how to combine the increased viscosity due to the particulate with the decreased viscosity associated with structured flow, all in a physically consistent fashion.

2.1 Homogeneous suspensions

The study of homogeneous suspensions has a long history beginning with the seminal work of Einstein showing that the effective viscosity η of a dilute suspension of hard spheres grows linearly with the volume fraction of particulate ϕ according to: $\eta = \eta_0 (1 + \frac{5}{2}\phi)$, where η_0 is the solvent viscosity. Many ideas appear in this work, developed by others much later, laying the foundation for a statistical mechanical description of suspension rheology [44]. We present a complete derivation of Einstein's result due to G. K. Batchelor [6] that relaxes the restriction to hard-sphere suspensions, and therefore also contains the work of G. I.

Taylor on the viscosity of a suspension of liquid droplets [86]. We go on to generalize these results to concentrated suspensions using the phenomenological effective-media argument of Roscoe [75].

2.1.1 Dilute suspensions

Dilute homogeneous suspensions of spheres are the simplest of all suspensions to investigate. Nevertheless, there are still subtle questions about the meaning of viscosity in a suspension, which by definition has a discrete distribution of viscosity throughout. Einstein had the insight to consider energy dissipation in the suspension and ask what viscosity is required in a homogenized analogous fluid to achieve the same dissipation. We present the derivation in detail because it serves to illustrate several useful ideas that resurface in later chapters; specifically the representation of *microscopic* inhomogeneities by a homogenized bulk parameter. Furthermore the initial steps of the derivation are closely followed by Chan and Leal [18] in their work on deformable particle migration (discussed in chapter 3) that underlies the main results of this dissertation. Finally, in the next chapter we propose to model a red blood cell as an immiscible fluid droplet and the meaning of some physical parameters is unclear in that approximation. For example, a fluid drop has a well-defined viscosity, but what about the internal viscosity of a red blood cell? Is it enough to burst the cell and measure the viscosity of the contents? Having clear insight into where the internal viscosity appears in the derivation, and the role it plays in the subsequent development, will aid in justifying future assumptions.

We begin by considering a small spherical particle suspended in a purely straining flow $e_{ij}x_j$ with background pressure P (Figure 2.1). The components of the velocity u_i and the pressure p are given by,

$$\begin{aligned} u_i &= u'_i + e_{ij}x_j, \\ p &= p' + P, \end{aligned}$$

where u'_i and p' are the perturbations due to the presence of the suspended particle on the solvent flow and pressure, respectively. The coordinate variables are given by x_j with the origin at the center of the spherical particle and summation over repeated indices implied.

The components of the rate-of-strain tensor are represented by e_{ij} with the usual meaning

$$e_{ij} = \frac{1}{2} \left(\frac{\partial u_j}{\partial x_i} + \frac{\partial u_i}{\partial x_j} \right).$$

Since we are assuming the far-field flow is simple linear shear, the e_{ij} are constant and $e_{jj} = 0$. Far from the particle, we require that the disturbances vanish, *i.e.*

$$\lim_{|\mathbf{x}| \rightarrow \infty} u'_i = \lim_{|\mathbf{x}| \rightarrow \infty} p' = 0.$$

We explicitly require that the shape of the particle remains spherical, and that departures from symmetry have negligible effects. We further assume the particle is made of an incompressible Newtonian fluid with viscosity $\tilde{\eta}_0$. The surface of the particle is at $|\mathbf{x}| \equiv r = a$, with $\mathbf{n} \cdot \mathbf{u} = 0$ at the interface. The velocity and the tangential stress¹ must be continuous across the interface, so that

$$\begin{aligned} u_i &= u'_i + e_{ij}x_j = \tilde{u}_i, \\ \epsilon_{kli}n_l n_j (S_{ij} - \tilde{S}_{ij}) &= 0, \end{aligned} \tag{2.1}$$

at $r = a$. Here the tilde indicates functions *within* the particle, ϵ_{ijk} is the alternating tensor², \mathbf{n} is the outward unit normal at the particle surface and \mathbf{S} is the stress tensor defined below.

Assuming small particle Reynolds number, we have

$$\frac{|e_{ij}| a^2 \rho_0}{\eta_0} \ll 1,$$

and so both the disturbance flow and the fluid within the particle are characterized by the creeping flow³ equations,

$$\begin{aligned} \nabla p' &= \eta_0 \nabla^2 \mathbf{u}', \\ \nabla \tilde{p} &= \tilde{\eta}_0 \nabla^2 \tilde{\mathbf{u}}, \end{aligned}$$

¹We use S in place of the more traditional σ , reserving σ for the interfacial tension in chapter 3.

² $\epsilon_{ijk} = 0$ unless $\{i, j, k\}$ are all different, and $+1(-1)$ if $\{i, j, k\}$ are (not) in cyclic order.

³Also called *Stokes flow*.

with $\nabla \cdot \mathbf{u}' = \nabla \cdot \tilde{\mathbf{u}} = 0$. The solution of the governing equations subject to the boundary conditions (2.1) can be computed exactly [6], although we shall only require the disturbance pressure p' and velocity u'_i , namely

$$p' = -\eta_0 \left(\frac{2\eta_0 + 5\tilde{\eta}_0}{\eta_0 + \tilde{\eta}_0} \right) \frac{a^3}{r^5} e_{ij} x_i x_j$$

$$u'_i = -\frac{\tilde{\eta}_0}{(\eta_0 + \tilde{\eta}_0)} \frac{a^5}{r^5} e_{ij} x_j + \left(\frac{5\tilde{\eta}_0}{2(\eta_0 + \tilde{\eta}_0)} \frac{a^5}{r^7} - \frac{(2\eta_0 + 5\tilde{\eta}_0) a^3}{2(\eta_0 + \tilde{\eta}_0) r^5} \right) e_{jkl} x_i x_j x_k. \quad (2.2)$$

We consider a volume of suspension V bounded by a surface A far enough from the particles that u'_i and p' both vanish at the boundary (Figure 2.1a). The stress tensor in the fluid is

$$S_{ij} = -P\delta_{ij} + 2\eta_0 e_{ij} + S'_{ij},$$

where

$$S'_{ij} = -p'\delta_{ij} + \eta_0 \left(\frac{\partial u'_j}{\partial x_i} + \frac{\partial u'_i}{\partial x_j} \right)$$

is the contribution to the stress due to the presence of the suspended particles. From a macroscopic point of view, on length scales very large compared to the length scales of the suspended particles, we can represent the suspension as a homogeneous fluid with effective viscosity η . The stress tensor in this representative fluid is

$$S_{ij} = -P\delta_{ij} + 2\eta e_{ij}.$$

We must find a constraint on η that will allow the effective viscosity to be expressed in terms of known quantities. Following Einstein [29, 30], we consider the rate of dissipation of mechanical energy in our suspension and in the macroscopically equivalent homogenized fluid. To avoid thorny issues of convergence associated with integration over volume, we consider the work done on the bounding surface at A . By definition, the stress tensor is the force per unit area acting on a plane of fluid, so that $F_i dA = S_{ij} n_j dA$ is the i^{th} component of the force vector acting on the area element dA . The rate of work done on that element is $u_i F_i dA$, and since we assume $u'_i = 0$ at the boundary, we have that the total rate of work W done on the bounding surface A is (Figure 2.1c),

$$W = \int_A e_{ik} x_k S_{ij} n_j dA = e_{ik} \int_A (-P\delta_{ij} + 2\eta_0 e_{ij} + S'_{ij}) x_k n_j dA.$$

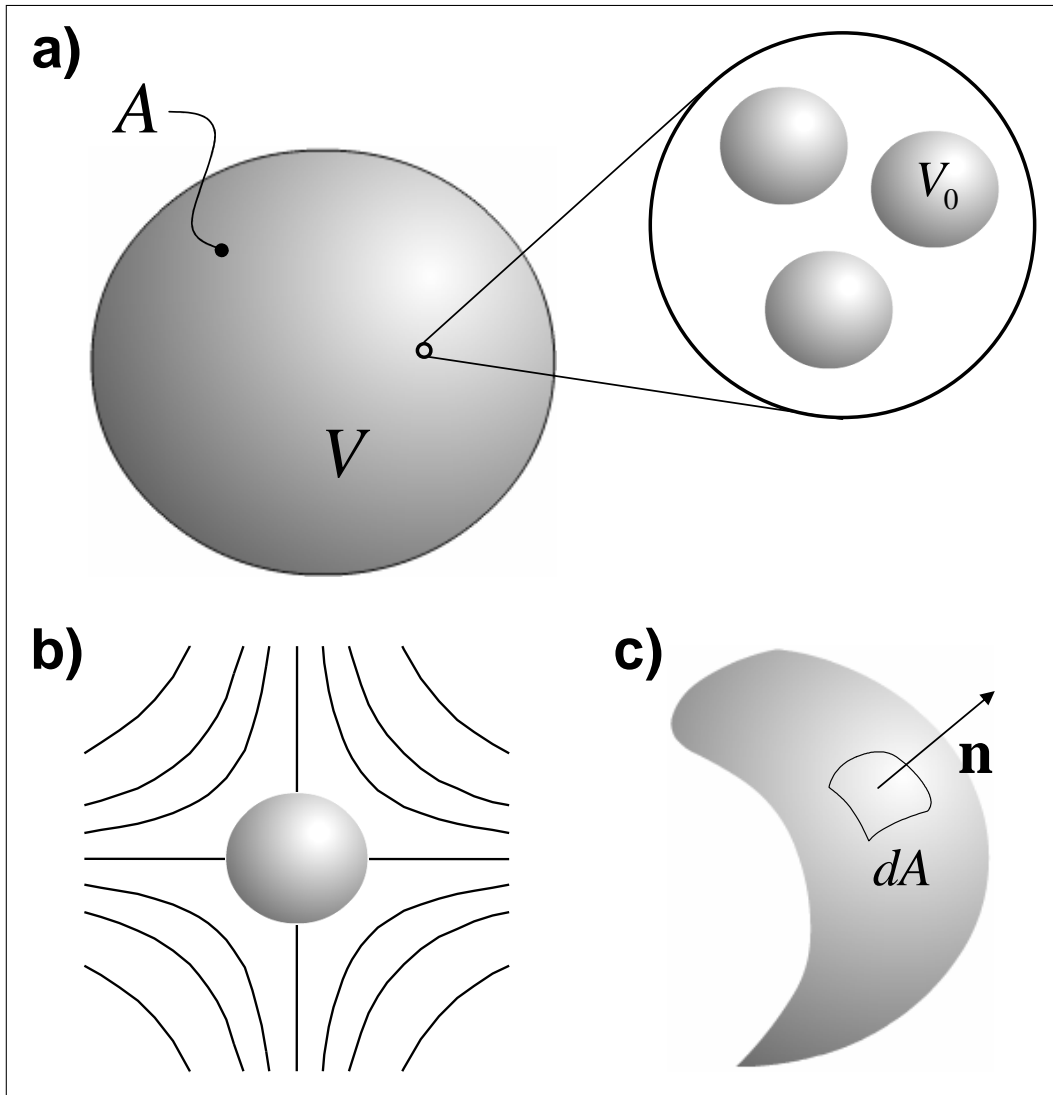


Figure 2.1: **Energy dissipation in a dilute suspension.** a) We bound a suspension of n identical microscopic particles by a macroscopic surface A . b) The flow around each particle is purely straining. c) \mathbf{n} is the outward unit normal to the area element dA .

In our analogous homogeneous fluid,

$$W = \int_A e_{ik} x_k S_{ij} n_j dA = e_{ik} \int_A (-P \delta_{ij} + 2\eta e_{ij}) x_k n_j dA.$$

Equating these two expressions, the constraint on η is thus,

$$2(\eta - \eta_0) e_{ik} \int_A e_{ij} x_k n_j dA = e_{ik} \int_A S'_{ij} x_k n_j dA.$$

Using the divergence theorem, and recalling that the e_{ij} are constant, we find

$$\int_A e_{ij} x_k n_j dA = \int_V \frac{\partial (e_{ij} x_k)}{\partial x_j} dV = e_{ij} \delta_{kj} \int_V dV = e_{ik} V,$$

and the constraint is simplified to read

$$2(\eta - \eta_0) e_{ik} e_{ik} V = e_{ik} \int_A S'_{ij} x_k n_j dA. \quad (2.3)$$

The last term $e_{ik} \int_A S'_{ij} x_k n_j dA$ represents the contribution to the energy dissipation due to the presence of the particles. Applying the divergence theorem to this term, we can discriminate between contributions from the solvent and contributions from the n identical particles of individual volume V_0 ,

$$\int_A S'_{ij} x_k n_j dA = \int_V \frac{\partial (S'_{ij} x_k)}{\partial x_j} dV = \int_{V-nV_0} \frac{\partial (S'_{ij} x_k)}{\partial x_j} dV + n \int_{V_0} \frac{\partial (S'_{ij} x_k)}{\partial x_j} dV. \quad (2.4)$$

The first term in the right-hand side is the volume integral over the solvent, and the second term is the volume integral over each of n particles with volume $V_0 = \frac{4}{3}\pi a^3$. The divergence of the stress tensor $\frac{\partial S'_{ij}}{\partial x_j}$ vanishes by virtue of the governing equations; hence,

$$\begin{aligned} \frac{\partial S'_{ij}}{\partial x_j} &= \frac{\partial}{\partial x_j} \left(-p' \delta_{ij} + \eta_0 \left(\frac{\partial u'_j}{\partial x_i} + \frac{\partial u'_i}{\partial x_j} \right) \right) \\ &= -\frac{\partial p'}{\partial x_i} + \eta_0 \left(\frac{\partial^2 u'_j}{\partial x_j \partial x_i} + \frac{\partial^2 u'_i}{\partial x_j \partial x_j} \right) \end{aligned}$$

$$\begin{aligned}
&= -\frac{\partial p'}{\partial x_i} + \eta_0 \left(\frac{\partial}{\partial x_i} \left(\frac{\partial u'_j}{\partial x_j} \right) + \frac{\partial^2 u'_i}{\partial x_j \partial x_j} \right) \\
&= -\frac{\partial p'}{\partial x_i} + \eta_0 \frac{\partial^2 u'_i}{\partial x_j \partial x_j} \quad \left(\nabla \cdot \mathbf{u}' = 0 \Leftrightarrow \frac{\partial u'_j}{\partial x_j} = 0 \right) \\
&= -\frac{\partial p'}{\partial x_i} + \eta_0 \frac{\partial^2 u'_i}{\partial x_j \partial x_j} = 0 \quad (-\nabla p' + \eta_0 \nabla^2 \mathbf{u}' = 0)
\end{aligned}$$

since the last line is simply the i^{th} component of the creeping flow equations. (Note that in the line previous we use the fact that the disturbance flow is divergence-free to write $\frac{\partial u'_j}{\partial x_j} = 0$.)

Re-writing (2.4) using $\frac{\partial S'_{ij}}{\partial x_j} = 0$ and converting the last term back to an integral over the surface of each particle,

$$\int_A S'_{ij} x_k n_j dA = \int_{V-nV_0} S'_{ij} \delta_{jk} dV + n \int_{A_0} S'_{ij} x_k n_j dA.$$

We are now able to determine constraint equation (2.3) explicitly:

$$\begin{aligned}
2(\eta - \eta_0) e_{ik} e_{ik} V &= e_{ik} \int_A S'_{ij} x_k n_j dA \\
&= e_{ik} \int_{V-nV_0} S'_{ik} dV + n e_{ik} \int_{A_0} S'_{ij} x_k n_j dA \\
&= e_{ik} \int_{V-nV_0} \left(-p' \delta_{ik} + \eta_0 \left(\frac{\partial u'_k}{\partial x_i} + \frac{\partial u'_i}{\partial x_k} \right) \right) dV + n e_{ik} \int_{A_0} S'_{ij} x_k n_j dA \\
&= e_{ik} \int_{V-nV_0} \left(\eta_0 \left(\frac{\partial u'_k}{\partial x_i} + \frac{\partial u'_i}{\partial x_k} \right) \right) dV + n e_{ik} \int_{A_0} S'_{ij} x_k n_j dA.
\end{aligned}$$

In the last line we have used the fact that $e_{ii} = 0$. From the symmetry in the flow, it is clear that $\frac{\partial u'_i}{\partial x_k} = \frac{\partial u'_k}{\partial x_i}$, so that with a final application of the divergence theorem, we write

$$2(\eta - \eta_0) e_{ik} e_{ik} V = n e_{ik} \int_{A_0} (S'_{ij} x_k n_j - 2\eta_0 u'_i n_k) dA,$$

where now the integral is over the surface of *a single particle only* and the negative sign comes from switching the inward unit normal at the control surface to the outward normal on the particle surface. We can evaluate this integral explicitly using the disturbance velocity and pressure (2.2), with the result

$$2(\eta - \eta_0) e_{ik} e_{ik} V = n e_{ik} \left[V_0 \left(\frac{2\eta_0 + 5\tilde{\eta}_0}{\eta_0 + \tilde{\eta}_0} \right) e_{ik} \right],$$

or, with $\phi = \frac{nV_0}{V}$,

$$\boxed{\eta = \eta_0 \left(1 + \phi \left(\frac{\eta_0 + \frac{5}{2}\tilde{\eta}_0}{\eta_0 + \tilde{\eta}_0} \right) \right)}. \quad (2.5)$$

In the limit of high internal viscosity, $\tilde{\eta}_0 \rightarrow \infty$, which for *undeformable* particles is equivalent to considering a suspension of *solid* spheres, we recover Einstein's relation,

$$\eta = \eta_0 \left(1 + \frac{5}{2}\phi \right),$$

(as we should).

The method of Einstein has been extended and generalized by many authors. Of particular relevance is the work of Jeffery [49] calculating the effective viscosity of a dilute suspension of ellipsoidal particles. His analysis leads to an expression in analogy with (2.5) above,

$$\eta = \eta_0(1 + b\phi),$$

where b is the *shape factor* that depends upon the eccentricity of the ellipsoid, decreasing from $\frac{5}{2}$ as the particle becomes more elongated. Considering a solid-like, viscoelastic sphere in linear shear flow, Goddard and Miller [36] recover Jeffery's result, but with the shape factor as a function of the imposed shear rate $\dot{\gamma}$ and the shear modulus of the particles G_p [69],

$$\eta = \eta_0(1 + b(\dot{\gamma})\phi) = \eta_0 \left(1 + \left[\frac{\frac{5}{2} \left(1 - \frac{3}{2} \frac{\eta_0^2 \dot{\gamma}^2}{G_p^2} \right)}{\left(1 + \frac{9}{4} \frac{\eta_0^2 \dot{\gamma}^2}{G_p^2} \right)} \right] \phi \right). \quad (2.6)$$

Consequently, their calculated effective viscosity exhibits 'shear-thinning' dependent upon particle deformability. We shall return to this point in Chapter 5 when we review experimental data on blood flow.

One essential point that we wish to emphasize is that microscopically the viscosity varies from point-to-point in the suspension: η_0 in the solvent and $\tilde{\eta}_0$ in the suspended droplets. Nevertheless, from a macroscopic vantage, this discrete distribution of viscosity is blurred into an *effective* material property of the suspension. The interplay between *micro* and *macro* descriptions, the smearing-out of detailed information to derive bulk (observable) properties, will be a dominant theme in coming chapters. The approximation of a discrete distribution of a great many particles or molecules by a handful of continuous parameters is essential in the development of useful models of physical phenomena, but representing the averaged microscopic dynamics by the field equations of fluid mechanics comes at the price of neglecting *micro*-scale fluctuations. We will return to this point in section 2.3 when we discuss constitutive models, and again in chapter 7 when we consider the effect of blood cell velocity fluctuations in more detail.

In principle, the approach outlined here can be applied to concentrated suspensions, with strange shapes and complex interface dynamics [7, 23, 44, 51, 65], but the calculations are formidable and any constraints or inhomogeneities in the particle distribution make the calculations virtually intractable. Instead, we follow the phenomenological approach of Roscoe [75], generalizing the results of Taylor and Einstein, (2.5), to concentrated suspensions.

2.1.2 Concentrated suspensions

At infinite dilution, in the absence of inter-particle interactions, the effective viscosity of a suspension of solid spheres obeys Einstein's relation above,

$$\eta \sim \eta_0 \left(1 + \frac{5}{2}\phi \right) \quad (\phi \rightarrow 0), \quad (2.7)$$

Roscoe [75] considered a *polydisperse*⁴ suspension with a collection of small spheres of different sizes occupying a volume fraction ϕ (Figure 2.2). Suppose that to this suspension one adds some large particles - large enough that from the point of view of the added particles, the suspension of small particles behaves like a homogeneous fluid with viscosity η . The large spheres occupy a volume fraction ϕ_L , and the total volume fraction occupied

⁴*Polydisperse*: Having a wide distribution of particle size. *Monodisperse*: Having a single particle size.

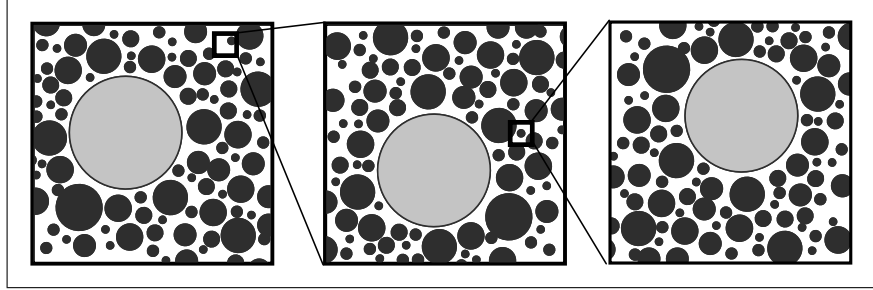


Figure 2.2: **Concentrated polydisperse suspensions.** A small number of large spheres are added to a suspension of smaller spheres, resulting in an infinitesimal increase in the volume fraction and a corresponding infinitesimal increase in the effective viscosity.

by the solute ϕ_T is then

$$\phi_T = \phi + \Delta\phi = \phi(1 - \phi_L) + \phi_L.$$

since the smaller spheres can only occupy the volume fraction of solvent left available *after* the larger spheres have been added. Alternatively, in terms of the change in the total volume fraction occupied,

$$\Delta\phi = \phi_L(1 - \phi).$$

If the large spheres are added in a small amount, $\phi_L \rightarrow 0$, we write the change in occupied volume fraction as an infinitesimal

$$\Delta\phi \approx d\phi = \phi_L(1 - \phi).$$

On the length scale of the large spheres, the suspension of smaller particles appears as a homogeneous fluid with viscosity η , and we use (2.7) to express the change in viscosity due to the addition of the larger spheres,

$$\eta_T = \eta + \Delta\eta = \eta \left(1 + \frac{5}{2}\phi_L \right).$$

Again, if the large spheres are added in a small amount, $\phi_L \rightarrow 0$, the change in viscosity will be infinitesimal

$$\Delta\eta \approx d\eta = \frac{5}{2}\phi_L\eta.$$

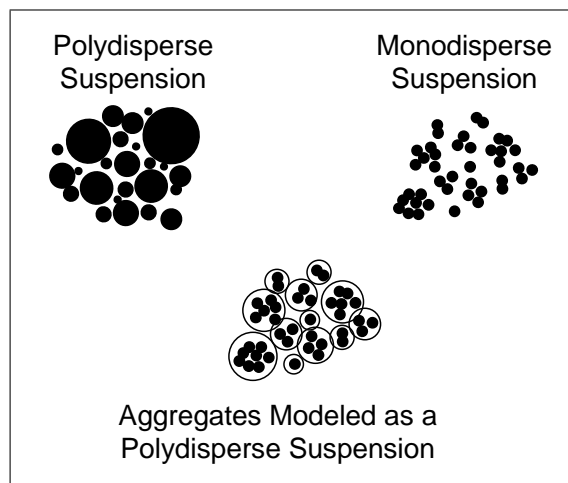


Figure 2.3: **Polydisperse and aggregated monodisperse suspensions.** Roscoe [75] suggested that a concentrated polydisperse suspension could be used as a model of aggregated monodisperse suspension, with different sized aggregates corresponding to a distribution of particle sizes.

Combining the infinitesimal change in the volume fraction with the resulting infinitesimal change in the macroscopic viscosity, we eliminate ϕ_L and arrive at a separable differential equation,

$$\frac{d\eta}{\eta} = \frac{5}{2} \frac{d\phi}{(1-\phi)}.$$

Integration of the differential equation yields an expression for the effective viscosity of a concentrated *polydisperse* suspension,

$$\boxed{\eta = \eta_0 (1 - \phi)^{-\frac{5}{2}}}, \quad (2.8)$$

where η_0 is the viscosity of the solvent in the total absence of suspended particles. This result holds for an infinitely disperse suspension, with ever smaller spheres occupying the space between larger spheres. As a result, the suspension solidifies ($\eta \rightarrow \infty$) when the volume fraction is unity ($\phi = 1$). The great insight of Roscoe was to suggest that an infinitely disperse suspension can be used to model aggregated suspensions of *monodisperse* spheres, with each aggregate behaving as a larger sphere (Figure 2.3). These aggregates

will have some solvent trapped between spheres, so ϕ must be modified to reflect this effective volume fraction of aggregates. For rigid spheres, closely packed, the trapped medium accounts for an increase in the effective volume fraction by a factor of $\frac{3\sqrt{2}}{\pi}$. A suspension of close packed rigid spheres will thus have an effective viscosity given by,

$$\eta = \eta_0 \left(1 - \frac{3\sqrt{2}}{\pi} \phi \right)^{-\frac{5}{2}}.$$

We then expect a monodisperse suspension of spheres to solidify at $\phi = \frac{\pi}{3\sqrt{2}} \approx 0.74$. In general, the particles in a concentrated suspension are rarely optimally packed, with suspension solidification occurring at some lower volume fraction called ϕ_{max} ,

$$\boxed{\eta = \eta_0 \left(1 - \frac{\phi}{\phi_{max}} \right)^{-\frac{5}{2}}.} \quad (2.9)$$

Repeating Roscoe's derivation for $\eta = \eta_0(1 + T\phi)$, where T is a function of the internal-to-external viscosity ratio $\kappa = \frac{\tilde{\eta}_0}{\eta_0}$, Pal [68] obtains an implicit expression for the effective viscosity of a homogeneous suspension of immiscible droplets,

$$\frac{\eta}{\eta_0} \left[\frac{\frac{\eta}{\eta_0} + \frac{5}{2}\kappa}{1 + \frac{5}{2}\kappa} \right]^{\frac{3}{2}} = \left(1 - \frac{\phi}{\phi_{max}} \right)^{-\frac{5}{2}\phi_{max}}.$$

In the limit of large internal viscosity, which is the case considered throughout the remainder of the dissertation, Pal's expression reduces to that of Roscoe (2.9). More generally, empirical expressions are often written with the exponent left free,

$$\boxed{\eta = \eta_0 \left(1 - \frac{\phi}{\phi_{max}} \right)^{-T}.} \quad (2.10)$$

The two parameters T and ϕ_{max} are determined experimentally, and there is a tremendous amount of scatter among suspensions [50]. As a result, this expression is more useful for correlating data from a specific suspension rather than as a predictive model, although the qualitative picture is appealing: Einstein's linear effective viscosity increase at low volume fraction and solidification at some maximum packing volume fraction ϕ_{max} (Figure 2.4).

Clearly, (2.10) cannot tell the whole story. There are essential suspension properties that are not represented, and lumped in some uncontrolled fashion in the two empirical

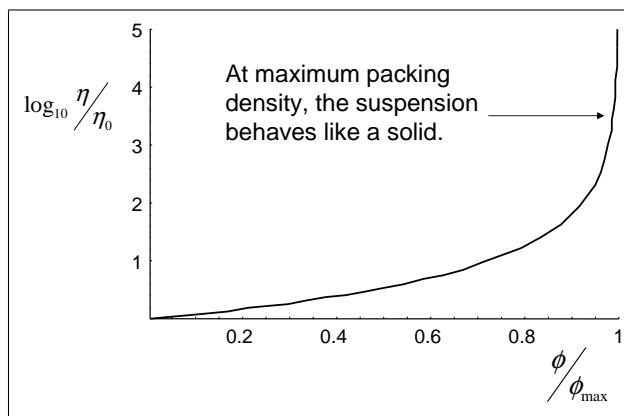


Figure 2.4: **Effective viscosity of a concentrated *homogeneous* suspension.** The effective viscosity increases with increasing particle volume fraction. Near the maximum particle packing density, the viscosity becomes very large, and the fluid behaves like a solid.

parameters T and ϕ_{max} . The most obvious restriction is that flowing suspensions are seldom homogeneous. Shear gradients or wall interactions invariably lead to some inhomogeneous particle distribution, and the geometry of the flow is an important consideration. In the next section, we describe an approach that takes account of the inhomogeneous particle distribution in tube flow by modeling blood as a *layered fluid* with a viscous core surrounded by rings of less viscous fluid.

2.2 Multiple-fluid models

At high flow rates, there is an observable striation of blood in tube flow, with a cell-deplete layer adjacent to the wall and an accumulation of red blood cells along the axis. Many models of blood rheology therefore take as their foundation this natural structuring of the flow, modeling the suspension as a layered fluid, with viscosity varying discretely across the vessel,

$$\eta(r) = \begin{cases} \eta_c & 0 \leq r < r_c \\ \eta_p & r_c \leq r \leq R, \end{cases}$$

where $\eta_c \gg \eta_p$ and r_c is the width of the core region (Figure 2.5a). Two layer flows of this

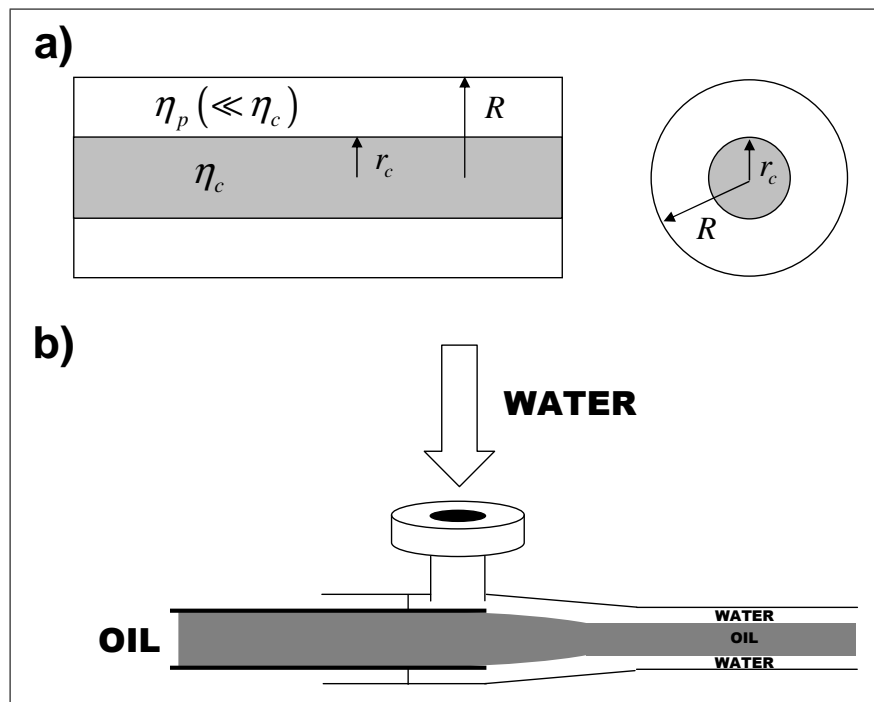


Figure 2.5: **Core-annular flows.** **a)** A two-layer fluid, with a high-viscosity core surrounded by a lower-viscosity lubricating layer. **b)** The reduced overall viscosity of core-annular flows is exploited by oil companies to move heavy oil great distances with comparatively little effort.

type are often called *core-annular flows* because looking down the tube, the viscous core is surrounded by an annulus of less viscous fluid (Figure 2.5a-inset). The viscosity is constant through each region and we assume both fluids are Newtonian so that we may write the only non-zero component of the shear-stress tensor⁵ for the fully developed laminar flow as

$$\tau = \eta(r) \frac{\partial u}{\partial r}, \quad (2.11)$$

where $\frac{\partial u}{\partial r}$ is the gradient in the velocity across the vessel. Here, and henceforth, all physical quantities are referred to a cylindrical coordinate system (r, θ, z) with the z -axis along the centerline of the flow. The creeping flow equations in cylindrical geometry, with the generalized Newtonian stress tensor (2.11) reduce to,

$$-\frac{dP}{dz} = -\frac{1}{r} \frac{d}{dr} \left(r \eta(r) \frac{du}{dr} \right),$$

where $\frac{dP}{dz}$ is the pressure drop along the tube. Applying no-slip boundary conditions at the wall, and requiring that the velocity be continuous across the vessel,

$$u(R) = 0$$

$$|u(0)| < \infty,$$

two integrations of the governing equation yield the general solution,

$$u(r) = -\frac{1}{2} \left(\frac{dP}{dz} \right) \int_r^R \frac{r' dr'}{\eta(r')}. \quad (2.12)$$

For the core-annular flow,

$$u(r) = \begin{cases} \frac{1}{4} \left(\frac{dP}{dz} \right) \left(\frac{(r^2 - r_c^2)}{\eta_c} + \frac{(r_c^2 - R^2)}{\eta_p} \right) & 0 \leq r \leq r_c \\ \frac{1}{4} \left(\frac{dP}{dz} \right) \left(\frac{(r^2 - R^2)}{\eta_p} \right) & r_c < r \leq R, \end{cases} \quad (2.13)$$

⁵*Shear-stress tensor*: The full stress tensor S_{ij} , without the pressure term $-p\delta_{ij}$. Also called the *extra-stress* or *deviatoric stress* tensor.

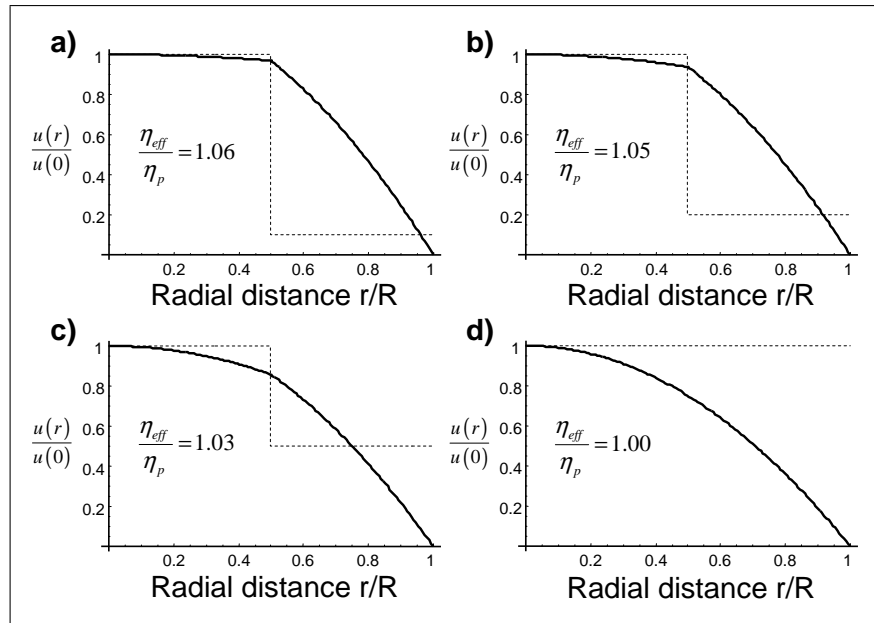


Figure 2.6: **Velocity profile of a core-annular flow - Variation in the viscosity difference.** **a)** The viscosity distribution $\frac{\eta(r)}{\eta_c}$ is shown as a dashed line. Here, the core viscosity is 10 times higher than in the lubricating layer. Nevertheless, the effective viscosity of the overall flow is raised by only 6%. The velocity profile is blunt along the axis - varying very little across the viscous core. **b)** The viscosity is 5 times higher than in the lubricating layer, with almost no change from panel a). **c)** The core viscosity is 2 times larger than in the lubricating layer, and the velocity profile is beginning to look more parabolic. **d)** With constant viscosity across the fluid, the velocity profile is parabolic.

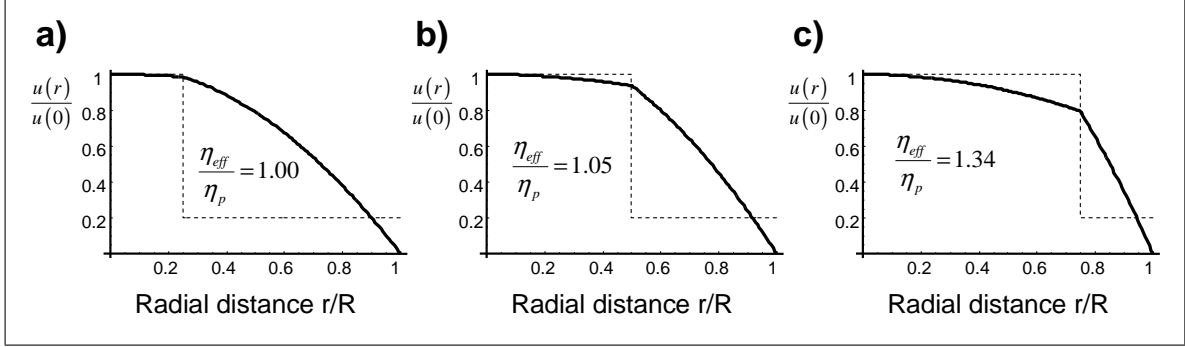


Figure 2.7: **Velocity profile of core-annular flows - Variation in core width.**

a) The core extends 25% of the way across the vessel, and the profile is essentially parabolic. **b)** The core extends 50% of the way across the vessel. **c)** The core extends 75% of the way across the vessel, and the velocity profile is clearly not parabolic. The effective viscosity, however, is only 34% more than the viscosity in the lubricating layer although the core is 5 times more viscous than the lubricating layer.

as compared to the classical Poiseuille flow of a homogeneous fluid with viscosity η ,

$$u_{Pois.}(r) = \frac{1}{4} \left(\frac{dP}{dz} \right) \frac{(r^2 - R^2)}{\eta}. \quad (2.14)$$

Sample plots of the core-annular velocity profile are shown in Figures 2.6 and 2.7. Large deviations of the flow velocity field from the parabolic profile are seen when $\eta_c \gg \eta_p$ and $r_c \approx R$. The volumetric flow rate Q is the integral of the velocity over the cross-sectional area,

$$Q = 2\pi \int_0^R u(r) r dr. \quad (2.15)$$

For a homogeneous fluid, using (2.14),

$$Q = -\frac{\pi R^4}{8\eta} \left(\frac{dP}{dz} \right). \quad (2.16)$$

Equating (2.15) and (2.16) we *define* the effective viscosity as an experimentally accessible

parameter that appears in the proportionality constant between the pressure drop and the flow rate,

$$-\frac{\pi R^4}{8\eta_{eff}} \left(\frac{dP}{dz} \right) = -\pi \left(\frac{dP}{dz} \right) \int_0^R r \int_r^R \frac{r' dr'}{\eta(r')} dr.$$

Rearranging, and solving for the effective viscosity, yields

$$\eta_{eff} = \frac{R^4}{8} \left[\int_0^R r \int_r^R \frac{r' dr'}{\eta(r')} dr \right]^{-1}. \quad (2.17)$$

Homogenization of the layered flow is therefore performed via a particular space-averaging derived from the Poiseuille flow. For the particular choice of $\eta(r)$ corresponding to core-annular flow we find

$$\eta_{eff} = \eta_p \left[1 - \left(\frac{r_c}{R} \right)^4 \left(1 - \frac{\eta_p}{\eta_c} \right) \right]^{-1},$$

and as $\eta_c \rightarrow \infty$ this reduces to

$$\eta_{eff} = \frac{\eta_p}{1 - \left(\frac{r_c}{R} \right)^4}.$$

Consequently, an infinitely viscous core can extend 45% of the way across the tube without raising the effective viscosity of the flow by more than 5% over the viscosity of the lubricating layer! This astonishing decrease in the viscosity of core-annular flows is exploited by oil companies to move heavy oil large distances using about as much energy as it would take to move water (Figure 2.5b).

There are obvious advantages for blood to adopt a core-annular microstructure [78], and so layered fluid approaches enjoy great popularity in the modeling of blood rheology [25, 42, 88]. Layered fluid models cannot be fully predictive, however, since r_c is an unknown empirically determined parameter and a notoriously difficult parameter to characterize consistently. The trouble lies in unambiguously assigning a precise location to the core interface since in the flow this is an averaged position at best, and variation of particle density on either side leads to a blurring of the surface, especially at slow to moderate flow rates. In principle, the flow can be divided into an arbitrary number of layers, but from a scientific point of view that compounds the uncertainty in the model by replacing

the unknown constant r_c with an unknown discrete distribution of the viscosity: $\{r_c^i, \eta_c^i\}$. While core-annular flow models suggest that microstructure has a dramatic effect on the suspension rheology, without a description of the mechanism underlying that microstructure such models are of limited use. What is needed is a viscosity distribution determined by more fundamental principles used in conjunction with a layered-fluid model.

In the next section, we consider a more general approach than the layered fluid models. Instead of assuming a generalized Newtonian stress tensor of the form $\tau = \eta(r) \frac{\partial u}{\partial r}$ with $\eta(r)$ to be determined, we explore the possibility of developing wholly original (non-Newtonian) formulations of the stress tensor $\tau \left(\frac{\partial u}{\partial r} \right)$, called *constitutive models*, with the hope that these may explain blood rheology.

2.3 Constitutive models

Implicit in the conservation principles that lay at the foundation of fluid mechanics is the *continuum hypothesis*. All matter is composed of molecules and microscopic molecular trajectories are unimaginably complex. The great miracle of thermodynamics is that for the most part microscopic details are unimportant, with the majority of physical phenomena being represented by a handful of observable macroscopic quantities such as density, velocity, temperature, and so on. Formally, we replace the full microscopic dynamics with averaged parameters, effectively smearing the discrete molecular world into a continuum. We are then able to enforce certain conservation principles (conservation of momentum, mass, energy, *etc.*), but this vast simplification comes at the cost of ignoring microscopic fluctuations. The result is a set of field equations that are not closed in the sense that the unknown macroscopic functions are *underdetermined* by the governing equations. It is by including the macroscopic effect of the molecular fluctuations that we arrive at the familiar Navier-Stokes equations of fluid mechanics, through a constitutive model of microscopic momentum transfer in the form of the shear-stress tensor. The origin of the shear-stress tensor is best illustrated by example [57].

Consider a simple shear flow between parallel plates. The streamlines of the macroscopic flow are parallel with the bounding walls and the fluid velocity field is tangent to these streamlines (Figure 2.8). Molecular fluctuations cause molecules to cross the streamlines,

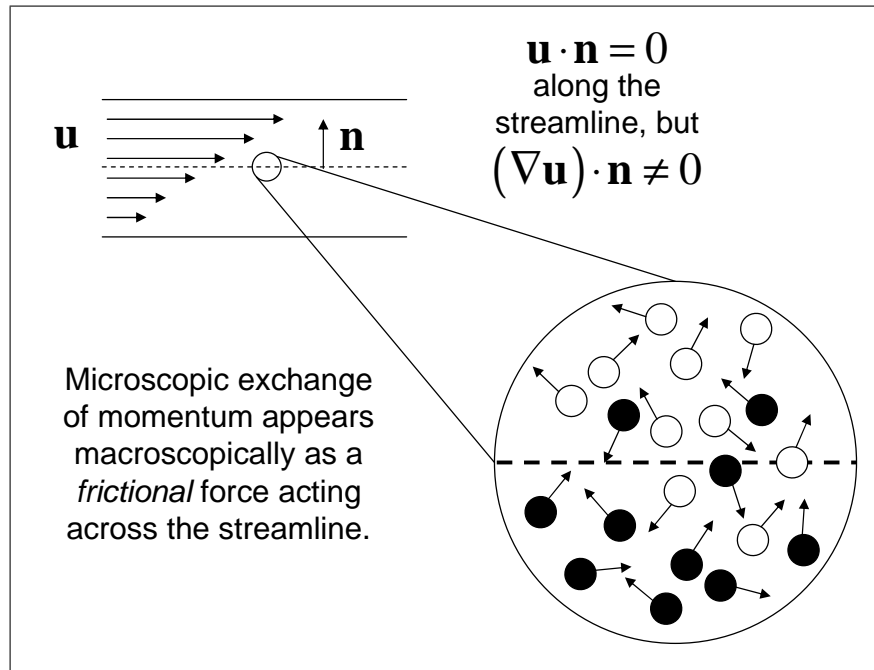


Figure 2.8: **The origin of the stress tensor in the microscopic exchange of momentum.** The white molecules are moving to the right faster than the black molecules. Microscopic fluctuations transfer faster moving particles to the slower moving fluid below the streamline and *vice versa*. The resulting transfer of momentum is manifest on the macroscopic scale as a *slowing down* of the fast fluid and a *speeding up* of the slow fluid. On the large scale, it seems as though a frictional force is acting across the streamline, and this frictional force is modeled as the shear-stress tensor τ . Notice that the mean exchange of particles is zero, since $\mathbf{u} \cdot \mathbf{n} = 0$. Redrawn from [57].

Model	Equation	Parameters
Generalized Newtonian	$\tau = \eta(r) \dot{\gamma}$	$\eta(r)$: viscosity distribution $\dot{\gamma}$: shear rate
Power Law	$\tau = m \dot{\gamma}^n$	m : consistency index n : non-Newtonian index
Hershel-Bulkley Model	$\tau = \begin{cases} \dot{\gamma} = 0 & \tau \leq \tau_y \\ m \dot{\gamma}^n + \tau_y & \tau > \tau_y \end{cases}$	τ_y : yield stress
Casson Model	$\tau = \begin{cases} \dot{\gamma} = 0 & \tau \leq \tau_y \\ (\eta^{1/2} \dot{\gamma}^{1/2} + \tau_y^{1/2})^2 & \tau > \tau_y \end{cases}$	

Table 2.1: **Popular constitutive models in blood rheology.** From [20] and [74].

though on average the movement of mass is balanced in either direction. The kinetic energy of the molecules is not the same, however, with faster molecules crossing the streamline from above and slower molecules from below. So although mass is conserved, there is a flux of momentum downward. The result on the macroscopic scale is an observable *slowing down* of the fast moving fluid and a *speeding up* of the slow moving fluid. This microscopic momentum transfer is modeled at the continuum level as a frictional force acting across the streamline, and expressed as the shear-stress tensor τ . The details of how momentum is transferred in the presence of a shear gradient is captured in the functional form of the stress tensor, called the constitutive model of the fluid. A sample of popular constitutive equations used to model blood flow are given in Table 2.1 (see also [2, 28, 70, 73]).

In principle, the constitutive equation must describe some fundamental microscopic mechanism for momentum transfer that is outside the purview of fluid mechanics and the continuum representation. This is a tremendously difficult task, and although some constitutive models that are used to model blood rheology have physical justification [79], in practice most are nothing more than *ad hoc* fitting-functions to experimental data [31].

The problem is the same as in layered fluid models discussed above: after choosing the form of the constitutive equation based upon semi-empirical reasoning, the investigator is left to fix a set of model parameters with obscure physical meaning. For example, parameters are often fixed using instruments that subject *homogeneous Newtonian* fluids to a constant shear gradient, but for suspensions in these instruments, the shear gradient will vary through the fluid. The result is that the relationship of parameters fixed using such instruments to *in vivo* blood rheology is unclear⁶. It is of fundamental importance to derive a model of blood flow that will encompass the features of flow inhomogeneity present in layered-fluid models and the details of microscopic momentum transfer contained in the constitutive equation all the while based upon a sound physical foundation.

2.4 Flow microstructure and local viscosity

In the following chapters, we develop a model that unites the three approaches discussed above. First, we consider the forces acting on a deformable blood cell in laminar tube flow, deriving a conservation equation for the red cell volume fraction $\phi(r)$. Solving for the steady-state volume fraction distribution $\phi^{ss}(r)$, we use Roscoe's expression for the viscosity of a concentrated suspension to translate the flow microstructure into a continuous viscosity distribution $\eta_\phi(r)$. Postulating the simplest of all constitutive equations – the generalized Newtonian stress tensor $\tau(r) = \eta_\phi(r) \frac{\partial u}{\partial r}$ – we solve the creeping flow equations for the overall suspension velocity. The expression is identical to the expression derived for the layered fluid model, but now with a viscosity distribution calculated directly from the flow-induced microstructure.

⁶This point will be taken up again in chapter 6.

Chapter 3

Microstructure

In the previous chapter, considering past work on *homogeneous* suspensions and layered flows, it was clear that the microscopic distribution of particles can dramatically decrease the observed viscosity of a flowing suspension. In the present chapter, we examine the forces acting on a deformable particle in tube flow, and derive a conservation equation for the particle distribution function $\phi(r, t)$. Solving for the steady-state, we arrive at an expression for the microscopic particle distribution $\phi^{ss}(r)$ as a function of the flow conditions and particle properties.

The data of Chien [21] shown in Figure 3.1 suggests that red blood cells adopt two qualitatively distinct microstructures in response to flow. At low shear rates ($0 - 1s^{-1}$), the red cells form extended aggregates called *rouleaux*. As the shear rate is increased, the aggregates are broken up so that the average aggregate size decreases and a corresponding decrease in the apparent viscosity is observed. This is analogous to the mechanism proposed by Casson to describe the rheology of printers' ink [17], and is often used to justify the use of Casson's equation in the modeling of blood flow.

Inspired by Casson's nonlinear constitutive model, many attempts have been made to capture the low-shear rheology of blood through a suitable constitutive equation based on the aggregation and break-up of cell clusters [64, 66, 74, 83]. In the present study, however, we will be concerned with the high-shear ($> 3s^{-1}$) behaviour of blood where cell deformability, and not aggregation, determines the character of the suspension flow.

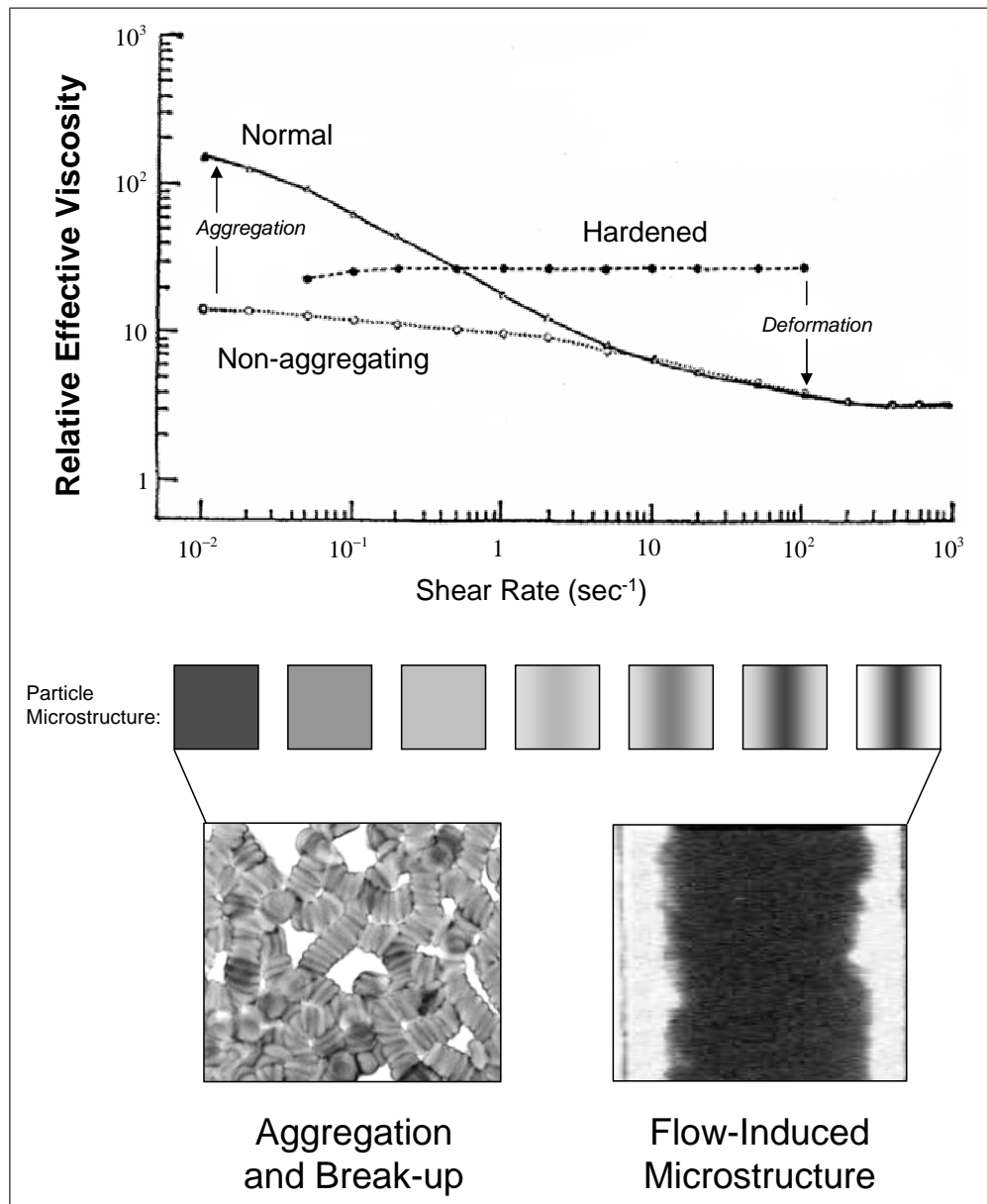


Figure 3.1: Schematic diagram of the relationship between microstructure and the apparent viscosity. A cartoon of the microstructure is shown in the panels below the main figure, illustrating the aggregation-dominated regime at low shear and particle redistribution at high shear.

Although the shear-rate is *not* constant across the gap, with regions of low shear near the centerline, the data of Chien (Figure 3.1) clearly shows that the effect of aggregation in the low-shear regions has negligible effect on the overall rheology at high averaged shear rates.

At moderately high shear rates ($> 3s^{-1}$), red blood cells move away from the walls and accumulate near the vessel axis. The low viscosity, particle depleted plasma layer lubricates the flow resulting in an observed decrease in the apparent viscosity. A simplified picture of the flow microstructure as a function of shear rate is shown in Figure 3.1.

In this chapter, we derive a conservation equation that describes this redistribution of red blood cells with particular care to include particle deformability as an essential mechanism.

3.1 Particle Redistribution

Consider an arbitrary control volume V of fixed shape moving with the background fluid flow. There is some volume fraction of V occupied by particles, called ϕ . The change in the total volume occupied by particles is,

$$\frac{\partial}{\partial t} \int_V \phi dV = \int_V \frac{\partial \phi}{\partial t} dV = - \int_S \mathbf{J} \cdot \mathbf{n} dS,$$

where \mathbf{J} is the flux of particles across the surface S of the control volume. Using the divergence theorem, we rewrite this equation as

$$\int_V \left[\frac{\partial \phi}{\partial t} + \nabla \cdot \mathbf{J} \right] dV = 0,$$

and since V is arbitrary and the fields are continuous – so that the du Bois-Reymond lemma applies – we arrive at the local conservation equation for the volume fraction, viz.

$$\frac{\partial \phi}{\partial t} = -\nabla \cdot \mathbf{J}.$$

There are two primary mechanisms responsible for the flux of particles across the surface of the control volume: a convective flux¹ \mathbf{J}_{conv} arising from the cross-stream migration of

¹Also called the *advective flux* or *transport term*.

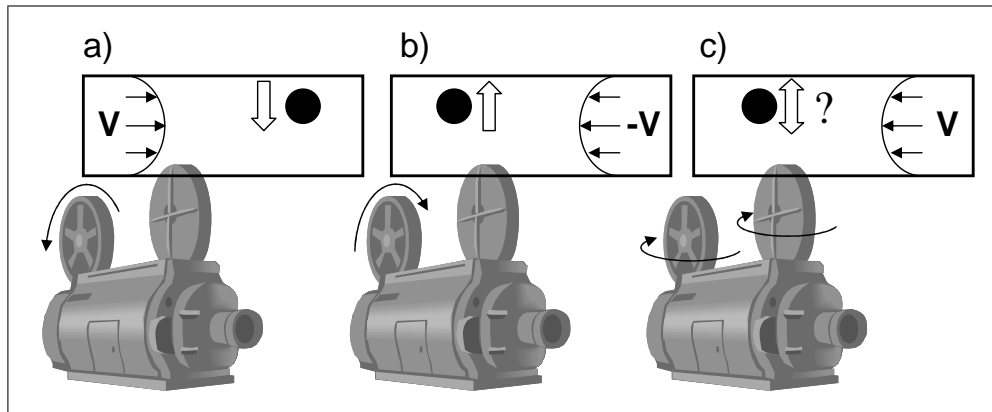


Figure 3.2: **Impossibility of cross-stream migration of a sphere in creeping flow.**

a) Consider a movie of a sphere in a unidirectional creeping flow, and suppose there is some force acting perpendicular to the wall to move the sphere across the flow. **b)** Reverse the direction of the velocity by playing the movie backward. The perpendicular force will now point in the opposite direction. **c)** But if the film is turned back to front, or the observer moves to the other side of the screen, the flow is indistinguishable from the flow in panel a). For the perpendicular force to act both upward and downward, it must be zero. Hence, there cannot be cross-stream migration of a sphere in creeping Newtonian flow.

red blood cells, and a diffusive flux \mathbf{J}_{diff} opposing particle packing.

In order to proceed, we require a suitable geometrical representation of the red blood cells. Their rest shape is difficult to model explicitly, so we make the simplification that in flow they behave like droplets of immiscible fluid [3, 35, 77, 89]. We can then take advantage of the work of Chan and Leal [18] who studied the problem of the migration of a fluid drop in a unidirectional shear flow.

3.1.1 Migration of a Fluid Droplet - Chan & Leal 1979

The streamlines of tube flow are parallel with the bounding walls; a convective flux therefore requires a mechanism inducing cross-stream migration. A neutrally buoyant hard sphere in creeping flow will not show any cross-stream migration. The argument, due to F. P. Bretherton [11] (see also p. 128 of [57]), is straightforward. The creeping Newtonian

equations for the flow around a sphere are linear in the velocity v and the pressure field P . If $\{v, P\}$ is a solution, so too is $\{-v, -P\}$. Suppose there is some downward force acting on the spherical particle, perpendicular to the walls when the flow velocity is v (Figure 3.2). Reversing the velocity and pressure field by running time backward, the perpendicular force will seem to act in the opposite direction while the flow velocity is $-v$. If the original flow is viewed from the other side of the tube, however, a velocity of $-v$ is likewise observed, but *with the migration force acting downward*. We are left to conclude that the migration force acts upward if we observe the flow from one side of the tube, and downward if we observe the flow from the other side. This is clearly a contradiction unless the migration force is zero. Hence, no cross-stream migration is possible for a neutrally buoyant, rigid spherical particle in the creeping flow of a Newtonian fluid.

Convective flux can only be realized if some term (e.g. nonlinearity) is introduced into the creeping flow equations to break the symmetry [56]. For example if the Reynolds number is not small and inertial terms contribute appreciably to the long-term behaviour of the system, the governing equations contain a symmetry breaking non-linearity of the form $\mathbf{v} \cdot \nabla \mathbf{v}$, and the conclusion of Bretherton no longer holds. Indeed, Segre and Silberberg [80] have observed cross-stream migration due to inertial effects in suspensions of rigid spheres. The symmetry of the governing equations may likewise be broken by immersing the particles in a non-Newtonian solvent. In this case, the nonlinearity lies in the constitutive equation of the fluid.

Here, we are primarily concerned with drift due to *deformation* of a spherical particle in creeping flow. Deformation of the particle surface transforms the mathematical model into a free boundary-value problem in which the location of the deformed surface has to be determined as part of the solution. The resulting symmetry-breaking condition can be accommodated by means of a perturbation expansion, assuming that the spherical shape of the particle is only slightly altered by hydrodynamic interactions with the walls and by the stretching of the surface by the shear-gradient in the flow. We present in some detail the work of Chan and Leal [18] deriving an expression for the cross-stream migration of a deformable drop in tube flow.

Chan and Leal [18] consider the motion of a neutrally buoyant drop in a unidirectional, quadratic shearing flow at zero Reynolds number. Their analysis is more general than

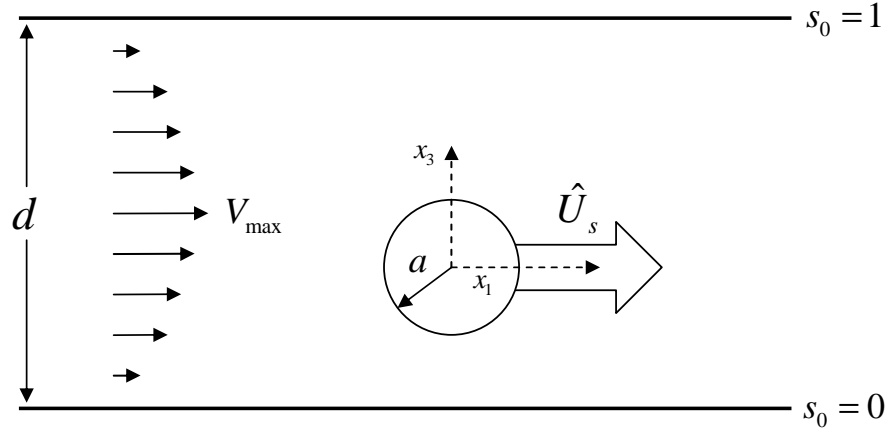


Figure 3.3: Coordinate system of Chan and Leal [18].

what we require since we shall restrict ourselves to a Newtonian suspending medium and a Newtonian fluid droplet. We follow their derivation for a two-dimensional Poiseuille flow, and their transformation to apply the results in three-dimensional tube flow. The system is non-dimensionalized using a characteristic velocity Ga , where a is the drop radius and G is the averaged shear rate in the bulk. The stress tensor in the two fluids is non-dimensionalized by $G\eta_0$ and $G\tilde{\eta}_0$, where η_0 is the viscosity in the medium and $\tilde{\eta}_0$ is the viscosity inside the fluid drop. The total velocity, pressure and stress distributions in the two fluids (including the disturbance due to the presence of the drop) are $(\mathbf{U}, P, \mathbf{S})$ and $(\tilde{\mathbf{U}}, \tilde{P}, \tilde{\mathbf{S}})$, where, again, the tilde denotes a function *inside* the drop. Finally, we denote the undisturbed velocity, pressure and stress fields by $(\mathbf{V}, Q, \mathbf{T})$.

The coordinate system has its origin at the center of the drop, with \mathbf{x} denoting the vector emanating from the origin, non-dimensionalized with respect to the particle radius a . In two-dimensional flow, we have only two components of \mathbf{x} : x_1 is chosen to lie in the direction of the bulk flow, and x_3 is perpendicular to the confining walls. Relative to a fixed laboratory frame, the drop translates with velocity \hat{U}_s , where the subscript s denotes quantities measured relative to the fixed-frame (Figure 3.3). The bulk flow \mathbf{V} , ignoring the disturbance due to the particle, is written as a general quadratic flow, [see eq. 2.6a on

p. 135 of [18]]

$$\mathbf{V} = (\alpha + \beta x_3 + \gamma x_3^2) \mathbf{e}_1 - \hat{\mathbf{U}}_s. \quad (3.1)$$

Here, \mathbf{e}_1 is the unit vector in the x_1 direction. For two-dimensional Poiseuille flow, the velocity field with respect to the laboratory frame is

$$V_s(s_0) = 4V_{\max}s_0(1 - s_0). \quad (3.2)$$

The lab coordinate s_0 is linearly related to the drop coordinate \mathbf{x} via,

$$s_0 = s + x_3 \frac{a}{d}, \quad (3.3)$$

where s is the location of the drop center, and x_3 has been non-dimensionalized, now with respect to the gap width d . With substitution of (3.3) into (3.2), the coefficients in the general unidirectional flow are given by [eq. 2.8 on p. 135]²,

$$\begin{aligned} \alpha &= 4V_{\max}s(1 - s) \\ \beta &= 4V_{\max}(1 - 2s)\zeta \\ \gamma &= -4V_{\max}\zeta^2, \end{aligned} \quad (3.4)$$

where $\zeta = \frac{a}{d}$ is the ratio of the particle radius to the gap width d .

The equations of motion of the total flow are

$$\begin{aligned} \nabla \cdot \mathbf{S} &= 0 & \nabla \cdot \mathbf{U} &= 0 \\ \nabla \cdot \tilde{\mathbf{S}} &= 0 & \nabla \cdot \tilde{\mathbf{U}} &= 0, \end{aligned}$$

where

$$\begin{aligned} S_{ij} &= -P\delta_{ij} + \left(\frac{\partial U_i}{\partial x_j} + \frac{\partial U_j}{\partial x_i} \right) \\ \tilde{S}_{ij} &= -\tilde{P}\delta_{ij} + \left(\frac{\partial \tilde{U}_i}{\partial x_j} + \frac{\partial \tilde{U}_j}{\partial x_i} \right). \end{aligned}$$

²Here, and henceforth, square brackets preceding the equation refer to the equation and page number in the original paper by Chan and Leal [18].

The far-field boundary conditions require that the disturbance velocity vanishes and that there is no slip velocity at the bounding walls,

$$\mathbf{U} \rightarrow \mathbf{V} \quad \text{as } r = |\mathbf{x}| \rightarrow \infty$$

$$\mathbf{U} = V_w \mathbf{e}_1 - \hat{\mathbf{U}}_s \quad \text{on the walls,}$$

where V_w is the velocity contribution $(\alpha + \beta x_3 + \gamma x_3^2)$ evaluated at the wall.

The droplet surface will be deformed by shear gradients in the flow or hydrodynamic interactions with the walls. The deformation of the particle surface boundary cannot be determined independently of the flow, however. Equations of this type are called *free-boundary problems* and in general are very difficult to solve. Chan and Leal overcome this difficulty by considering a perturbation expansion in the deformability of the drop. The boundary conditions on the surface of the *deformed* drop are continuity of velocity, no normal flow and continuity of the stress,

$$\mathbf{U} = \tilde{\mathbf{U}}$$

$$\mathbf{U} \cdot \mathbf{n} = \tilde{\mathbf{U}} \cdot \mathbf{n} = 0$$

$$\mathbf{S} \cdot \mathbf{n} = \kappa \tilde{\mathbf{S}} \cdot \mathbf{n} + \frac{1}{\delta} \left(\frac{1}{R_1} + \frac{1}{R_2} \right) \mathbf{n}. \quad (3.5)$$

Here $\kappa = \frac{\tilde{\eta}_0}{\eta_0}$ is the ratio of the internal to external viscosity, R_1 and R_2 are the principal radii of curvature of the deformed droplet, and the parameter δ is a dimensionless measure of the magnitude of viscous forces to drop deformability, expressed in terms of the interfacial tension σ ,

$$\delta = \frac{a\eta_0 G}{\sigma}. \quad (3.6)$$

The deformability is assumed to be small, and the solution to the flow problem is written as a perturbation expansion in δ .

The particle velocity, expanded in powers of δ , becomes [eq. 2.11 on p. 137]

$$\hat{\mathbf{U}}_s = \hat{\mathbf{U}}_s^{(0)} + \delta \hat{\mathbf{U}}_s^{(\delta)} + \delta^2 \hat{\mathbf{U}}_s^{(\delta\delta)} + \dots$$

The zero-order term $\hat{\mathbf{U}}_s^{(0)}$ is the translational velocity of a perfectly spherical drop, and from the argument of Bretherton above, we know $\hat{\mathbf{U}}_s^{(0)} = 0$. Similarly, expanding the other functions in powers of δ ,

$$\mathbf{U} = \mathbf{U}^{(0)} + \delta\mathbf{U}^{(\delta)} + \delta^2\mathbf{U}^{(\delta\delta)} + \dots$$

$$P = P^{(0)} + \delta P^{(\delta)} + \delta^2 P^{(\delta\delta)} + \dots$$

$$\mathbf{S} = \mathbf{S}^{(0)} + \delta\mathbf{S}^{(\delta)} + \delta^2\mathbf{S}^{(\delta\delta)} + \dots,$$

while inside the drop,

$$\tilde{\mathbf{U}} = \tilde{\mathbf{U}}^{(0)} + \delta\tilde{\mathbf{U}}^{(\delta)} + \delta^2\tilde{\mathbf{U}}^{(\delta\delta)} + \dots$$

$$\tilde{P} = \frac{1}{\delta}\tilde{P}^{(\frac{1}{\delta})} + \tilde{P}^{(0)} + \delta\tilde{P}^{(\delta)} + \dots$$

$$\tilde{\mathbf{S}} = \frac{1}{\delta}\tilde{\mathbf{S}}^{(\frac{1}{\delta})} + \tilde{\mathbf{S}}^{(0)} + \delta\tilde{\mathbf{S}}^{(\delta)} + \dots$$

The $O(\frac{1}{\delta})$ terms are required to satisfy (3.5) in the case of a quiescent spherical drop.

The shape of the drop is also expanded as a perturbation series in δ . $F(r)$ is the parametric droplet surface, with $r = |\mathbf{x}|$ and \mathbf{x} is non-dimensionalized with respect to the drop radius a . Consequently, the surface of the undeformed (spherical) drop is given by $F(r) = r - 1 = 0$. In general, however, expressed in terms of the deformations $f^{(\delta^n)}$ at $O(\delta^n)$,

$$F(r) = r - 1 - \delta f^{(\delta)} - \delta^2 f^{(\delta\delta)} - \dots = 0. \quad (3.7)$$

The stress condition (3.5) is then re-written using $F(r, \delta)$ to express the outward unit normal \mathbf{n} and the curvature as a series in δ [eq. 2.15 on p. 138],

$$\mathbf{n} = \frac{\nabla F}{|\nabla F|} = \mathbf{e}_r - \delta\nabla f^{(\delta)} - \delta^2 \left[\nabla f^{(\delta\delta)} + \frac{1}{2} (\nabla f^{(\delta)} \cdot \nabla f^{(\delta)}) \mathbf{e}_r \right] + \dots$$

$$\frac{1}{R_1} + \frac{1}{R_2} = \nabla \cdot \mathbf{n} = 2 - \delta [2f^{(\delta)} + \nabla^2 f^{(\delta)}] - \dots$$

Any quantity evaluated at the surface is expanded in a Taylor series about $r = 1$ using (3.7).

The full solution at each order of δ will therefore determine the cross-stream migration to that order in δ . To simplify the calculations, Chan and Leal introduce a reciprocal

theorem that allows the calculation of the cross-stream migration to any order in δ using only the solution to the problem *one order less* in δ . We shall only require the migration velocity to $O(\delta)$. With the reciprocal theorem, all that is needed is the solution at $\delta = 0$, the translation of a *spherical* drop in a Poiseuille flow.

The complimentary problem, required for the reciprocal theorem, would typically use a drop of the same *shape* as in the original problem, but moving in a *quiescent* fluid. Using the Taylor expansion above to replace the deformed drop by a sphere with suitably modified boundary conditions in the original problem, it becomes possible to use a spherical drop in the complimentary problem as well. The equations of motion for a sphere moving perpendicular to the bounding walls in a quiescent fluid are

$$\nabla \cdot \tilde{\mathbf{S}} = 0 \quad \nabla \cdot \mathbf{u} = 0,$$

where,

$$t_{ij} = -q\delta_{ij} + \left(\frac{\partial u_j}{\partial x_i} + \frac{\partial u_i}{\partial x_j} \right),$$

with similar equations governing the flow inside the drop $(\tilde{\mathbf{u}}, \tilde{q}, \tilde{\mathbf{S}})$. The flow vanishes far from the drop and at the walls,

$$\mathbf{u} \rightarrow -\mathbf{e}_3 \quad \text{as } r \rightarrow \infty$$

$$\mathbf{u} = -\mathbf{e}_3 \quad \text{on the walls.}$$

(Recall that \mathbf{e}_3 is the unit vector in the direction perpendicular to the walls). Generalizing the reciprocal theorem of Lorentz for solenoidal vector fields [62], Chan and Leal derive a reciprocal relation [eq. 3.11 on p. 141],

$$\int_{A_d} \left[(\mathbf{S} - \kappa\tilde{\mathbf{S}}) \cdot \mathbf{u} - (\tilde{\mathbf{S}} - \kappa\tilde{\mathbf{S}}) \cdot \mathbf{U} - \kappa\tilde{\mathbf{S}} \cdot (\mathbf{U} - \tilde{\mathbf{U}}) - \tilde{\mathbf{S}} \cdot \mathbf{u} + \tilde{\mathbf{S}} \cdot \mathbf{V} \right] \cdot \mathbf{n} \, dA = 0, \quad (3.8)$$

allowing higher order solutions to be calculated from those of one order lower in δ . The quiescent terms $O(\frac{1}{\delta})$ are,

$$\begin{aligned} \tilde{P}^{(\frac{1}{\delta})} &= \frac{2}{\kappa} \\ \tilde{S}_{ij}^{(\frac{1}{\delta})} &= -\frac{2}{\kappa}\delta_{ij}. \end{aligned}$$

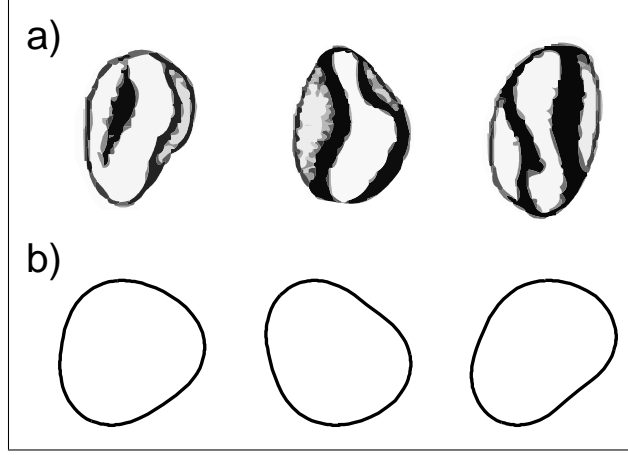


Figure 3.4: **Predicted droplet shape compared to red blood cells in flow.** a) Various blood cells shapes observed in flow through glass tubes [40]. b) Some predicted droplet shapes from the work of Chan and Leal [18].

The zero-order solutions are still very difficult to calculate exactly. Chan and Leal resort to the method of reflections [43] to approximate the solution. Assuming the ratio of the particle radius to the gap width is small, $\zeta = \frac{a}{d} \ll 1$, the solution is expanded as

$$\mathbf{U}^{(0)} = {}_1\mathbf{U}^{(0)} + {}_2\mathbf{U}^{(0)} + {}_3\mathbf{U}^{(0)} + \dots,$$

where ${}_i\mathbf{U}^{(0)}$ is the i^{th} reflection obeying the boundary conditions alternately at the surface of the particle and the bounding walls. From the boundary stress condition, the δ -expansion of the unit normal, and the curvature, the shape of the drop at each order in δ is calculated. To first-order, with $(x_1, x_3) = (r \cos \theta, r \sin \theta)$ in plane polar coordinates,

$$f^{(\delta)}(\theta) = \beta \frac{16 + 19\kappa}{8(1 + \kappa)} \sin \theta \cos \theta - \gamma \frac{10 + 11\kappa}{40(1 + \kappa)} (\cos \theta - 5 \cos \theta \sin^2 \theta).$$

Sample plots of the droplet surface $r = 1 - \delta f^{(\delta)}(\theta)$ are shown in Figure 3.4. Although heuristic, the drop shapes bear a plausible resemblance to the shape of red blood cells observed in flow, suggesting that the eventual representation of a red blood cell by a fluid

droplet has some justification. Collecting the $O(\delta)$ terms in (3.8) [eq. 6.4 on p. 157],

$$\begin{aligned} - \int_{A_d} \left[\left(\mathbf{S}^{(\delta)} - \kappa \tilde{\mathbf{S}}^{(\delta)} \right) \cdot \mathbf{u} - (\mathbf{t} - \kappa \tilde{\mathbf{t}}) \cdot \mathbf{U}^{(\delta)} - \kappa \tilde{\mathbf{t}} \cdot \left(\mathbf{U}^{(\delta)} - \tilde{\mathbf{U}}^{(\delta)} \right) \right] \cdot \mathbf{e}_r dA = \\ = \frac{2\pi(2+3\kappa)}{1+\kappa} \left(\hat{\mathbf{U}}_s^{(\delta)} \right)_3, \end{aligned}$$

where the third reflection of the migration velocity comes from the $\mathbf{t} \cdot \mathbf{V}$ term. Rearranging for the migration velocity, writing the integrand explicitly [eq. 6.6 on p. 157],

$$\begin{aligned} \left(\hat{\mathbf{U}}_s^{(\delta)} \right)_3 = - \frac{1+\kappa}{2\pi(2+3\kappa)} \int_{A_d} \left\{ \left[-f^{(\delta)} \frac{\partial}{\partial r} \left(\mathbf{S}^{(0)} - \kappa \tilde{\mathbf{S}}^{(0)} \right) \cdot \mathbf{e}_r + \left(\mathbf{S}^{(0)} - \kappa \tilde{\mathbf{S}}^{(0)} \right) \cdot \nabla f^{(\delta)} \right. \right. \quad (3.9) \\ \left. \left. + \nabla f^{(\delta)} (2f^{(\delta)} + \nabla^2 f^{(\delta)}) \right] \cdot \mathbf{u} + (\mathbf{t} - \kappa \tilde{\mathbf{t}}) : \mathbf{e}_r \mathbf{e}_r \left[f^{(\delta)} \left(\frac{\partial}{\partial r} \mathbf{U}^{(0)} \right) \cdot \mathbf{e}_r - \mathbf{U}^{(0)} \cdot \nabla f^{(\delta)} \right] \right. \\ \left. \left. + \kappa \tilde{\mathbf{t}} \cdot \mathbf{e}_r \cdot \left[f^{(\delta)} \frac{\partial}{\partial r} \left(\mathbf{U}^{(0)} - \tilde{\mathbf{U}}^{(0)} \right) \right] \right\} dA. \end{aligned}$$

For the two-dimensional flow, the integrand above can be expressed as [eq. 6.7 on p. 158],

$$\left(\hat{\mathbf{U}}_s^{(\delta)} \right)_3 \sim \int_{A_d} [O(\zeta^2) + O(\zeta^3) + O(\zeta^4)] dA,$$

where the $O(\zeta^2)$ term is odd in x_3 , and therefore vanishes. The leading order term is $O(\zeta^3)$, proportional to $\beta\gamma$ [eq. 6.8 on p. 158],

$$\begin{aligned} \left(\hat{\mathbf{U}}_s^{(\delta)} \right)_3 = - \frac{\beta\gamma}{(1+\kappa)^2(2+3\kappa)} \left[\frac{(16+19\kappa)(13-36\kappa-73\kappa^2-24\kappa^3)}{42(2+3\kappa)(4+\kappa)} + \right. \\ \left. + \frac{(10+11\kappa)(8-\kappa+3\kappa^2)}{105} \right] \mathbf{e}_3. \end{aligned}$$

Here, again, the subscript s indicates drop migration relative to the fixed laboratory frame, and the hat indicates a superposition of this velocity over the bulk fluid flow. With a final transformation of the two-dimensional flow to full three-dimensional tube flow, the cross-stream migration is [eq. 6.10 on p. 159],

$$\hat{U}_m = - \frac{\beta\gamma}{(1+\kappa)^2(2+3\kappa)} \left[\frac{3}{14} \frac{(16+19\kappa)(1-\kappa-2\kappa^2)}{(2+3\kappa)} + \frac{(10+11\kappa)(8-\kappa+3\kappa^2)}{140} \right].$$

In three-dimensional tube flow, the constants (α, β, γ) are given by,

$$\begin{aligned}\alpha &= V_{\max} \left(1 - \frac{r^2}{R^2} \right) \\ \beta &= -2V_{\max} \frac{ar}{R^2} \\ \gamma &= -V_{\max} \frac{a^2}{R^2},\end{aligned}$$

where r is the radial distance from the tube center and R is the radius of the tube. In tubular flow, the gap width d and averaged shear rate G must be redefined as,

$$\begin{aligned}\zeta &= \frac{a}{2R} \\ G &= \frac{V_{\max}}{R}.\end{aligned}$$

Expressing the migration velocity with all the units written explicitly gives the final result

$$\boxed{u_m(r) = \delta Ga \left[\left(\hat{\mathbf{U}}_s^{(\delta)} \right)_3 \right] = -2P(\kappa) \frac{V_{\max}^2 \eta_0}{\sigma} \left(\frac{a}{R} \right)^3 \left(\frac{r}{R} \right),} \quad (3.10)$$

where we have abbreviated the dependence on the viscosity ratio κ as

$$P(\kappa) = \frac{3}{14} \frac{(16 + 19\kappa)(1 - \kappa - 2\kappa^2)}{(1 + \kappa)^2 (2 + 3\kappa)^2} + \frac{(10 + 11\kappa)(8 - \kappa + 3\kappa^2)}{140(1 + \kappa)^2 (2 + 3\kappa)}.$$

and replaced V_{max} by $\frac{V_{max}}{Ga}$.

Notice that the migration velocity is *linear* in the radial coordinate r . It is also clear that if the shear rate is increased (*i.e.* V_{max} is increased) or the particle deformability is increased (*i.e.* σ is decreased), the migration force likewise increases and we would expect the flow to become layered with a core developing along the axis of the tube. The model so far appears to be consistent with experimental observation.

The internal viscosity of the droplet $\tilde{\eta}_0$ is a measure of the resistance offered to the motion of fluid within. The red blood cells, however, do not have a homogeneous internal structure, and so we must ask what meaning $\tilde{\eta}_0$ can have in the context of a biological cell. It is not enough to lyse the cell and measure the viscosity of the cell contents. The relevance of the internal viscosity to the migration velocity comes from the development of

internal circulation patterns that dissipate energy [86]. The rugged internal architecture of the cell provides strong resistance to flow of the cytoplasm. It seems appropriate, then, to model the internal environment of the red blood cell as a highly viscous fluid. Taking the limit as $\tilde{\eta}_0 \rightarrow \infty$ (or $\kappa = \frac{\tilde{\eta}_0}{\eta_0} \rightarrow \infty$), we arrive at³

$$\lim_{\kappa \rightarrow \infty} P(\kappa) = \frac{11}{140}.$$

With an expression for the migration velocity of a single particle, we write the convective flux as,

$$\mathbf{J}_{conv} = \phi u_m(r) \mathbf{e}_r.$$

Although derived for the motion of a *single* drop, we use $u_m(r)$ for the motion of a red blood cell in an arbitrarily concentrated suspension, treating the surrounding particles as a smeared-out effective medium. As in the continuum hypothesis, the representation of the discrete particulate as an effective mean-field comes at the expense of ignoring the effect of particle-particle interactions on the convective transport of a single particle. We attempt to compensate for the fine-scale fluctuations arising from interparticle and solvent collisions by including a diffusive flux, modeled after Fick's law,

$$\mathbf{J}_{diff} = -D\nabla\phi,$$

where D is the rate of diffusion. The diffusive flux will act in opposition to the tendency of particles to accumulate along the axis, and in the absence of a convective flux, it will drive the system toward the homogeneous particle distribution $\nabla\phi = 0$. The diffusion coefficient may be a function of space for inhomogeneous concentrated suspensions, including as it does restricted motion due to cage effects [24] and asymmetric collisions in the shear flow [52, 58]. Here we assume that D is constant in space, though it may be dependent upon the flow rate and the averaged particle packing density ϕ_0 . The connection between the diffusion coefficient and the mean-field approximation underlying the use of u_m in \mathbf{J}_{conv} will be explored in more detail in Chapter 7.

³The perturbation expansion of Chan and Leal assumes $\kappa \ll O(\frac{1}{\delta})$. The limit $\kappa \rightarrow \infty$ must therefore be interpreted as $O(1) \ll \kappa \ll O(\frac{1}{\delta})$, with $\delta \rightarrow 0$.

3.2 Particle Conservation Equation

In principle the total flux \mathbf{J} may contain contributions arising from additional mechanisms, such as the electrostatic repulsion between the vessel walls and the particle surface, sedimentation, *etc.*, but here we only consider the convective contribution from particle deformation and the diffusive contribution arising from particle-particle interactions. The conservation equation for the particle volume fraction then reads,

$$\frac{\partial \phi}{\partial t} = -\nabla \cdot [\phi u_m(r) \mathbf{e}_r - D \nabla \phi],$$

or in cylindrical coordinates, with $u_m(r)$ defined in (3.10),

$$\frac{\partial \phi(r, t)}{\partial t} = -\frac{1}{r} \frac{\partial}{\partial r} \left\{ r \left[u_m(r) \phi(r, t) - D \frac{\partial \phi(r, t)}{\partial r} \right] \right\}. \quad (3.11)$$

Nondimensionalizing time with respect to the rate of diffusion, $\hat{t} = \frac{D}{R^2} t$, and the radial distance by the vessel radius, $\hat{r} = \frac{r}{R}$, the particle conservation equation (3.11) reduces to

$$\frac{\partial \phi}{\partial \hat{t}} = \frac{1}{\hat{r}} \frac{\partial}{\partial \hat{r}} \left\{ \hat{r} \left[2\varepsilon \hat{r} \phi + \frac{\partial \phi}{\partial \hat{r}} \right] \right\}, \quad (3.12)$$

where the parameter ε is like a *Péclet* number, and measures the ratio of the magnitude of the convective flux to the magnitude of the diffusive flux,

$$\boxed{\varepsilon = \frac{11}{140} \frac{V_{\max}^2 \eta_0 a}{\sigma D} \left(\frac{a}{R} \right)^2}. \quad (3.13)$$

Alternatively, the parameter ε can be thought of as a measure of the inhomogeneity of the particle distribution, since $\varepsilon = 0$ corresponds to the diffusion dominated regime, and therefore to a homogeneous particle distribution.

The full, time-dependent solution of the conservation equation can be easily calculated using a Bessel-Fourier expansion of ϕ . In this form, however, the qualitative features of the microstructure are obscured. We choose instead to look at the long-time, steady-state solution to gain a deeper intuitive feeling for how the flow affects the particle distribution.

3.2.1 Steady-state Particle Distribution $\phi^{ss}(\hat{r})$

The steady-state solution of (3.12) is reached when the convective and diffusive flux balance. Integrating the right-hand side of (3.12) once, and enforcing zero flux across the axis, we arrive at the first-order ordinary differential equation,

$$\frac{\partial \phi}{\partial \hat{r}} = -2\varepsilon \hat{r} \phi.$$

The steady-state particle distribution is therefore Gaussian,

$$\phi^{ss}(\hat{r}) = C_0 \exp[-\varepsilon \hat{r}^2].$$

The integration constant C_0 is determined by enforcing the conservation of the total particle mass. With the initial particle volume fraction ϕ_0 , conservation of the total mass requires that

$$\int_0^1 \hat{r} \phi_0 d\hat{r} = \frac{\phi_0}{2} = \int_0^1 \hat{r} \phi^{ss}(\hat{r}) d\hat{r}, \quad (3.14)$$

or,

$$C_0 = \frac{\varepsilon \phi_0}{1 - e^{-\varepsilon}}.$$

Equation (3.14) tacitly assumes that the packing of particles along the axis can be arbitrarily tight. That is not the case, and while the particle density must certainly be less than 1, in practice complete packing is rarely achieved. Let ϕ_{\max} be the maximum volume fraction possible, then (3.14) holds as long as $C_0 \leq \phi_{\max}$. If a completely packed core develops along the axis, extending some distance \hat{r}_c from the center line, then the steady-state distribution will be piece-wise defined. We modify the derivation of the particle distribution function to account for the impenetrable core by requiring that $u_m(r)$ vanishes at r_c ,

$$u_m(\hat{r}) \mapsto u_m(\hat{r}) - u_m(\hat{r}_c),$$

and by requiring that ϕ^{ss} reach its maximum at $\hat{r} = \hat{r}_c$ (*i.e.* that $\frac{\partial \phi}{\partial \hat{r}}$ is continuous at $\hat{r} = \hat{r}_c$). The resulting steady-state particle distribution outside the core is,

$$\phi^{ss}(\hat{r}) = \phi_{\max} \exp \left[\int_{\hat{r}_c}^{\hat{r}} \frac{(u_m(\hat{r}') - u_m(\hat{r}_c))}{D} d\hat{r}' \right] \quad (\hat{r} \geq \hat{r}_c).$$

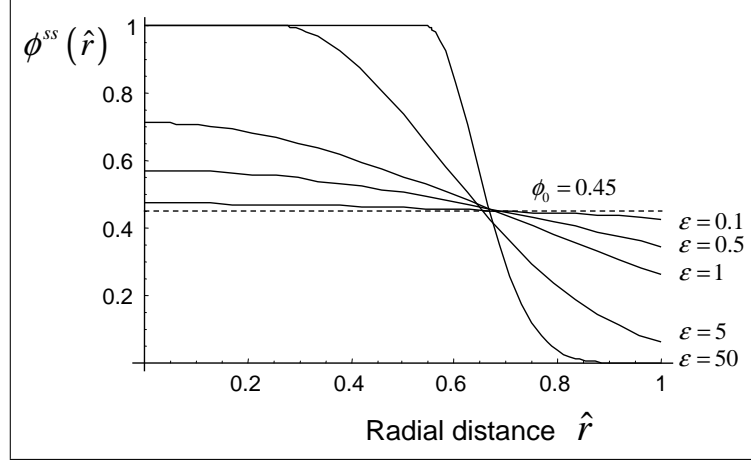


Figure 3.5: **Steady-state particle distribution.** As the flow rate increases (*i.e.* as ε increases), a dense core develops along the axis. For the purposes of illustration, $\phi_{max} = 1$.

Writing the full steady-state distribution with a core as a piece-wise function, we have

$$\phi^{ss}(\hat{r}) = \begin{cases} \phi_{max} & 0 \leq \hat{r} \leq \hat{r}_c \\ \phi_{max} \exp[-\varepsilon(\hat{r} - \hat{r}_c)^2] & \hat{r}_c < \hat{r} \leq 1. \end{cases}$$

The location of the core edge \hat{r}_c is determined by the conservation of total mass, *i.e.*

$$\begin{aligned} \int_{\hat{r}_c}^1 \hat{r} \phi^{ss}(\hat{r}) d\hat{r} &= \phi_{max} \int_{\hat{r}_c}^1 \hat{r} \exp[-\varepsilon(\hat{r} - \hat{r}_c)^2] d\hat{r} \\ &= \frac{\phi_0 - \phi_{max} \hat{r}_c^2}{2}, \end{aligned}$$

although the equation is transcendental and must be solved numerically.

Figure 3.5 illustrates the effect of ε on the steady-state particle distribution. At low ε , the flow is homogeneous across the vessel. With increase in ε , due to any number of mechanisms (increase in flow rate, increase in particle deformability, decrease in the vessel diameter, *etc.*), the particle distribution becomes more inhomogeneous. Once the maximum packing density is reached along the axis, a core develops. A *core-annular* model

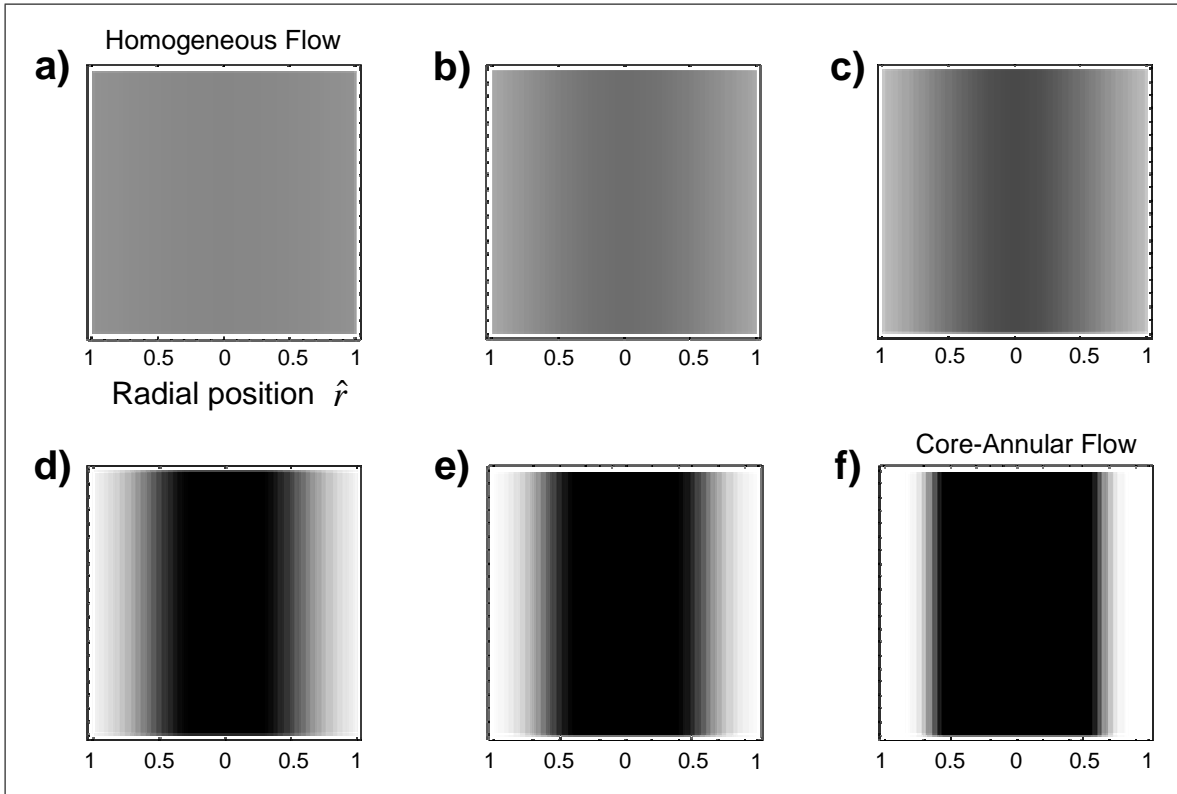


Figure 3.6: **Density plot of the steady-state particle distribution.** The microstructure is made more obvious by considering the density plot of ϕ . **a)** $\varepsilon = 0.1$ - The particles are distributed homogeneously. (Flow is along the vertical.) **b)** $\varepsilon = 0.5$ **c)** $\varepsilon = 1$ **d)** $\varepsilon = 5$ **e)** $\varepsilon = 10$ **e)** $\varepsilon = 50$ - The core-annular flow is fully developed.

Here, and henceforth, plots across the entire tube will be labeled symmetrically along the horizontal with the axis at $r = 0$.

is not appropriate, however, unless ε is very large and the particle density in the depleted layer vanishes.

The limitation of core-annular flow models is the uncertainty in the measured width of the core - a very difficult parameter to extract from observations since the edge is not well defined. Figure 3.6 is a plot of the steady-state particle distribution again, but now as a density plot. It would seem that the core is *thicker* in panel **f**) as compared with panel **d**). Assuming a core-annular flow, one would then conclude that the flow illustrated in **d**) has a lower apparent viscosity. That conclusion is false, although a layered-fluid model does not contain enough detail to make the contradiction obvious. By using \hat{r}_c to parameterize the entire flow, layered-fluid models ignore the continuous distribution of particulate outside the core. A single scalar is too coarse a measure of the complicated underlying mechanism. In the next chapter, we consider the effect of the steady-state particle distribution $\phi^{ss}(\hat{r})$ on the overall suspension flow by deriving a continuous local viscosity distribution in a generalized Newtonian constitutive equation.

Chapter 4

Overall suspension flow

In the previous chapter we developed a conservation equation governing the particle volume fraction distribution $\phi(\hat{r}, t)$, using a convective flux term from Chan and Leal [18] for deformable drops in unidirectional creeping flow. Having derived the steady-state particle distribution $\phi^{ss}(\hat{r})$, in the present chapter we assume a generalized Newtonian constitutive equation to calculate the effect of the particle microstructure on the overall suspension velocity field. Comparing the resulting flow rate with an analogous homogeneous fluid, we define an effective viscosity for the suspension.

4.1 Suspension flow and the effective viscosity

To connect the particle microstructure with the overall flow, we must decide upon a constitutive equation that relates the microscopic momentum transfer, mediated by the suspended particles, to the macroscopic flow. We are aided by our focus on the steady-state since in the long-time limit, the particle distribution is constant along the vessel, depending only upon the radial coordinate \hat{r} . We imagine the suspension as infinitesimally thin laminae of homogeneous particle distributions rolled concentrically around the axis, and model momentum transfer between laminae using the simplest expression – the generalized Newtonian constitutive equation [71],

$$\tau(\hat{r}) = \eta_\phi \frac{\partial u}{\partial \hat{r}},$$

where η_ϕ is the effect of the particle volume fraction on the local viscosity of the suspension. We leave the form of η_ϕ undefined for the moment, except to emphasize again that in the steady-state, η_ϕ will depend upon the radial distance only: $\eta_\phi(\hat{r})$. We ignore sedimentation of the red blood cells, which amounts to assuming the suspension has uniform mass density ρ_0 . As we showed in Chapter 2, with a generalized Newtonian stress-tensor the creeping flow equations reduce to,

$$\frac{dP}{dz} = \frac{1}{\hat{r}} \frac{\partial}{\partial \hat{r}} \left\{ \hat{r} \left(\eta_\phi(\hat{r}) \frac{\partial u}{\partial \hat{r}} \right) \right\}.$$

For constant pressure-driven flow¹, the velocity profile is (*cf.* (2.12)),

$$u(\hat{r}) = -\frac{1}{2} \left(\frac{dP}{dz} \right) \int_{\hat{r}}^1 \frac{\hat{r}_1}{\eta_\phi(\hat{r}_1)} d\hat{r}_1. \quad (4.1)$$

The effective viscosity of blood is often reported in experiments [47]. To make sense of this data, we must ask what is meant by the effective viscosity of a suspension - after all, viscosity is a bulk property of homogeneous fluids, while suspensions are necessarily inhomogeneous. The instruments used to measure blood viscosity often rely upon a linear relationship between dependent and independent variables, with the viscosity appearing in the proportionality constant when the measured fluid is homogeneous. For example, in a capillary viscometer the flow rate Q is measured as a function of the pressure drop ΔP along the tube of length L . Assuming the fluid is homogeneous, and the flow is laminar, the effective viscosity is defined by the ratio

$$\eta_{eff} \triangleq \frac{\pi}{8L} \frac{\Delta P}{Q}.$$

The flow rate is the volume of fluid passing through a cross-section of the tube per unit time, calculated by integrating the velocity of the flow over the cross-sectional area of the conduit,

$$Q = 2\pi \int_0^1 \hat{r} u(\hat{r}) d\hat{r}. \quad (4.2)$$

¹In Appendix B, the derivation is repeated for a weakly pulsatile driving pressure.

Using the velocity distribution calculated above, and comparing the flow rate to that of an analogous homogeneous fluid, we define the effective viscosity as (*cf.* (2.17) on p. 28)

$$\eta_{eff}(\varepsilon) = \frac{1}{8} \left[\int_0^1 \hat{r} \left[\int_{\hat{r}}^1 \frac{\hat{r}_1}{\eta_\phi(\hat{r}_1)} d\hat{r}_1 \right] d\hat{r} \right]^{-1}. \quad (4.3)$$

As in core-annular flow, the effective viscosity is a particular kind of averaged local viscosity - particular to the geometry of the viscometer. That is one of the reasons for the great variety of blood viscosity values reported in literature. *The effective viscosity is not an intrinsic property of a suspension, but depends upon the underlying flow-induced microstructure and upon the averaging implicit in the instrument used to make the measurement.*²

In order to present explicit plots of $\eta_{eff}(\varepsilon)$, $\phi^{ss}(\hat{r})$ and the resulting velocity distribution $u(\hat{r})$, we must choose the particular form of $\eta_\phi(\hat{r})$. One of the most common expressions is the general expression of Roscoe derived in the context of concentrated homogeneous suspensions,

$$\eta_\phi(\hat{r}) = \eta_0 \left(1 - \phi^{ss}(\hat{r})/\phi_{max} \right)^{-T}. \quad (4.4)$$

With specific choices of ϕ_{max} and T , (4.4) reproduces the popular expressions of Roscoe [75], Brinkman [12], Dientenfass [26], and others [53, 69, 71]. In using the expression above, we assume that at each radial position \hat{r} , the suspension is a locally homogeneous Newtonian fluid. The non-Newtonian behaviour of the flow is then a result of the combined effect of each microscopic lamina on the overall suspension velocity. The choice of Roscoe's expression is for illustrative purposes only, and was made largely to remain consistent with the past work of Phillips *et. al* [71]. We must emphasize that this choice *will not qualitatively affect any of the results in the following* and in fact *any* monotonically increasing function $\eta(\phi)$ would serve as well.

Despite the general form of the local viscosity given by (4.4), certain features of the model can be made obvious by examining the small ε limit. Consider the velocity profile

²In Chapter 6, we re-derive the particle distribution and velocity field in a concentric-cylinder geometry, such as one finds in a Couette viscometer, and we find a very different expression for the effective viscosity.

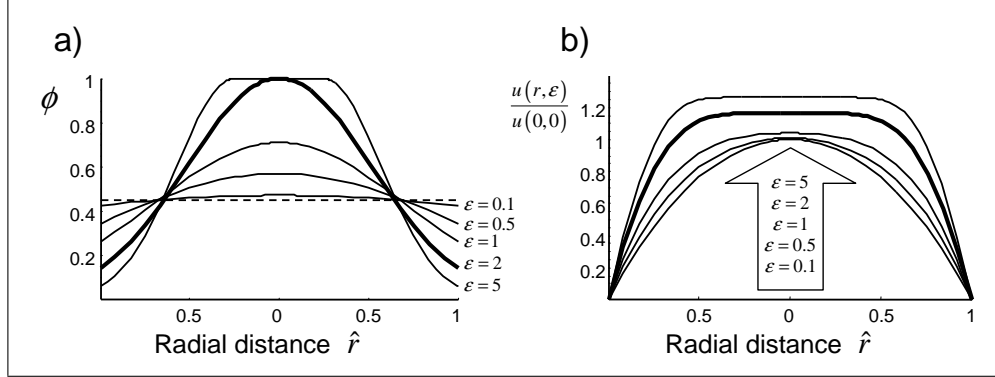


Figure 4.1: **Velocity profile of a concentrated suspension in tube flow.** **a)** The steady-state particle distribution, with the core developing at $\varepsilon \approx 2$ (bold). **b)** The resulting velocity field, normalized with respect to the centerline velocity of the parabolic profile ($\varepsilon = 0$). The velocity profile is flattened near the axis even prior to the formation of the core. For comparison, the velocity field corresponding to $\varepsilon = 2$ is also shown in bold. (The lowest plot corresponds to $\varepsilon = 0.1$.)

(4.1),

$$u(\hat{r}) \sim -\frac{1}{4} \left(\frac{dP}{dz} \right) \frac{1}{\eta_0 (1 - \phi_0/\phi_{max})^{-T}} \left\{ (1 - \hat{r}^2) + \frac{\varepsilon T}{2} \frac{(\phi_0/\phi_{max})}{(1 - \phi_0/\phi_{max})} (1 - \hat{r}^2) \hat{r}^2 + O(\varepsilon^2) \right\},$$

as $\varepsilon \rightarrow 0$. The underlined term represents a correction to the parabolic profile of homogeneous Poiseuille flow, and results in a blunt distribution along the axis. For the sake of illustration, and to make contact with experimental results in the next chapter, we must choose an explicit value for ϕ_{max} and T . Red blood cells are quite flexible and several investigators have reported flow of very concentrated suspensions ($\phi_0 > 0.95$). It seems reasonable, therefore, to set $\phi_{max} = 1$ so that the viscosity stays finite for any physically accessible hematocrit. The exponent T is more open to interpretation. Experimental evidence suggests that T is around 2, but there is a great deal of variation from data set to data set [50]. We will choose the value $T = 1.8$ to remain consistent with the work of Krieger [53] and Phillips *et al.* [71].

With an explicit choice for ϕ_{max} and T , the full velocity profile, with numerically

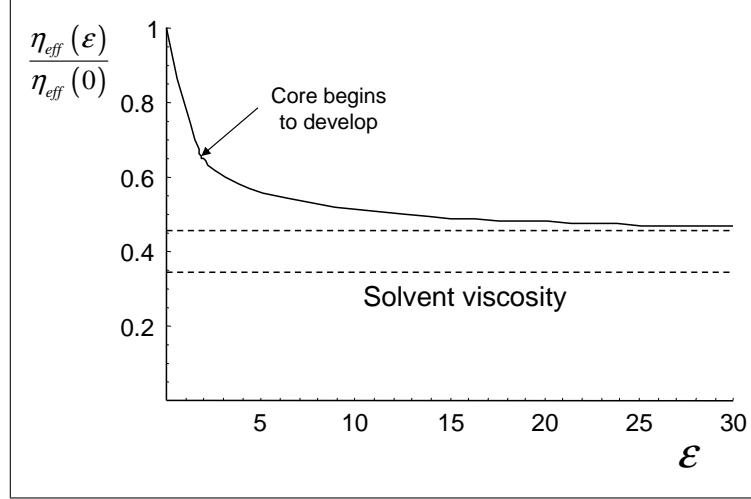


Figure 4.2: **Effective viscosity of a concentrated suspension in tube flow.** As the particles are redistributed to the axis, the apparent velocity falls. At very high ε , the core is fully developed and blood flows like a low-viscosity Newtonian fluid.

computed \hat{r}_c at high ε , is shown in Figure 4.1, with a comparison to the particle density distribution $\phi^{ss}(\hat{r})$. The increased density of particulate near the axis leads to an increase in the local viscosity and a consequent *flattening* of the velocity profile, even prior to the formation of a core.

It is also helpful to look at the small- ε expansion of the effective viscosity. Substituting (4.4) into (4.3), retaining linear terms in ε , we are able to calculate the effective viscosity of a *nearly homogeneous* suspension flow,

$$\eta_{eff} \sim \eta_0 \left(1 - \phi_0/\phi_{max}\right)^{-T} \left\{1 - \frac{\varepsilon T}{6} \frac{(\phi_0/\phi_{max})}{(1 - \phi_0/\phi_{max})} + O(\varepsilon^2)\right\},$$

as $\varepsilon \rightarrow 0$. We see that the effect of the flow (i.e. $\varepsilon > 0$) is to *reduce* the effective viscosity (shear-thinning), and that this effect is most pronounced for suspensions near maximal packing density ($\phi_0 \approx \phi_{max}$). In the dilute limit $\phi_0 \rightarrow 0$, we recover Einstein's relation with a correction due to the flow,

$$\eta_{eff} \sim \eta_0 \left[1 + \frac{\phi_0}{\phi_{max}} T \left\{1 - \frac{\varepsilon}{6}\right\}\right],$$

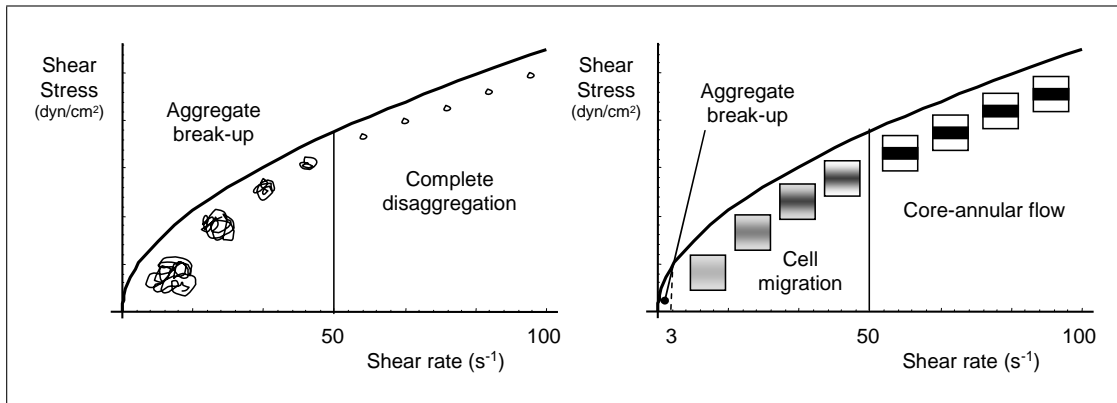


Figure 4.3: **Contrast with the standard picture of blood rheology.** **a)** In the standard picture, the decrease in the effective viscosity is attributed to the break-up of red blood cell aggregates, with a constant viscosity reached when only singlet cells remain. Redrawn from Figure 2.2 on p. 24 of the text by Charm and Kurland [20] (see also [59]) **b)** By contrast, here we propose that aggregate break-up plays a role only at very low shear rates, and that restructuring of the particle distribution in the flow is the major determinant of flow rheology, with a constant effective viscosity observed when a core-annular flow is developed.

as $\varepsilon \rightarrow 0$ and $\phi_0 \rightarrow 0$.

With $\phi_{max} = 1$ and $T = 1.8$, the full effective viscosity expression plotted as a function of ε is shown in Figure 4.2. The effective viscosity decreases as ε increases. At about $\varepsilon = 2$, a core develops along the axis (*cf.* Figure 3.5, p. 49), and the viscosity decreases more slowly while the core widens. At large ε , the core-annular flow is fully developed and the effective viscosity is constant.

The usual view of blood rheology [20, 64] is depicted in Figure 4.3a, redrawn from the textbook by Charm and Kurland [20]. The viscosity decreases as aggregates of red blood cells are broken up, with a constant viscosity reached when only singlet red blood cells remain. The observed layering of the flow is treated as an incidental consideration. In fact, Charm and Kurland go further when discussing the use of capillary viscometers to study blood rheology:

It is possible to express wall shear rate and stress from pressure-velocity measurements in capillary tubes by making the following assumptions:

1. Steady flow.
2. No radial components of velocity.
3. Axial velocity is a function of distance from the axis only.
4. *No slippage or marginal layer at the wall.*
5. No end effects.
6. Isothermal conditions.
7. Fluid incompressible.
8. No external forces.

...In the absence of a marginal layer, the capillary tube is a perfectly suitable instrument for blood viscometry. (p. 59 of [20])

Even assuming that a homogeneous cell distribution simplifies the theoretical treatment somewhat, it is not clear that such measurements have any physiological relevance whatsoever.

Though a popular view, it is simply not supported by experimental observation of blood flow - suspensions of aggregating and non-aggregating cells behave *identically* above shear rates of about $3s^{-1}$. An alternative picture (Figure 4.3b) brings the flow microstructure to the forefront, with a constant viscosity reached when the particles are maximally packed along the axis, and the core-annular flow is fully developed.

Although cell migration and an inhomogeneous viscosity distribution seems consistent with observation, the value of the model must be measured by its quantitative agreement with experimental data. In the next chapter we compare model predictions under a variety of conditions with available experiments, and for sufficiently low tube Reynolds number, we find that the model reproduces the observed rheology very well.

Chapter 5

Comparison with experiments

Having fully specified the form of the local viscosity, we will apply the model in two ways. First, we shall use ε as a free parameter, using the model to reconstruct complete velocity profile information from a couple of data points, or from the experimental flow rate. Second, using the physical interpretation of ε afforded by equation (3.13), we shall calculate the effective interfacial tension and the shear-dependent diffusion rate of red blood cells in tube flow.

5.1 Fitting of incomplete data

Non-invasive measurement techniques such as magnetic resonance imaging (MRI) are being used to estimate the wall shear stress in physiological flow. Unfortunately, the spatial resolution of these techniques is limited, and sub-pixel data estimation is necessary, often with data near the wall fitted to a paraboloid [67]. With the present model, using ε as a free parameter, we can reconstruct missing data and estimate the wall shear stress with far greater precision than is possible with a parabolic fit.

Figure 5.1 shows the velocity profile fitted to two data points half-way between the axis and the wall (filled circles). These data points and those shown as open circles are taken from the observed flow of a concentrated suspension of ghost red blood cells through a narrow glass tube (Figure 5 of [39]). The dashed line is the parabolic fit through the same two points. The inset shows that a parabolic fitting function underestimates the wall shear

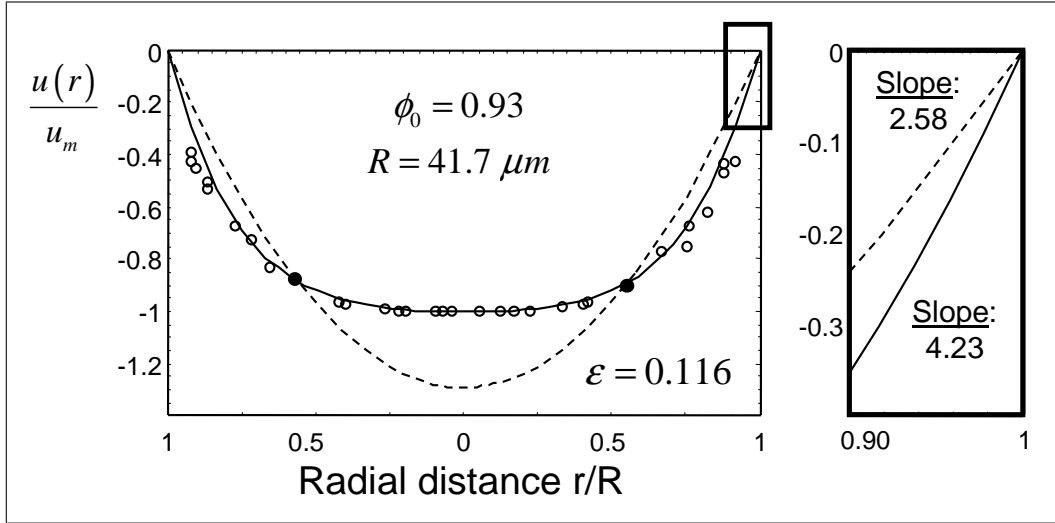


Figure 5.1: Using ε as a fitting parameter-Wall shear stress.

Estimating the wall shear stress from incomplete data. The model parameter ε is fitted to two points (filled circles) The missing data is shown as open circles. The parabolic fit (dashed) underestimates the wall shear stress by a factor of 1.6 [Inset].

stress (which is proportional to $u'(r)$) by about 160%.

Alternatively, ε can be determined by matching the model to the experimentally determined flow rate, via (4.2). Since $\eta(r)$ is a function of ε , so too will $u(r)$. Integrating over the cross-section of the tube, we obtain the flow-rate as a function of ε , $Q(\varepsilon)$. Comparing $Q(\varepsilon)$ to the experimental flow rate Q_{exp} , we are able to determine the choice of ε that will reproduce the observed flow rate. With ε so determined, we plot $u(r; \varepsilon)$, and the velocity profile is reconstructed exactly (Figure 5.2). Here again the data points (filled circles) are taken from ghost cell flow through glass tubes (Figure 5 of [39]). Note that $u(r; \varepsilon)$ is *not* fit to the data points – ε is simply chosen to match the *flow rate*. The close agreement between the model and data lends credence to the mathematical form of the velocity function.

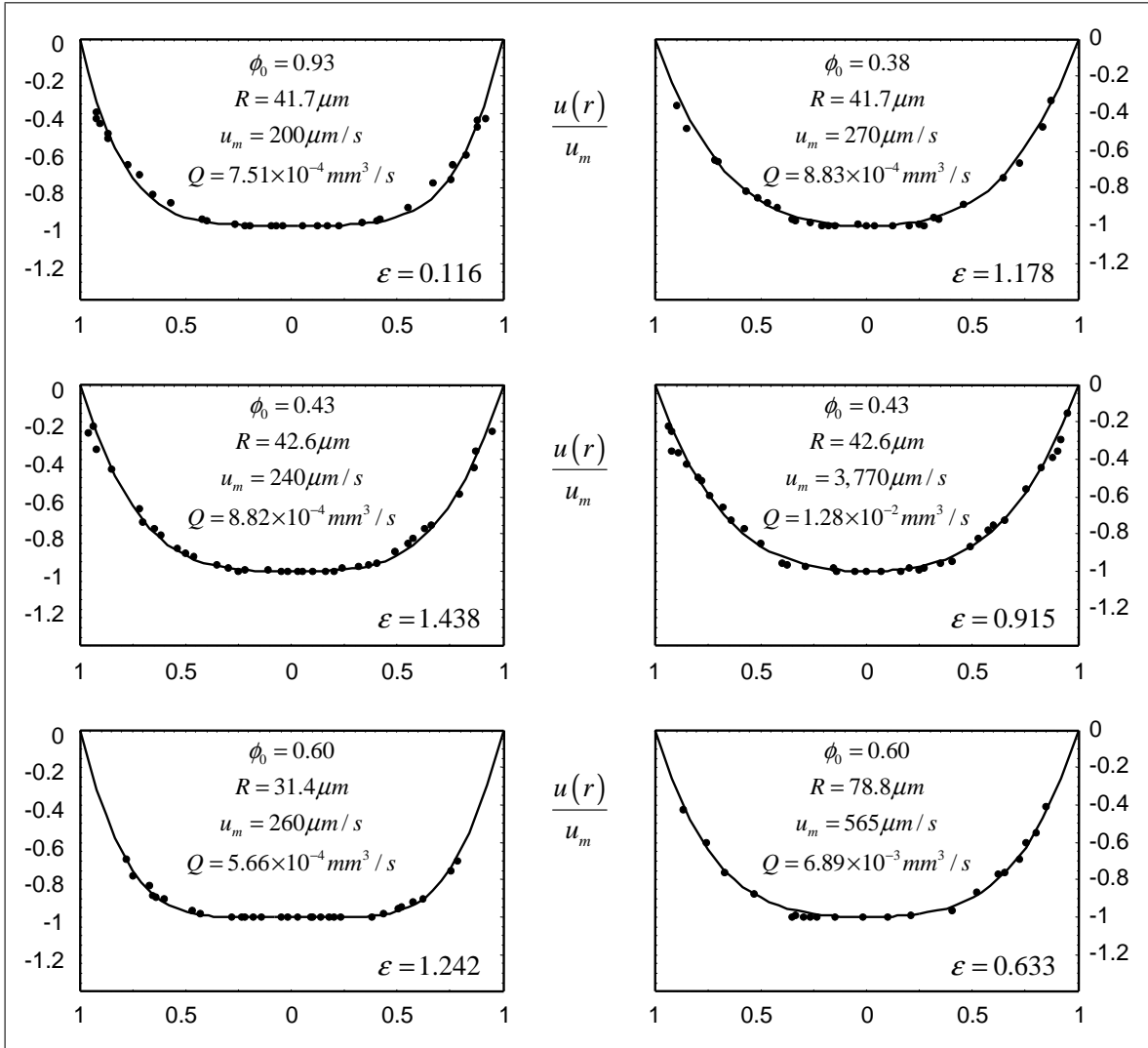


Figure 5.2: Using ε as a fitting parameter-Velocity profiles.

Fitting ε to the experimental flow rate. Given the centerline velocity u_m , the hematocrit ϕ_0 and the tube radius R the model parameter ε is chosen so that (4.2) matches the experimental flow rate. Here the velocity data is shown as filled circles and the model prediction as a solid line. (All data is from [39] for ghost red cells flowing through glass tubes.)

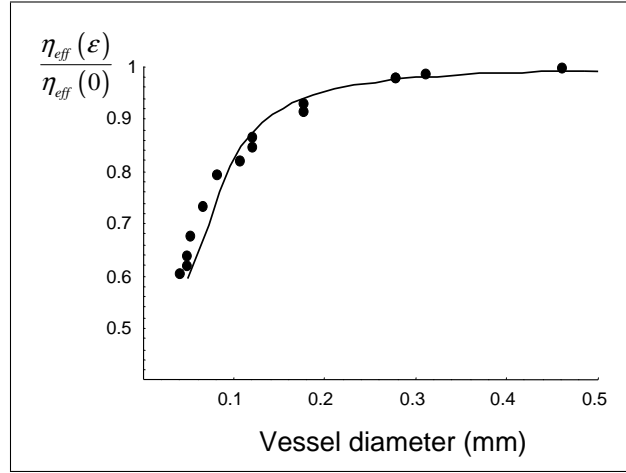


Figure 5.3: **Comparison with the data of Fahraeus and Lindqvist.** The original data of Fahraeus and Lindqvist [33] is shown as filled circles, with the limiting viscosity normalized to one. The model parameter ε is proportional to R^{-2} , and the effective viscosity (4.3) calculated with $\varepsilon = 0.2R^{-2}$ (R measured in mm) is shown as a solid line.

5.2 Semi-qualitative rheology

The Fahraeus-Lindqvist Effect

The definition of ε (3.13) allows the reproduction of the anomalous flow behavior of blood by fixing various combinations of physical parameters. For example, we see that for a given experimental set-up, $\varepsilon \propto R^{-2}$. Fitting the original data of Fahraeus and Lindqvist [33] (normalized to unity at large vessel diameter), we can fix the proportionality constant to their particular experimental set-up,

$$\varepsilon = \frac{0.2}{R^2},$$

with the tube radius R measured in mm . The resulting fit to the experimental data using the effective viscosity calculated using (4.3) is shown in Figure 5.3 – the decrease in the observed viscosity is reproduced very well.

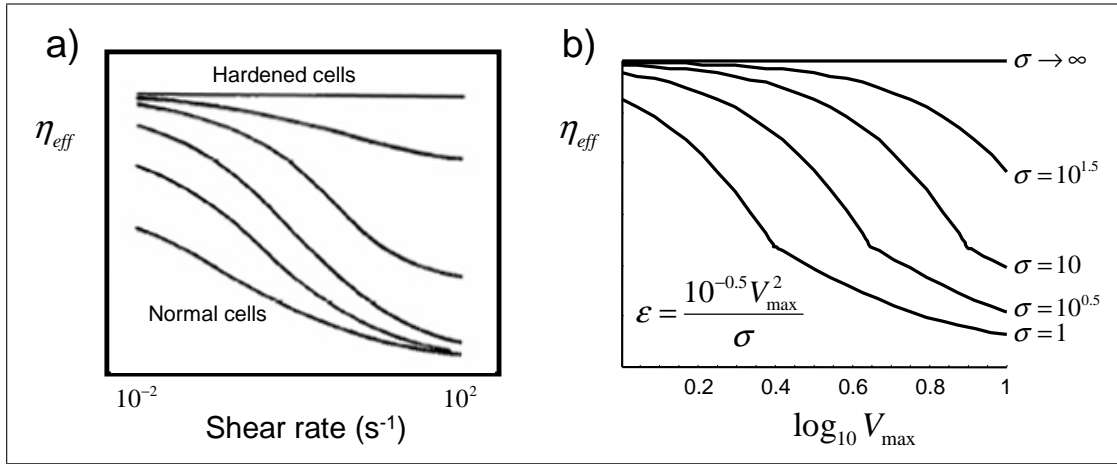


Figure 5.4: **Shear-thinning and cell hardening.** **a)** The data of Carr and Cokelet [16] illustrating the effect of cell hardening on shear-thinning in blood. **b)** The qualitative behavior is reproduced by the model. The shear rate is proportional to V_{max} and the ‘hardness’ of the blood cells is expressed by the interfacial tension σ . Here, $\varepsilon = \frac{10^{-0.5} V_{max}^2}{\sigma}$. For an alternate explanation of the observed behaviour, see the comment following the next section.

Shear-thinning and the effect of cell hardening

Carr and Cokelet [16] examined the effect of shear rate *and* cell deformability on the observed viscosity of blood. A qualitative plot of their results is shown in Figure 5.4a. We can compare the model prediction with their results by writing ε as a function of the shear rate (expressed through the centerline velocity V_{max}) and the interfacial tension σ ,

$$\varepsilon \propto \frac{V_{max}^2}{\sigma}.$$

The qualitative behavior is reproduced by the model for nominal choices of V_{max} and σ . The discontinuity in the second derivative of the theoretical plot marks the point where the core begins to develop in the particle density distribution, an artifact that is amplified by the logarithmic scale.

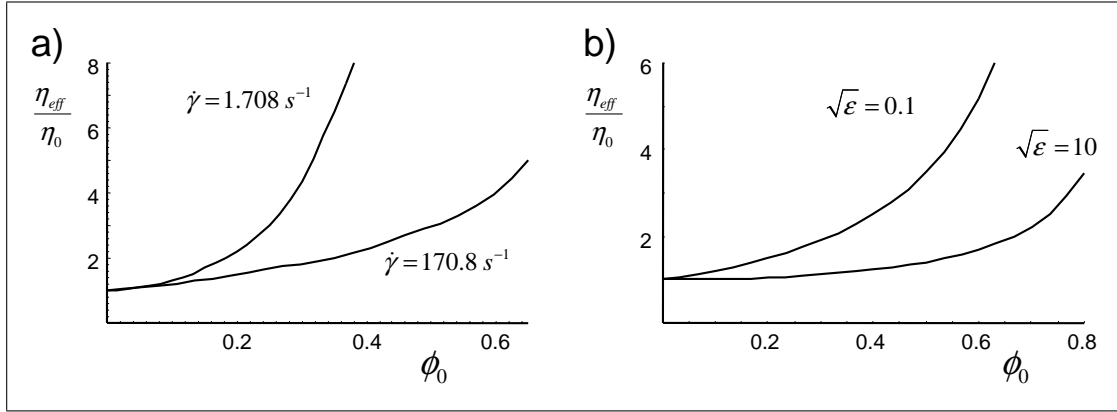


Figure 5.5: **The effect of shear on the volume fraction dependent viscosity.** a) A plot of the effective viscosity as a function of cell volume fraction is sensitive to the shear rate at which the measurements are made [13]. b) The model reproduces the same trend, where $\dot{\gamma} \propto \sqrt{\varepsilon}$. For an alternate explanation of the observed effect, see the text at the end of this section.

The effect of shear rate on the effective viscosity

In Chapter 2, we remarked that experiments correlating data using Roscoe's expression $\eta = \eta_0 \left(1 - \frac{\phi}{\phi_{max}}\right)^{-T}$ produce enormous spread in the characterization of ϕ_{max} and T . The problem, as pointed out by Jeffrey and Acrivos [50], is that the form of the viscosity expression is not rich enough to capture the underlying physical mechanisms responsible for the observed rheology. The two free parameters represent a collection of physical properties assembled in some unknown way. For example, the rate of divergence of the measured viscosity decreases as the shear rate increases. Several investigators therefore propose to make ϕ_{max} and T empirical functions of the shear rate, but this is a stopgap solution. Although some hindsight rationalizations are offered to justify the *ad hoc* modification of the fitting function, such as cell shape changes in response to flow [13, 69], or circulation of a liquid cell membrane [26], the evidence offered in their support is largely indirect. Calculating the effective viscosity using a spatial average of the local viscosity obviates any modification of ϕ_{max} or T .

Shear-thinning is apparent in the plot of the effective viscosity as a function of the

average cell volume fraction (the hematocrit ϕ_0) at various shear rates (Figure 5.5a). Since ε is directly related to the square of the shear rate (through V_{max}), a plot of η_{eff} as a function of ϕ_0 at various values of $\sqrt{\varepsilon}$ should show the same behavior - as indeed it does, even with ϕ_{max} and T fixed (Figure 5.5b).

Pal [69] derives a model exhibiting the same qualitative behaviour shown above in Figures 5.4 and 5.5. His method follows Roscoe's approach [75] (outlined in Chapter 2) to extend to the concentrated regime the work of Goddard and Miller [36] on the rheology of dilute homogeneous suspensions of viscoelastic spheres (*cf.* eq. (2.6) on p. 18).

Unfortunately, the approach of Roscoe tacitly assumes a *homogeneous* distribution of particles and since there can be no doubt that red blood cells migrate in response to the background flow, it would seem a spatially uniform model is *not* appropriate for describing physiological blood flow. The same can be said of any constitutive equation derived from a spatially homogeneous distribution of particles, for example the work of Frankel and Acrivos [34]. Although such models are of great use in the study of the behaviour of a *static* distribution of viscoelastic inclusions in a composite material, the marginal layer and spatial non-uniformity of the particle distribution plays a dominant role in suspension *flow* [4]. In summary, past models of blood flow are able to reproduce the cell-deformability dependent shear-thinning observed experimentally, though the proposed mechanism (cell elongation) differs from the mechanism proposed in the present model (cell migration), and experimental evidence suggests that cell migration cannot be ignored in the modeling of blood flow.

5.3 Predictive rheology

The definition of ε is given in terms of physical parameters and should in principle allow rheological data to be predicted. There is, however, some difficulty assigning meaning to the constants V_{max} and D , along with the interfacial tension σ .

The migration velocity (3.10) was derived by Chan and Leal in terms of the motion of a *single* drop in a unidirectional flow, so the background flow will not be affected by the motion of the drop. For a concentrated suspension, redistribution of the particles by the background flow will change the suspension flow geometry in an essential way. For example,

the maximum flow velocity along the axis u_m is no longer related to the shear gradient near the wall via Poiseuille's law and therefore cannot be identified as V_{max} . Nevertheless, in the vicinity of the wall where drop migration is dominant we can determine the parabolic contribution to the shear gradient by taking a Taylor expansion of the fluid flow velocity (4.1) at $r = 1$, retaining quadratic terms, to find

$$V_{max} = \frac{u_m}{2\eta(1) \int_0^1 \frac{r' dr'}{\eta(r')}}.$$

In this way, we are able to connect the centerline velocity u_m to the mean-field shear gradient that an individual particle will experience near the wall, and hence calculate the cross-stream migration velocity. With V_{max} expressed in terms of experimentally accessible quantities, the remaining parameters D and σ are left to fully characterize ε .

Diffusion of an individual particle in a concentrated suspension is enhanced by the flow (shear-induced diffusion [52, 58]) and constrained by the close-packing of neighboring particles (cage effects [24]). In general, these contributions will not be uniform across the vessel, but as a first approximation we consider D as a *spatially homogeneous* function of ε (the flow) and ϕ_0 (the average packing fraction). For simplicity¹, we assume a polynomial in ε and ϕ_0 . Since ε can be fitted to flow rate data as in Figure 5.2, we will use the data of Goldsmith and Marlow to determine $D(\varepsilon, \phi_0)$ such that the variance in σ is minimized². Considering a second-order polynomial fitting function, we arrive at the empirical diffusion coefficient

$$D(\varepsilon, \phi_0) = 1 - 3.77 \varepsilon \phi_0 + 3.7 \varepsilon^2 \phi_0^2,$$

where D_0 is the Einstein-Stokes diffusion constant,

$$D_0 = \frac{kT}{6\pi\eta_0 a}.$$

¹The form of the fitting function will be discussed in Chapter 7.

²Data is taken from Figure 5 of [39], excluding Figure 5b (right) since the tube Reynolds number is too large in that experiment. To ensure that the suspension flow is adequately modeled by the creeping flow equations, we require that the tube Reynolds number $\frac{u_m 2R\rho_0}{\eta_0}$ be less than 0.05. The two fitting parameters in the polynomial are calculated by determining the minimum of the variance in σ using the `FindMinimum` command in *Mathematica*[®].

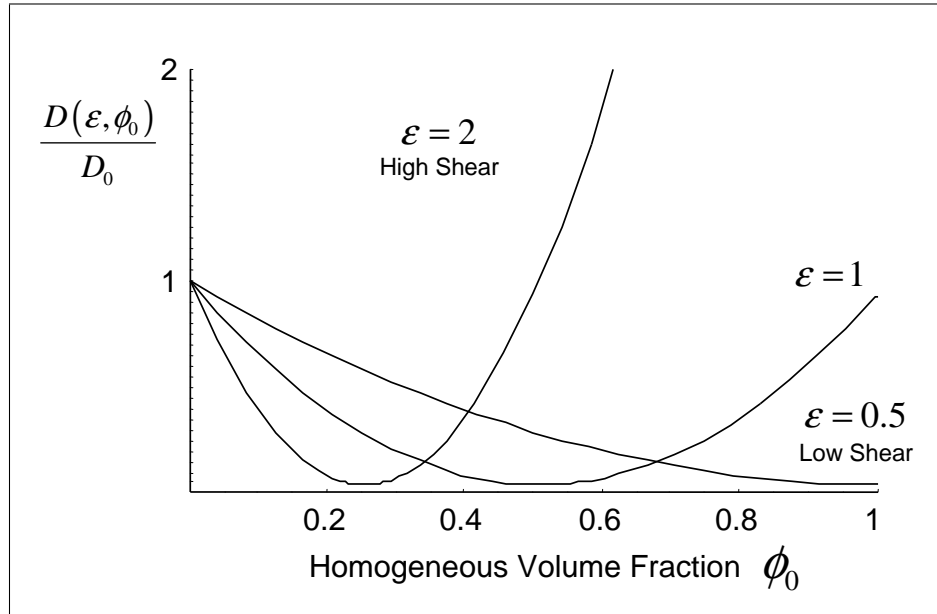


Figure 5.6: **The effect of shear and particle packing on the diffusion rate.** The empirical diffusion rate coefficient $D(\varepsilon, \phi_0) = 1 - 3.77 \varepsilon \phi_0 + 3.7 \varepsilon^2 \phi_0^2$ is dominated by cage effects at low shear ($\varepsilon = 0.5$) where close packing restricts diffusion. As the shear rate increases ($\varepsilon = 2$), asymmetric collisions among particles enhance the diffusion rate in concentrated suspensions.

Here k is Boltzmann's constant and T is the absolute temperature. Qualitatively, the diffusion constant $D(\varepsilon, \phi_0)$ behaves as one would hope (Figure 5.6): As the shear rate increases, shear-induced diffusion overcomes cage effects, increasing the apparent rate of diffusion. With this choice of $D(\varepsilon, \phi_0)$, the resulting estimate for σ is,

$$\sigma = (1.2 \pm 0.1) \times 10^{-4} N m^{-1}.$$

(Determined from the data of five experiments.) That is to say that the red blood cells *behave like deformable droplets with interfacial tension* $\sigma = 1.2 \times 10^{-4} N m^{-1}$. In reality, red cells are biconcave disks with a cell-membrane tension of about $1 \times 10^{-5} N m^{-1}$ [32], an order of magnitude less than the model σ . It is important to note that the internal architecture of the cell and the membrane itself lend an apparent rigidity opposing cell

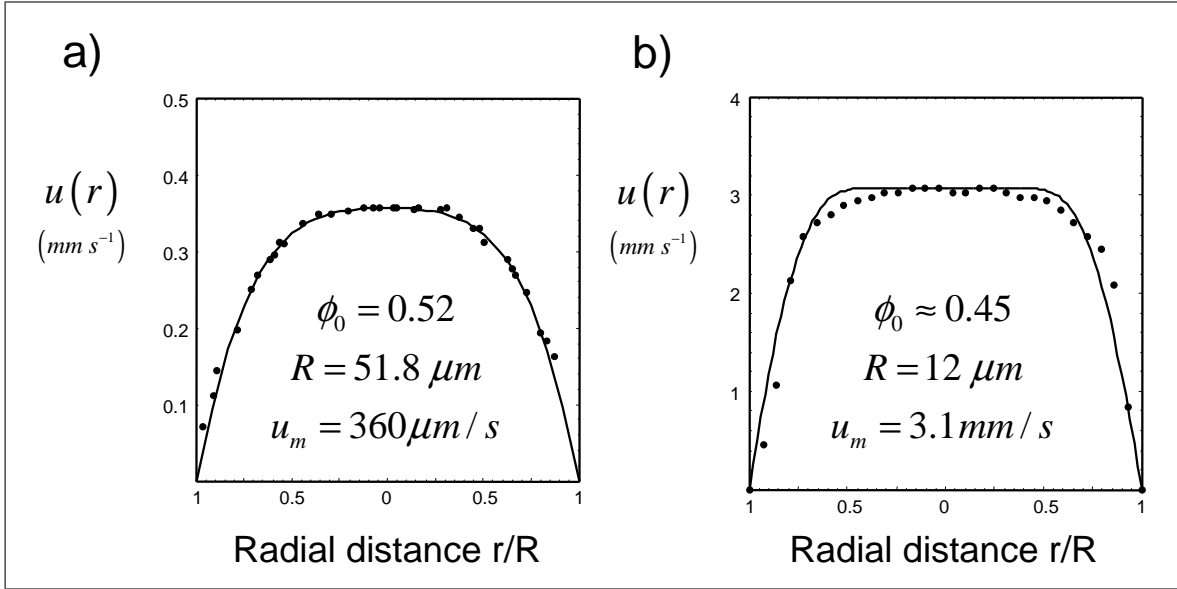


Figure 5.7: **Model prediction compared with experimental data.** a) *In vitro* data of Goldsmith and Turrito The model prediction is shown along with the data for the flow of ghost red blood cells through glass tubes [41] (A different experiment from that used to determine $D(\varepsilon, \phi_0)$). b) *In vivo* data of Sugii, Nishio and Okamoto The data is for the flow of rat's blood through an arteriole [82], with estimated hematocrit $\phi_0 = 0.45$.

deformation not found in a simple fluid drop.

Collecting V_{max} and $D(\varepsilon, \phi_0)$, we arrive at an implicit nonlinear equation for ε (cf. (3.13) on p. 47),

$$\varepsilon = \frac{11}{140} \frac{V_{max}^2(\varepsilon, \phi_0)}{\sigma} \frac{\eta_0 a}{D(\varepsilon, \phi_0)} \left(\frac{a}{R}\right)^2. \quad (5.1)$$

Here, $\sigma = 1.2 \times 10^{-4} N m^{-1}$, the nominal plasma viscosity $\eta_0 = 1.1 \times 10^{-3} kg m^{-1} s^{-1}$, and the deformed red cell radius $a = 3.5 \times 10^{-6} m$. The hematocrit ϕ_0 , vessel radius R and centerline velocity u_m depend upon the details of the particular system under investigation. To vindicate the simplifications made to develop an expression for $D(\varepsilon, \phi_0)$ and fix σ , we compare the theoretically predicted velocity profile to experimental data.

The *in vitro* data of Goldsmith and Turrito (Figure 2 of [41]) for concentrated ghost

cells in glass tubes is shown in Figure 5.7a. The experimental parameters are $\phi_0 = 0.52$, $R = 51.8\mu m$ and $u_m = 360\mu m/s$. This is all the information required to estimate the velocity profile across the tube, and the theoretical prediction fits the data very well.

In vivo data is far more difficult to collect, and human data is scarce. Nonetheless, making use of the excellent data of Sugii *et al.* (Figure 7d of [82]) for blood flowing in the small arterioles of a rat, with $R = 12\mu m$, $u_m = 3.1mm/s$ and estimated rat hematocrit $\phi_0 = 0.45$ [92] and cell radius³ $a \approx 3 \times 10^{-6}m$, we again find good agreement between the experimental results and the theoretical prediction (Figure 5.7b).

All of the experimental results presented in this chapter were obtained from tube flow. In the next chapter, we repeat the model derivation in a different flow configuration to assess the impact the measuring instrument itself has on the experimental characterization of the effective viscosity of a suspension.

³Based on the fact that the rat blood cell has a volume about 60% that the human red blood cell.

Chapter 6

Couette geometry

The model predictions compare well with the experimental results presented in the previous chapter for pressure driven suspension flow. The geometry of the flow is a fundamental consideration in the development of the model - determining the form of the migration velocity and the choice of the reference coordinate system. In the present chapter, we keep the same reference coordinate system, but alter the flow geometry to linear shear as found in a rotating cylinder (Couette) viscometer with narrow gap. In contrast with the above, the dominant contribution to the migration velocity comes from hydrodynamic interactions of the deformable particles with the walls. Consequently, the expression for the migration velocity u_m is no longer linear in the radial coordinate, but rather a singular function diverging near the confining walls. The steady-state particle distribution is obviously no longer Gaussian, and the behavior of the effective viscosity as a function of ε is essentially different. The conclusion is that the parameterization of *in vivo* models from viscometer data is not justifiable.

6.1 Measuring viscosity

Viscosity measurements of homogeneous fluids typically rely on linear experiments, insofar as the non-linear inertial terms in the Navier-Stokes equations vanish identically or are negligibly small [10, 43]. There are three main instrument configurations that produce a linear relationship between the dependent and independent variables, with the viscosity

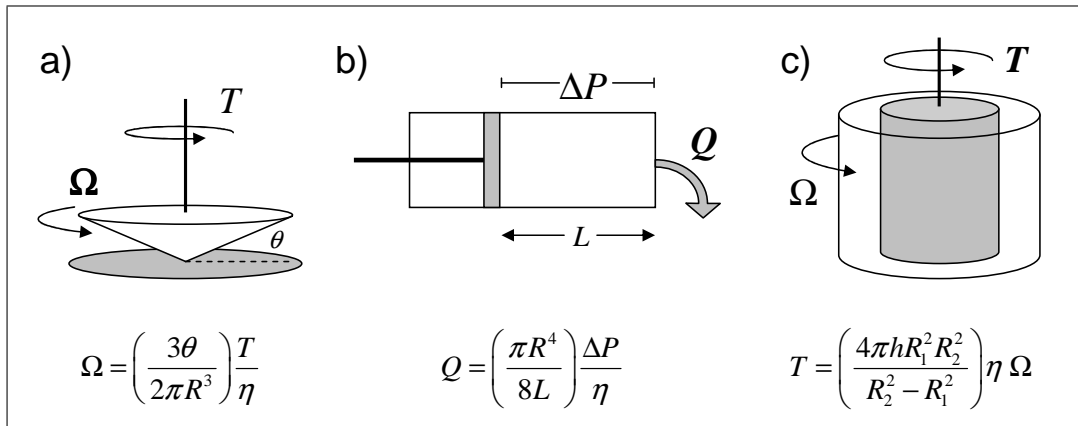


Figure 6.1: **Various viscometers.** **a) Cone-plate viscometer** The rotation speed Ω of a shallow cone is measured as a function of the applied torque T . **b) Capillary viscometer** The flow rate Q is measured as a function of the pressure drop along the tube ΔP . **c) Couette viscometer** The torque T acting on the inner cylinder is measured as a function of the rotation speed Ω of the outer cylinder.

appearing in the proportionality constant: cone-plate viscometers, capillary viscometers, and Couette (or coaxial cylindrical) viscometers (Figure 6.1). We shall briefly discuss each instrument. For the capillary and Couette viscometers, we derive the relationship between dependent and independent variables when the viscosity of the fluid is not constant.

Cone-plate viscometer

For completeness, we shall briefly discuss the cone-plate viscometer, though we shall not consider the derivation of the particle volume fraction ϕ nor the local viscosity η_ϕ in this geometry. Furthermore, it is not clear how to obtain an expression of the effective viscosity in the case of variable local particle density.

In this configuration, a cone of radius R rotates at a speed $\Omega \text{ rad s}^{-1}$ above a flat plate. The surface of the cone forms a small angle θ ($\ll 1 \text{ rad}$) with the plate (Figure 6.1a). At a distance r from the rotation axis, the velocity of a homogeneous fluid is constant across

the gap,

$$u(r) = \Omega r.$$

The shear rate $\dot{\gamma}$ is $\dot{\gamma} = \frac{u}{h}$, where h is the width of the gap, and from Figure 6.1a,

$$\dot{\gamma} = \frac{u(r)}{h} = \frac{\Omega r}{r \tan \theta} \approx \frac{\Omega}{\theta} \quad (\theta \ll 1 \text{ rad}),$$

i.e. the shear rate is constant throughout. (In a structured fluid, this will no longer be the case, but it is not clear how the derivation can be modified to accommodate a varying local viscosity). With the shear-stress tensor τ_r , the total torque T exerted on the fluid by the cone is,

$$T = \int_A \tau_r r dA,$$

where the integral is over the surface of the cone $dA = 2\pi r ds$ with ds representing the distance along the edge of the cone. Since $r = s \cos \theta$, for small θ , $ds \approx dr$ and,

$$T = 2\pi \int_0^R \tau_r r^2 dr.$$

Assuming a Newtonian stress tensor $\tau_r = \eta \dot{\gamma} = \eta \frac{\Omega}{\theta}$, the total torque is given by

$$T = \frac{2\pi\Omega}{\theta} \int_0^R \eta r^2 dr,$$

which re-arranges to,

$$\Omega = \left(\frac{3\theta}{2\pi R^3} \right) \frac{T}{\eta},$$

relating the observed rotation speed Ω to the applied torque T , and the fluid viscosity η appears in the proportionality constant.

Capillary viscometer

In a capillary viscometer the flow rate Q is measured as a function of the pressure drop ΔP along the tube of length L . The net force acting on the fluid due to the applied pressure is

$$F_p = \Delta P \pi r^2.$$

Opposing the generated motion is the shear force acting on the surface of the lamina of fluid at r ,

$$F_\tau = \tau (2\pi r) L.$$

For a steady flow, these forces balance, and¹

$$\tau = \frac{\Delta P r}{L} \frac{1}{2}.$$

Assuming a generalized Newtonian stress tensor $\tau = \eta_\phi(r) \frac{du}{dr}$,

$$\eta_\phi(r) \frac{du}{dr} = \frac{\Delta P r}{L} \frac{1}{2},$$

which is a first-order separable differential equation. Integrating both sides, along with the boundary condition $u(R) = 0$,

$$\int_0^u du = u(r) = -\frac{\Delta P}{2L} \int_0^r \frac{r dr'}{\eta_\phi(r')}.$$

In practice, it is more convenient to measure the volumetric outflow of the pipe instead of the velocity field $u(r)$ itself. The flow rate is the volume of fluid passing through a cross-section of the tube per unit time, calculated by integrating the velocity of the flow over the cross-sectional area of the conduit,

$$Q = -\frac{\Delta P}{2L} \int_0^R 2\pi r \left[\int_0^r \frac{r' dr'}{\eta_\phi(r')} \right] dr. \quad (6.1)$$

For a homogeneous fluid with viscosity η_{eff} ,

$$Q = \left(\frac{\pi R^4}{8L} \right) \frac{\Delta P}{\eta_{eff}}.$$

Comparing with (6.1), we *define* the effective viscosity of a suspension flowing through a tube as

$$\eta_{eff} = \frac{R^4}{8} \left[\int_0^R r \left(\int_0^r \frac{r' dr'}{\eta_\phi(r')} \right) dr \right]^{-1}. \quad (6.2)$$

¹From the momentum equations for an axisymmetric flow, we know the pressure drop along a tube is linear, so where we have formerly written $-\frac{dP}{dz}$, we now equivalently write $\frac{\Delta P}{L}$ to clarify the derivation.

Couette viscometer

The Couette viscometer is a popular design consisting of two coaxial cylinders: an inner cylinder of radius R_1 and height h inside an outer cylinder of radius R_2 (Figure 6.1c). The test fluid is contained between the two cylinders and multiple experiments can be made on the same sample. Consequently, this is the instrument of choice for investigations of viscoelastic and aging effects in complex fluids.

The outer cylinder rotates with a constant speed $\Omega \text{ rad s}^{-1}$, while the inner cylinder remains stationary. The torque T acting on the inner cylinder is measured by the angular deflection about the axis of rotation. If we consider the torque acting on a thin cylinder of fluid at a distance r from the axis of rotation, then

$$T = \text{Stress} \times \text{Surface Area} \times \text{Length of the Lever Arm}$$

$$T = \tau_r (2\pi r h) r,$$

or, re-arranging for the shear-stress tensor τ_r ,

$$\tau_r = \frac{T}{2\pi r^2 h}. \quad (6.3)$$

We denote by ω the angular velocity of the fluid at r , so that the velocity of the fluid in the direction of rotation is $u_\theta = \omega r$, and the shear rate is then given by

$$\frac{\partial u_\theta}{\partial r} = r \frac{d\omega}{dr},$$

Assuming a generalized Newtonian stress tensor $\tau_r = \eta_\phi(r) \frac{\partial u_\theta}{\partial r} = \eta_\phi(r) r \frac{d\omega}{dr}$, then from (6.3) it follows that

$$\frac{d\omega}{dr} = \left(\frac{T}{2\pi h} \right) \frac{1}{\eta_\phi(r) r^3}.$$

Integrating both sides²,

$$\int_0^\Omega d\omega = \frac{T}{2\pi h} \int_{R_1}^{R_2} \frac{dr}{\eta_\phi(r) r^3}. \quad (6.4)$$

²The lower limit of integration for ω corresponds to a *stationary* inner cylinder - In general, it may rotate with speed $\Omega_0 \text{ rad s}^{-1}$. If that is the case, then in the following replace Ω with $\Delta\Omega$, where $\Delta\Omega = \Omega - \Omega_0$. See Appendix C for details.

For a homogeneous fluid with constant viscosity η_{eff} , (6.4) becomes

$$T = \left(\frac{4\pi h R_1^2 R_2^2}{(R_2^2 - R_1^2)} \right) \eta_{eff} \Omega. \quad (6.5)$$

The expression in parentheses is constant for a given instrument, determined by calibration with a standard fluid. The torque T is then linearly related to the rotation speed Ω and the proportionality constant is the viscosity η_{eff} . Comparing (6.4) with (6.5), we *define* the effective viscosity of an inhomogeneous suspension as

$$\eta_{eff} = \frac{1}{2} \left[\frac{1}{R_1^2} - \frac{1}{R_2^2} \right] \left[\int_{R_1}^{R_2} \frac{dr}{\eta_\phi(r)r^3} \right]^{-1}. \quad (6.6)$$

Compare this with the corresponding expression for a capillary viscometer (6.2) - the spatial averaging implied by the measurement of an effective viscosity is very different for the two instruments. Of course, for a homogeneous fluid of viscosity η_0 , both reduce to $\eta_{eff} = \eta_0$. As we show in the next section, not only is the spatial averaging different, but $\eta_\phi(r)$, too, has a completely different behavior from $\eta_\phi(r)$ corresponding to a capillary geometry as derived in Chapter 4.

6.2 Steady-state rheology in a Couette viscometer

Our approach to the calculation of the steady-state particle distribution will be identical with that followed in Chapters 3 and 4 - We first write an expression for the migration velocity u_m and thereby construct a conservation equation for ϕ that we solve in steady-state. We assume a generalized Newtonian stress tensor and use the results of the previous section to define the effective viscosity.

For a Couette viscometer, the radii of the two cylinders are very large compared with the gap width d . In the derivation of the migration velocity u_m we are then able to approximate the flow geometry by a linear shear flow between parallel plates (Figure 6.2). The migration velocity derived in Chapter 3 applied to *unbounded* quadratic unidirectional flow. The cross-stream migration was due to gradients in the shear rate, and was $O\left(\frac{a^3}{R^3}\right)$. Now, in a linear background flow there is no gradient in the shear rate and the cross-stream migration to leading order is due to *hydrodynamic interactions with the walls*. The

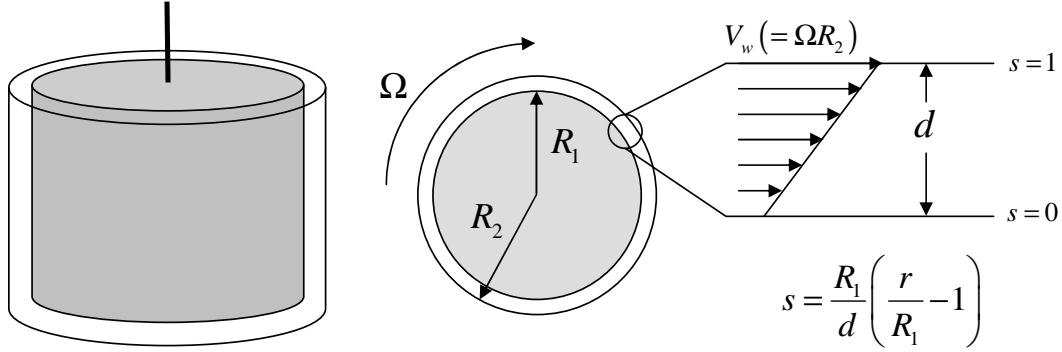


Figure 6.2: **A Couette viscometer.** Two concentric cylinders rotate relative to one another. The ratio of the rotation speed to the resultant torque acting on the inner cylinder is determined by the viscosity of a *homogeneous* fluid. The gap width d is very small compared with the radii of the cylinders, and so the local flow may be reasonably modeled as a linear shear flow between parallel plates.

mechanism is different from the mechanism in tube flow, and the velocity correction is $O\left(\frac{a^4}{d^4}\right)$ [56]. To simplify the notation, we use the dimensionless variable $s = \frac{R_1}{d} \left(\frac{r}{R_1} - 1\right)$ and write the migration velocity as [see eq. 6.13 on p. 159 of [18]],

$$u_m(s) = \frac{1}{28} \frac{V_w^2 \eta_0}{\sigma} \left(\frac{a}{d}\right)^4 \left[\frac{1}{s^2} - \frac{1}{(1-s)^2} + 2(1-2s) \right].$$

Note the expression is *singular* at the walls ($s = 0, 1$). Defining the convective and diffusive flux as before, solving the resulting conservation equation at steady-state (with the time and distance non-dimensionalized with respect to d instead of R), the particle density distribution is given by

$$\phi_{||}^{ss}(s) = C_0 \exp \left[-\bar{\varepsilon} \left(\frac{1}{s} + \frac{1}{(1-s)} - 2s + 2s^2 \right) \right],$$

where the subscript ‘||’ denotes the distribution in the parallel-plate geometry, and the parameter $\bar{\varepsilon}$ is,

$$\bar{\varepsilon} = \frac{1}{28} \frac{V_{\max}^2 \eta_0 a}{\sigma D} \left(\frac{a}{d}\right)^3.$$

The integration constant C_0 is again fixed by imposing the conservation of mass,

$$\int_{R_1}^{R_2} \phi_0 r dr = \frac{\phi_0}{2} (R_2^2 - R_1^2) = \int_{R_1}^{R_2} \phi_{\parallel}^{ss} \left(\frac{R_2}{d} \left(\frac{r}{R_1} - 1 \right) \right) r dr,$$

but it is no longer possible to calculate C_0 exactly. A good approximation can be found, however, and the steady-state particle density distribution is,

$$\phi_{\parallel}^{ss}(s) \approx \frac{\phi_0 e^{\frac{6}{5}\bar{\varepsilon}}}{e^{-2\bar{\varepsilon}} - 2\bar{\varepsilon} E_i(2\bar{\varepsilon})} \exp \left[-\bar{\varepsilon} \left(\frac{1}{s} + \frac{1}{(1-s)} - 2s(1-s) \right) \right],$$

where $E_i(z)$ is the exponential integral,

$$E_i(z) = \int_1^{\infty} \frac{e^{-zt}}{t} dt.$$

In the dilute limit, where no core has formed, we are able to compare our results with the theoretical work of Hudson [46] on dilute emulsions (Figure 6.3). His model is more complicated, including the effects of particle buoyancy and a spatially-varying diffusion coefficient. As a result, he must solve for ϕ^{ss} numerically. Unfortunately, Hudson's solutions for ϕ are unphysical since they are *negative* over a portion of the domain. Nevertheless, in regions where his ϕ is positive, our results compare well, and both agree with experimental data [46]. For a concentrated suspension, as in Chapter 4, we must include the possibility of a maximally packed core along the centerline. The core will begin to form when the maximum of ϕ_{\parallel}^{ss} exceeds ϕ_{max} , *i.e.* for $\bar{\varepsilon}$ and ϕ_0 such that

$$\frac{e^{-\frac{23}{10}\bar{\varepsilon}} \phi_0}{e^{-2\bar{\varepsilon}} - 2\bar{\varepsilon} E_i(2\bar{\varepsilon})} > \phi_{max}.$$

Dividing the migration velocity into two parts, $u_m^<(s)$ for $s \leq \frac{1}{2}$ and $u_m^>(s)$ for $s \geq \frac{1}{2}$, we require that both vanish at the edge of the core (which has radius r_c),

$$\begin{aligned} u_m^<(s) &\mapsto u_m^<(s) - u_m^<\left(\frac{1}{2} - r_c\right) \\ u_m^>(s) &\mapsto u_m^>(s) - u_m^>\left(\frac{1}{2} + r_c\right). \end{aligned}$$

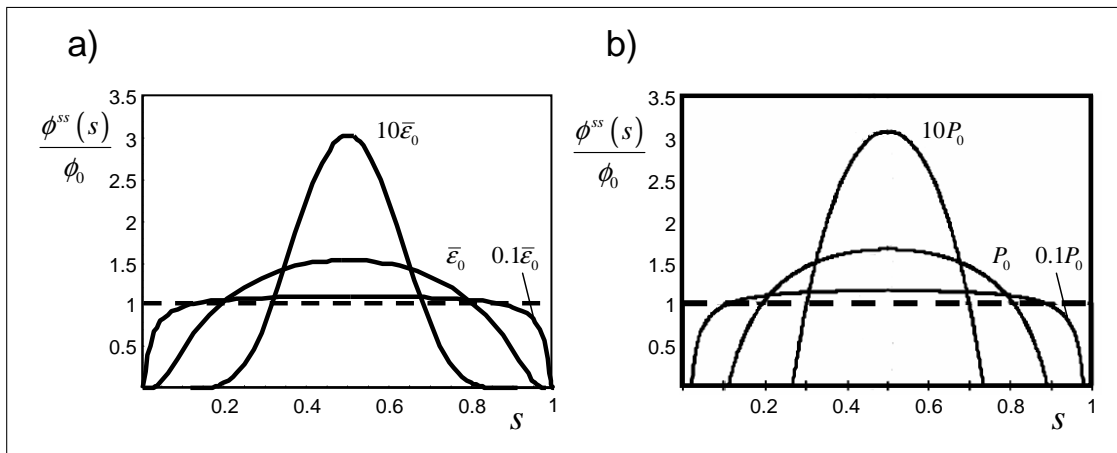


Figure 6.3: **Steady-state particle distribution of a dilute suspension.** **a)** Steady-state particle distribution with increasing $\bar{\epsilon}$. The suspension is dilute so that $3\phi_0 \ll \phi_{max}$, and no core develops. Notice the boundary layer that forms at the walls for small $\bar{\epsilon}$. **b)** Numerical solutions by Hudson [46] for the same geometry, but with a non-linear diffusion coefficient. His solutions are parameterized by a *Péclet* number P_0 analogous to $\bar{\epsilon}_0$. Hudson's solutions are unphysical and intersect the horizontal axis; only the positive part is shown. [Here, $\bar{\epsilon}_0 = 0.16$ and $P_0 = 1$.]

We are then able to construct the particle distribution for a suspension with a core,

$$\phi_{||}^{ss}(s) = \begin{cases} \phi_{\max} \exp \left[\int_{\frac{1}{2}-r_c}^s \frac{u_m^<(s') - u_m^<(\frac{1}{2}-r_c)}{D} ds' \right] & 0 \leq s \leq \frac{1}{2} - r_c \\ \phi_{\max} & \frac{1}{2} - r_c \leq s \leq \frac{1}{2} + r_c \\ \phi_{\max} \exp \left[\int_{\frac{1}{2}+r_c}^s \frac{u_m^>(s') - u_m^>(\frac{1}{2}+r_c)}{D} ds' \right] & \frac{1}{2} + r_c \leq s \leq 1. \end{cases}$$

Again, the width of the core must be determined by enforcing the conservation of mass, resulting in a transcendental equation that is solved numerically.

From (6.4) we are able to calculate the flow velocity in the direction of rotation,

$$u_{\theta}(r) = r \left(\frac{T}{2\pi h} \right) \int_{R_1}^r \frac{dr'}{\eta_{\phi}(r') r'^3},$$

or, more explicitly,

$$u_{\theta}(r) = r \left\{ \frac{\Omega \int_{R_1}^r \frac{dr'}{\eta_{\phi}(r') r'^3}}{\int_{R_1}^{R_2} \frac{dr'}{\eta_{\phi}(r') r'^3}} \right\},$$

where now,

$$\eta_{\phi}(r) = \eta_0 \left(1 - \frac{\phi_{||}^{ss} \left(\frac{R_1}{h} \left(\frac{r}{R_1} - 1 \right) \right)}{\phi_{\max}} \right)^{-T}.$$

The particle distribution and velocity profile of a concentrated suspension ($\phi_0 = 0.45$) are shown in Figure 6.4. The most significant difference between the steady-state particle distribution in tube and Couette flow is the particle density in the depleted layer near the walls. For tube flow, the particle density near the wall decreases continuously with increasing ε . For Couette flow, on the other hand, a boundary layer appears adjacent to the walls, and a region of pure solvent lubricates the flow for *all* $\bar{\varepsilon} > 0$. This singular behavior of the particle density distribution leads to a sharp decrease in the effective viscosity of concentrated suspensions, as we shall see. The velocity profile, Figure 6.4b, is linear for

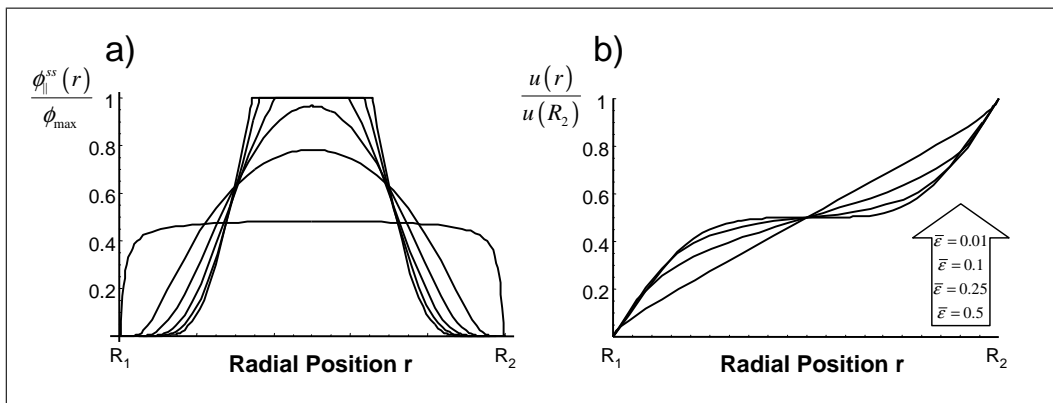


Figure 6.4: **Steady-state particle and velocity distribution of a concentrated suspension.** **a)** Steady-state particle distribution with increasing $\bar{\epsilon}$. The suspension is concentrated enough ($\phi_0 = 0.45$) that a core develops along the centerline at high $\bar{\epsilon}$. **b)** Velocity profile in the gap. For very large cylinder radii and small gap, the velocity profile of a *homogeneous* fluid is linear. The variable local viscosity due to the particle microstructure alters the flow field in an essential way, creating an inflection point at the centerline. (Here the gap width is 0.1% of the inner cylinder radius R_1 .)

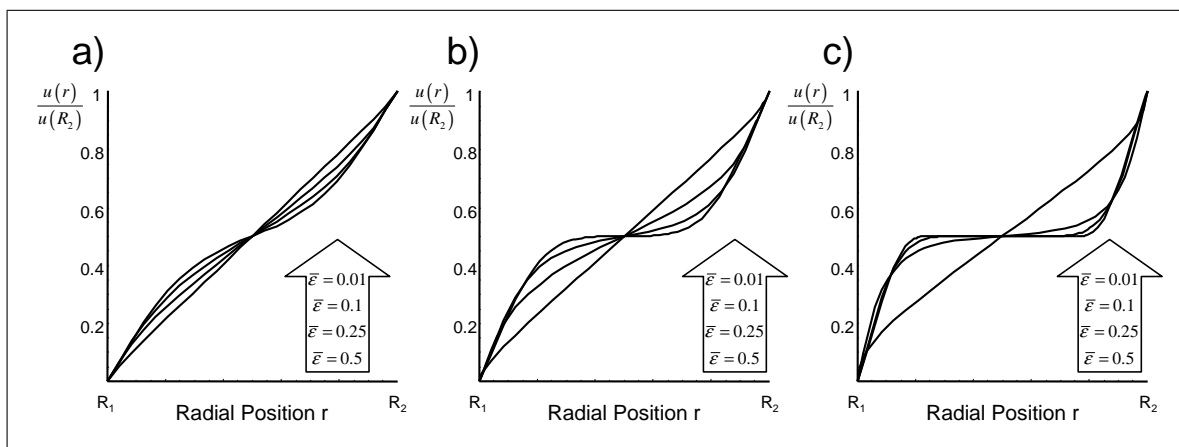


Figure 6.5: **Potential instability in Couette flow of concentrated suspensions.** **a)** For a comparatively dilute suspension ($\phi_0 = 0.25$), the flow is almost linear across the gap, although an inflection point is apparent at the centerline. **b)** For a more concentrated suspension ($\phi_0 = 0.45$), the velocity profile along the centerline is flattened. **c)** For a concentrated suspension ($\phi_0 = 0.65$), the velocity profile is very flat along most of the gap resembling an unstable shear layer flow.

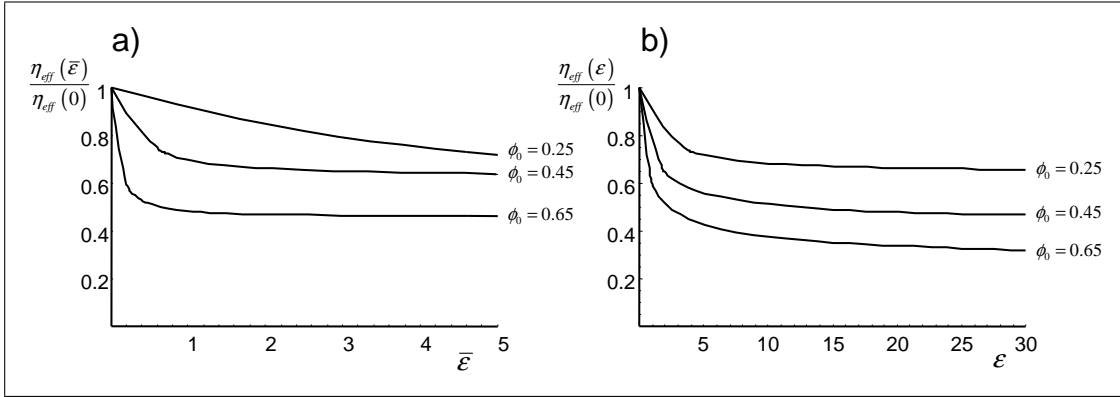


Figure 6.6: **Effective viscosity of Couette flow.** **a)** The effective viscosity of a Couette flow as a function of $\bar{\varepsilon}$ at three initial particle concentrations. **b)** The effective viscosity of the analogous tube Poiseuille flow.

small $\bar{\varepsilon}$, but as the particles migrate toward the center, the profile becomes flattened with an inflection point at the centerline.

An inflection point is often a warning sign that the flow may become unstable. Comparing the velocity profile at various particle concentrations (Figure 6.5), we see that at high particle density, even at very low shear rates, the particle migration leads to a flow profile that resembles an unstable shear-layer configuration³.

Using (6.5), we calculate the effective viscosity of Couette suspension flow (Figure 6.6). For the sake of comparison, we include the analogous plot for tube Poiseuille flow. There are three main points of interest. First, the core-annular limiting viscosity is *different* depending upon the viscometer. In tube flow, for $\phi_0 = 0.45$, the core-annular viscosity is about $\frac{1}{2}$ the zero-shear homogeneous viscosity; in Couette flow, the core-annular viscosity is only $\frac{3}{4}$ of the homogeneous viscosity.

Second, the Newtonian plateau of constant viscosity corresponding to fully developed core-annular flow occurs at a much lower $\bar{\varepsilon}$ than in the Poiseuille case. Even setting $\bar{\varepsilon} = \varepsilon$

³The migration of particles and the resultant flattening of the velocity profile along the centerline may help explain the observed instability of suspension Couette flow at low shear rates (see for example [37] or [61]). Analysis of the Taylor instability in suspension flow is outlined in Appendix C.

by choosing a gap width $d = 2\sqrt[3]{\frac{2R^2a}{3}}$ will not emulate suspension Poiseuille flow through a tube of radius R since the mechanisms of particle migration are so different.

Third, as ϕ_0 increases the effective viscosity of the Couette flow drops sharply, almost *discontinuously*, near $\bar{\varepsilon} = 0$. This is because of the boundary layer in the particle distribution function. The continuously decreasing particle density near the walls of a Poiseuille flow does not affect the observed viscosity in the same way. The qualitative behavior of suspension rheology is essentially different between the two viscometers. Since it is common practice to parameterize blood constitutive models using viscometer data, in the next section we consider the tenuous relationship such models have with physiological blood flow.

6.3 Trouble with constitutive models

For concreteness, we consider the recent work of El-Khatib and Damiano [31], although the problems that we discuss are not limited to that work, but rather appear anytime viscometer data is used to fix parameters in a constitutive model of suspension rheology.

Attempting to model pulsatile blood flow in a cylindrical tube, the authors propose a generalized Newtonian stress-tensor of the form

$$\tau = \eta \left(\frac{\partial u}{\partial r}, \phi_0 \right) \frac{\partial u}{\partial r}, \quad (6.7)$$

that depends upon the local shear rate $\frac{\partial u}{\partial r}$ and the resting cell volume fraction ϕ_0 . To fix the viscosity function $\eta \left(\frac{\partial u}{\partial r}, \phi_0 \right)$, they use the data of Chien and co-workers [22], obtained using a Couette viscometer and providing the observed viscosity over a range of shear rates from 0.01 to 500 s^{-1} . An algebraic fitting function is used, and they obtain (for $\phi_0 = 0.45$),

$$\eta(\dot{\gamma}) = 22.16 - \frac{17\dot{\gamma}^2}{\dot{\gamma}^2 + 8.5} + \frac{110.5}{90\dot{\gamma}^2 + 1}, \quad (6.8)$$

a plot of which is shown in Figure 6.7. This expression for η is substituted into the generalized stress-tensor, with $\dot{\gamma}$ replaced by $\frac{\partial u}{\partial r}$, and various consequences for blood flow are inferred from the subsequent analysis.

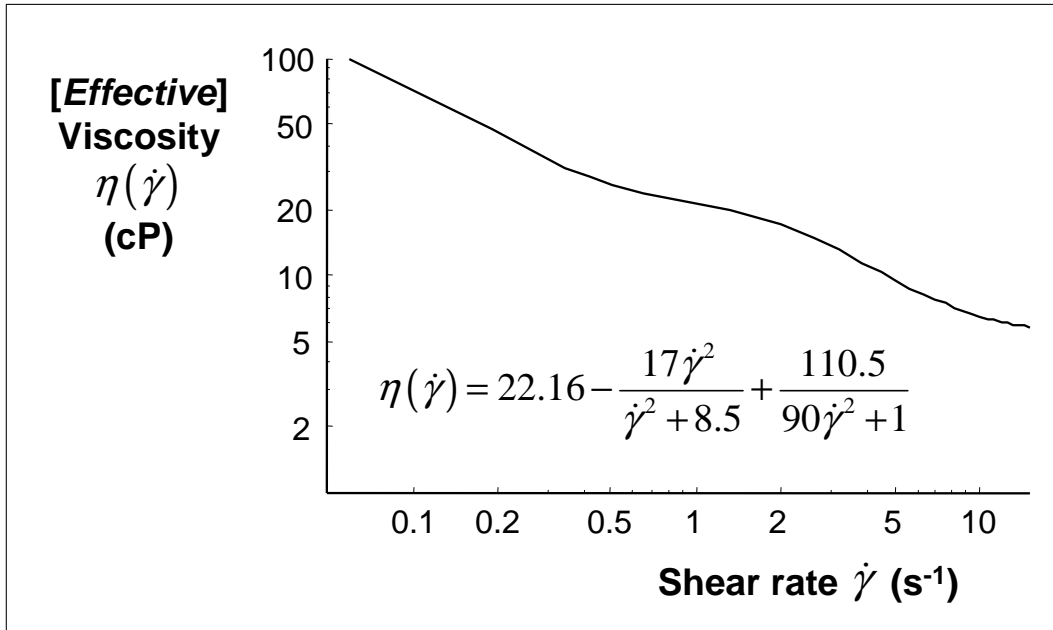


Figure 6.7: **Parameterization of a constitutive model.** The viscosity used by El-Khatib and Damiano [31] in a generalized Newtonian stress-tensor to model the pulsatile flow of blood in a vessel. There are two major problems: 1. The effective viscosity is *not* related to the local viscosity in a straightforward way. 2. The shear rate for suspension flow in a Couette viscometer is not constant in general, so the $\dot{\gamma}$ along the horizontal axis *does not* correspond to the $\frac{\partial u}{\partial r}$ appearing in the momentum conservation equation of tubular flow.

As has been pointed out by others [4, 5, 72], there is a deep problem with this approach – it is a problem of reification, of treating the words ‘viscosity’ and ‘shear rate’ as though they somehow correspond to intrinsic properties of a suspension. It is clear from the preceding section that in the data of Chien, the observed viscosity is an *effective bulk parameter that is a particular spatial average of the non-uniform local viscosity*. Moreover, the shear rate $\dot{\gamma}$ appearing along the horizontal axis is a measure of the rotation speed of the outer cylinder $\dot{\gamma} = \frac{\Omega R_2}{h}$ and has *nothing whatsoever to do with the local velocity gradient in tube flow*. That is to say, the η and $\dot{\gamma}$ in the fitting function (6.8) are *not* related to the η and $\frac{\partial u}{\partial r}$ appearing in the stress-tensor (6.7). The conclusion is that for a suspension, parameters in a constitutive equation cannot be fixed by bulk macroscopic measurements; the microscopic suspension properties must be taken into account.

As we have shown in this chapter, using the bulk behaviour of a suspension to characterize model parameters is fraught with difficulties, so in the next chapter, we return to the empirical diffusion coefficient $D(\phi_0, \varepsilon)$ and attempt to justify its form by considering the effect of microscopic particle velocity fluctuations on the averaged particle density distribution. Furthermore, we indicate how $D(\phi_0, \varepsilon)$ could be determined from microscopic information alone.

Chapter 7

Mean-field diffusion coefficient

In Chapter 5, to make contact with experimental data we chose an empirical expression for the diffusion coefficient $D(\varepsilon, \phi_0) = 1 - 3.77 \varepsilon \phi_0 + 3.7 \varepsilon^2 \phi_0^2$. As we have seen in Chapter 2, the microscopic transfer of momentum is represented on a macroscopic scale by the constitutive equation for the shear-stress tensor. In a similar way, microscopic fluctuations in the particle velocity due to collisions with solvent molecules and other particles are represented on a macroscopic scale by the diffusion coefficient. Here we shall attempt to justify the form of $D(\varepsilon, \phi_0)$ by explicitly considering the effect of collision-induced velocity fluctuations on the averaged particle density $\langle \phi \rangle$. We begin by introducing a fluctuating velocity field into the conservation equation for ϕ . We then estimate the conservation equation for the averaged process $\langle \phi \rangle$ using a closure scheme due to Bourret [8, 9]. In drawing the connection between the averaged conservation equation and the empirical diffusion coefficient $D(\varepsilon, \phi_0)$, we conclude with a heuristic approach to the problem which is in the spirit of the classical treatment of *turbulent* diffusion [63], although the physical mechanism underlying the diffusion in our case is much different.

7.1 Stochastic conservation equation for ϕ

Reconsider the particle conservation equation,

$$\frac{\partial \phi}{\partial t} = -\nabla \cdot (\phi \mathbf{u} - D_0 \nabla \phi)$$

with the diffusion coefficient D_0 given by the Einstein-Stokes formula, but now with shear-induced multi-particle collisions modeled as a zero-mean fluctuation term $\mathbf{v}(\mathbf{x}, t)$ in the convective velocity $\mathbf{u}(\mathbf{x}, t)$, which is a divergence-free field¹ of the type

$$\mathbf{u}(\mathbf{x}, t) = \mathbf{U}(\mathbf{x}) + \alpha \mathbf{v}(\mathbf{x}, t),$$

where $\mathbf{U}(\mathbf{x})$ is the mean migration velocity which we identify with the expression derived by Chan and Leal [18]. If we separate the right-hand side of the conservation equation into deterministic and random terms, then

$$\frac{\partial \phi}{\partial t} = -\mathbf{U} \cdot \nabla \phi + D_0 \nabla^2 \phi - \alpha \mathbf{v}(\mathbf{x}, t) \cdot \nabla \phi. \quad (7.1)$$

Or, in more concise notation,

$$\frac{\partial \phi}{\partial t} = L_0 \phi + \alpha L_1(t) \phi, \quad (7.2)$$

where $L_0 = [-\mathbf{U} \cdot \nabla + D_0 \nabla^2]$ is a deterministic linear operator, while $L_1(t) = [-\mathbf{v}(\mathbf{x}, t) \cdot \nabla]$ is stochastic, containing as it does the random velocity fluctuations $\mathbf{v}(t)$. We are after a closed *deterministic* equation governing the evolution of ϕ . We first consider a system of ordinary linear stochastic differential equations to illustrate the closure scheme, then with a Fourier transform we convert our stochastic conservation equation into a form amenable to approximation.

7.1.1 Bourret's approximation

For simplicity, consider a system of ordinary linear differential equations with random coefficients,

$$\frac{d\mathbf{y}}{dt} = \mathbf{A}_0 \mathbf{y} + \alpha \mathbf{A}_1(t) \mathbf{y}, \quad (7.3)$$

where \mathbf{A}_0 is a deterministic (time-invariant) real matrix and $\mathbf{A}_1(t)$ is a matrix of zero-mean, Gaussian distributed real random functions². The parameter α is small, and is a

¹We can be sure that the divergence $\frac{\partial v_j}{\partial x_j}$ exists in the mean-square sense as long as fluctuations in the velocity have a non-zero correlation length [27].

²For a discussion of random functions in general, see van Kampen's book [91]. For a discussion of stochastic differential equations in particular, see his review article [90].

measure of the strength of the fluctuations. The trajectory $\mathbf{y}(t)$ is a random function of time since it is characterized by a differential equation with random coefficients. Equations of this type are called *stochastic differential equations*, and the solution of the entire probability distribution of $\mathbf{y}(t)$ is usually impossible, so we must resort to methods of approximation. The most common of these involve exploitation of a small noise amplitude α and a short correlation time in the fluctuations: $\langle \mathbf{A}_1(t) \mathbf{A}_1(t + \tau) \rangle = 0$ for $\tau \gg \tau_c$ where τ_c is the *correlation time* of the fluctuations and the angled brackets denote an ensemble average. Suppose we are interested in only the *averaged* process $\langle \mathbf{y}(t) \rangle$, as is often the case in physical applications. Our goal is to derive from the stochastic equation (7.3) a *deterministic* evolution equation for $\langle \mathbf{y}(t) \rangle$. To that end, we introduce the so-called interaction representation, writing $\mathbf{y}(t)$ in terms of an auxiliary function $\mathbf{z}(t)$,

$$\mathbf{y}(t) = e^{t\mathbf{A}_0} \mathbf{z}(t),$$

so that from (7.3) the differential equation for $\mathbf{z}(t)$ is,

$$\frac{d\mathbf{z}}{dt} = \alpha e^{-t\mathbf{A}_0} \mathbf{A}_1(t) e^{t\mathbf{A}_0} \mathbf{z}(t),$$

or simply,

$$\frac{d\mathbf{z}}{dt} \equiv \alpha V(t) \mathbf{z}(t), \quad (7.4)$$

where we have defined the operator $V(t)$ by

$$V(t) = e^{-t\mathbf{A}_0} \mathbf{A}_1(t) e^{t\mathbf{A}_0}.$$

Solving the auxiliary equation (7.4) iteratively with initial condition $\mathbf{z}(0)$, we obtain a family of integral equations,

$$\mathbf{z}(t) = \mathbf{z}(0) + \alpha \int_0^t V(t') \mathbf{z}(t') dt',$$

$$\mathbf{z}(t) = \mathbf{z}(0) + \alpha \int_0^t V(t') \mathbf{z}(0) dt' + \alpha^2 \int_0^t \int_0^{t'} V(t') V(t'') \mathbf{z}(t'') dt'' dt'.$$

Taking the average of the second iterate, and using the fact that the fluctuating term $\mathbf{A}_1(t)$ has zero-mean,

$$\langle \mathbf{z}(t) \rangle = \mathbf{z}(0) + \alpha^2 \int_0^t \int_0^{t'} \langle V(t') V(t'') \mathbf{z}(t'') \rangle dt'' dt'. \quad (7.5)$$

The cross-correlation term $\langle V(t') V(t'') \mathbf{z}(t'') \rangle$ couples this equation to an infinite hierarchy of moment equations for $\mathbf{z}(t)$ in terms of the moments of the fluctuations. To make progress, we adopt the closure scheme of Bourret [90] to arrive at a closed equation for the evolution of the averaged process $\langle \mathbf{z}(t) \rangle$ in terms of only the first and second moments of the fluctuations. First, in the averaged integral equation (7.5) we make the change of variable $\tau = t' - t''$, to obtain

$$\langle \mathbf{z}(t) \rangle = \mathbf{z}(0) + \alpha^2 \int_0^t \int_0^{t'} \langle V(t') V(t' - \tau) \mathbf{z}(t' - \tau) \rangle d\tau dt'.$$

Next, taking the derivative, we arrive at a convolution equation characterizing the evolution of the averaged process

$$\frac{d}{dt} \langle \mathbf{z}(t) \rangle = \alpha^2 \int_0^t \langle V(t) V(t - \tau) \mathbf{z}(t - \tau) \rangle d\tau.$$

The correlation $\langle V(t) V(t - \tau) \rangle$ is, by assumption, narrowly peaked near $\tau = 0$. As a consequence, the triple product $\langle V(t) V(t - \tau) \mathbf{z}(t - \tau) \rangle$ will also be narrowly peaked around $\tau = 0$. Provided the magnitude of the noise is small ($\alpha \ll 1$), and the correlation time of the noise is short compared to the other time scales in the problem, the process $\mathbf{z}(t - \tau)$ will not significantly change over the interval $\tau \in [0, \tau_c]$, and we factor the triple correlation into a product of two correlations [8, 9] with the process $\mathbf{z}(t - \tau)$ evaluated at $\tau = 0$,

$$\frac{d}{dt} \langle \mathbf{z}(t) \rangle = \alpha^2 \int_0^t \langle V(t) V(t - \tau) \rangle \langle \mathbf{z}(t) \rangle d\tau. \quad (7.6)$$

The averaged process $\langle \mathbf{z}(t) \rangle$ is independent of τ , and will pass outside the integral to give

$$\frac{d}{dt} \langle \mathbf{z}(t) \rangle = \alpha^2 \left[\int_0^t \langle V(t) V(t-\tau) \rangle d\tau \right] \langle \mathbf{z}(t) \rangle.$$

Since the integrand is only correlated (hence non-zero) near $\tau = 0$, van Kampen [90] argues that the upper limit of integration is immaterial, and can be taken to infinity,

$$\frac{d}{dt} \langle \mathbf{z}(t) \rangle = \alpha^2 \left[\int_0^\infty \langle V(t) V(t-\tau) \rangle d\tau \right] \langle \mathbf{z}(t) \rangle.$$

This final equation is an evolution for the averaged process $\langle \mathbf{z}(t) \rangle$ that no longer depends upon previous values of $\mathbf{z}(t)$, and as such is an approximation of the convolution equation (7.6) by an evolution equation for a *Markov* process [54]. Re-writing the interaction representation back in terms of the original function $\mathbf{y}(t)$, we get *Bourret's approximation*,

$$\boxed{\frac{d}{dt} \langle \mathbf{y}(t) \rangle = \mathbf{A}_0 \langle \mathbf{y}(t) \rangle + \alpha^2 \left[\int_0^\infty \langle \mathbf{A}_1(t) e^{\tau \mathbf{A}_0} \mathbf{A}_1(t-\tau) \rangle e^{-\tau \mathbf{A}_0} d\tau \right] \langle \mathbf{y}(t) \rangle.} \quad (7.7)$$

With more careful statistical arguments [87, 90], it can be shown that the error incurred in this approximation is $O(\alpha^3 \tau_c^2)$, but higher-order corrections are not consistently calculated using the iteration procedure above – *i.e.*, we must use more sophisticated cumulant-expansion [90], or projection operator methods [87].

7.1.2 Conservation equation for $\langle \phi(\mathbf{x}, t) \rangle$

The generalization of Bourret's approximation from a system of ordinary differential equations to a partial differential equation is straightforward: we replace the matrices \mathbf{A}_0 and $\mathbf{A}_1(t)$ with the *linear operators* L_0 and $L_1(t)$ and get a result analogous to (7.7), namely

$$\frac{\partial}{\partial t} \langle \phi(\mathbf{x}, t) \rangle = L_0 \langle \phi(\mathbf{x}, t) \rangle + \alpha^2 \left[\int_0^\infty \langle L_1(t) e^{\tau L_0} L_1(t-\tau) \rangle e^{-\tau L_0} d\tau \right] \langle \phi(\mathbf{x}, t) \rangle. \quad (7.8)$$

To estimate the integrand, it is more convenient to work with the Fourier transform of the averaged equation. Direct evaluation of the transform is difficult, and so we repeat the derivation above with the Fourier transform of the stochastic conservation equation.

Since the cross-stream migration of the particle is primarily due to gradients in the shear rate and its behaviour is essentially unchanged if the walls are removed, we are justified in taking the Fourier transform of (7.2). We define the Fourier transform $\mathcal{F}\{\cdot\}$ as

$$\mathcal{F}\{f(\mathbf{x}, t)\} = \hat{f}(\mathbf{k}, t) = \int_{\mathbb{R}^3} e^{-i\mathbf{k}\cdot\mathbf{x}} f(\mathbf{x}, t) d\mathbf{x},$$

and the transformed stochastic conservation equation, written in terms of the vector components with summation over repeated indices implied, is written

$$\frac{\partial \hat{\phi}}{\partial t} = -k^2 D_0 \hat{\phi} - \mathcal{F}\left\{U_j \frac{\partial \phi}{\partial x_j}\right\} - \alpha \mathcal{F}\left\{v_j \frac{\partial \phi}{\partial x_j}\right\}.$$

In an unbounded domain, a product of functions in \mathbf{x} -space becomes a convolution in \mathbf{k} -space [48], so that

$$\begin{aligned} \mathcal{F}\left\{v_j \frac{\partial \phi}{\partial x_j}\right\} &= i \left(\hat{v}_j * k_j \hat{\phi}\right) = i \int_{\mathbb{R}^3} \hat{v}_j(\mathbf{k} - \mathbf{k}') k'_j \hat{\phi}(\mathbf{k}', t) d\mathbf{k}', \\ \mathcal{F}\left\{U_j \frac{\partial \phi}{\partial x_j}\right\} &= i \left(\hat{U}_j * k_j \hat{\phi}\right) = i \int_{\mathbb{R}^3} \hat{U}_j(\mathbf{k} - \mathbf{k}') k'_j \hat{\phi}(\mathbf{k}', t) d\mathbf{k}', \end{aligned}$$

where a factor of $(2\pi)^{-3}$ on the right-hand side has been suppressed to keep the notation as simple as possible. Introducing the shorthand for the transformed operators,

$$\hat{L}_0 \hat{\phi} = -k^2 D_0 \hat{\phi} - i \int_{\mathbb{R}^3} \hat{U}_j(\mathbf{k} - \mathbf{k}') k'_j \hat{\phi}(\mathbf{k}', t) d\mathbf{k}',$$

$$\alpha \hat{L}_1 \hat{\phi} = -i\alpha \int_{\mathbb{R}^3} \hat{v}_j(\mathbf{k} - \mathbf{k}') k'_j \hat{\phi}(\mathbf{k}', t) d\mathbf{k}',$$

we re-write the Fourier transform of the conservation equation concisely as

$$\frac{\partial \hat{\phi}}{\partial t} = \left(\hat{L}_0 + \alpha \hat{L}_1\right) \hat{\phi}, \tag{7.9}$$

where $\hat{L}_1(\mathbf{k}, t)$ is a random operator. As above, we introduce the interaction representation, writing $\hat{\phi}(\mathbf{k}, t)$ in terms of an auxiliary function $\hat{c}(\mathbf{k}, t)$,

$$\hat{\phi}(\mathbf{k}, t) = e^{t\hat{L}_0} \hat{c}(\mathbf{k}, t),$$

so that the differential equation for $\hat{c}(\mathbf{k}, t)$ is simply,

$$\frac{\partial \hat{c}}{\partial t} \equiv \alpha V(t) \hat{c}(\mathbf{k}, t), \quad (7.10)$$

where we have defined the operator $V(t)$ by

$$V(t) = e^{-t\hat{L}_0} \hat{L}_1(t) e^{t\hat{L}_0}.$$

Invoking Bourret's approximation as above, and re-writing the interaction representation back in terms of the original function $\hat{\phi}$, we find in analogy with (7.7)

$$\frac{d}{dt} \langle \hat{\phi}(\mathbf{k}, t) \rangle = \hat{L}_0 \langle \hat{\phi}(\mathbf{k}, t) \rangle + \alpha^2 \left[\int_0^\infty \langle \hat{L}_1(t) e^{\tau\hat{L}_0} \hat{L}_1(t-\tau) \rangle e^{-\tau\hat{L}_0} d\tau \right] \langle \hat{\phi}(\mathbf{k}, t) \rangle,$$

The integrand contains two exponentials of the differential operator \hat{L}_0 , making the integral difficult to evaluate in general. If, however, the characteristic time scale associated with \hat{L}_0 is long compared with the correlation time of the noise, we can take the leading order contribution of the exponential: $e^{\pm\tau\hat{L}_0} \approx \mathbf{1}$. The formal expansion of the exponential operator introduces secular terms since the time scale of \hat{L}_0 depends upon k , and therefore integration over all of k in the inverse Fourier transform will diverge. Physically, we see that this divergence is fictitious, and comes from adopting a continuum view of the suspension. In truth, the wave number cannot be made arbitrarily large since the suspension is composed of particles with finite spatial extension. We set k_{max} as the maximum allowable wave number, which is of the order of the inverse particle radius $k_{max} = O(\frac{1}{a})$. The size of the particles therefore sets a restriction upon the maximum allowable noise correlation time for the expansion of the exponential operator to be valid:

$$\tau_c \ll \left| \hat{L}_0^{-1} \right| \sim \min \left| \frac{a^2}{D_0}, \frac{R^3}{a\varepsilon D_0} \right|,$$

where $\frac{a^2}{D_0}$ is the time it takes for a particle to diffuse a distance a and $\frac{R^3}{a\varepsilon D_0}$ is the time it takes a particle to migrate a distance a carried by u_m . Another way to view the correlation time is as a time scale much longer than the time between solvent-particle collisions, but much shorter than the time it takes for a blood cell itself to move a macroscopic distance.

With the exponentials approximated by the unit matrix, the integrand is simplified to the auto-correlation of \hat{L}_1 alone,

$$\begin{aligned} & \left\langle \hat{L}_1(t) e^{\tau \hat{L}_0} \hat{L}_1(t - \tau) \right\rangle e^{-\tau \hat{L}_0} \approx \left\langle \hat{L}_1(t) \hat{L}_1(t - \tau) \right\rangle = \\ & = - \int \int_{\mathbb{R}^3} k'_j k''_l \langle \hat{v}_j(\mathbf{k} - \mathbf{k}', t) \hat{v}_l(\mathbf{k}' - \mathbf{k}'', t - \tau) \rangle d\mathbf{k}' d\mathbf{k}'' . \end{aligned}$$

The correlation of the Fourier-transform of the velocity fluctuations can be simplified if we re-write the complete expression as

$$\begin{aligned} & \langle \hat{v}_j(\mathbf{k} - \mathbf{k}', t) \hat{v}_l(\mathbf{k}' - \mathbf{k}'', t - \tau) \rangle = \\ & = \int \int_{\mathbb{R}^3} e^{-i(\mathbf{k} - \mathbf{k}') \cdot \mathbf{x}} e^{-i(\mathbf{k}' - \mathbf{k}'') \cdot (\mathbf{x} + \xi)} \langle v_j(\mathbf{x}, t) v_l(\mathbf{x} + \xi, t - \tau) \rangle d\xi d\mathbf{x} \\ & = \int \int_{\mathbb{R}^3} e^{-i(\mathbf{k} - \mathbf{k}'') \cdot \mathbf{x}} e^{-i(\mathbf{k}' - \mathbf{k}'') \cdot \xi} \langle v_j(\mathbf{x}, t) v_l(\mathbf{x} + \xi, t - \tau) \rangle d\xi d\mathbf{x} . \end{aligned}$$

We assume that $\mathbf{v}(\mathbf{x}, t)$ is *stationary* in space and time (*i.e.* the first two moments of \mathbf{v} are independent of \mathbf{x} and t). The auto-correlation is then a function of the spatial separation and time difference *only*,

$$\langle v_j(\mathbf{x}, t) v_l(\mathbf{x} + \xi, t - \tau) \rangle = \Gamma_{jl}(\xi, \tau) .$$

The assumption of stationarity will likewise simplify the auto-correlation of the Fourier transform of the velocity fluctuations,

$$\begin{aligned} & \langle \hat{v}_j(\mathbf{k} - \mathbf{k}', t) \hat{v}_l(\mathbf{k}' - \mathbf{k}'', t - \tau) \rangle = \\ & = \left[\int_{\mathbb{R}^3} e^{-i(\mathbf{k} - \mathbf{k}'') \cdot \mathbf{x}} d\mathbf{x} \right] \left[\int_{\mathbb{R}^3} e^{-i(\mathbf{k}' - \mathbf{k}'') \cdot \xi} \Gamma_{jl}(\xi, \tau) d\xi \right] \\ & = \delta(\mathbf{k} - \mathbf{k}'') \int_{\mathbb{R}^3} e^{-i(\mathbf{k}' - \mathbf{k}'') \cdot \xi} \Gamma_{jl}(\xi, \tau) d\xi \\ & \equiv \delta(\mathbf{k} - \mathbf{k}'') S_{jl}(\mathbf{k}' - \mathbf{k}'', \tau) , \end{aligned}$$

where the Fourier transform of the auto-correlation function $S_{jl}(\mathbf{k}' - \mathbf{k}'', \tau)$ is sometimes called the *power spectrum* or the *spectral density* of the velocity fluctuations [84]. Returning to the auto-correlation of the operator \hat{L}_1 , the stationarity assumption results in

$$\begin{aligned} \langle \hat{L}_1(t) \hat{L}_1(t - \tau) \rangle &= \\ &= - \iint_{\mathbb{R}^3} k'_j k''_l \delta(\mathbf{k} - \mathbf{k}'') S_{jl}(\mathbf{k}' - \mathbf{k}'', \tau) d\mathbf{k}' d\mathbf{k}'' \\ &= - \int_{\mathbb{R}^3} k'_j k_l S_{jl}(\mathbf{k}' - \mathbf{k}, \tau) d\mathbf{k}'. \end{aligned}$$

With a linear change of variable $\mathbf{q} = \mathbf{k}' - \mathbf{k}$, we write

$$\begin{aligned} \langle \hat{L}_1(t) \hat{L}_1(t - \tau) \rangle &= - \int_{\mathbb{R}^3} (k_j + q_j) k_l S_{jl}(\mathbf{q}, \tau) d\mathbf{q} \\ \langle \hat{L}_1(t) \hat{L}_1(t - \tau) \rangle &= -k_j k_l \int_{\mathbb{R}^3} S_{jl}(\mathbf{q}, \tau) d\mathbf{q} - k_l \int_{\mathbb{R}^3} q_j S_{jl}(\mathbf{q}, \tau) d\mathbf{q}. \end{aligned}$$

The power spectrum $S_{jl}(\mathbf{q}, \tau)$ is an *even* function of \mathbf{q} , so the second term on the right-hand side is *odd* in \mathbf{q} and will therefore vanish, leaving

$$\langle \hat{L}_1(t) \hat{L}_1(t - \tau) \rangle = -k_j k_l \int_{\mathbb{R}^3} S_{jl}(\mathbf{q}, \tau) d\mathbf{q}.$$

We define the mean-field diffusivity tensor as,

$$\tilde{D}_{jl} \equiv \int_0^\infty \int_{\mathbb{R}^3} S_{jl}(\mathbf{q}, \tau) d\mathbf{q} d\tau.$$

With substitution into the Fourier transform of the transport equation,

$$\frac{d}{dt} \langle \hat{\phi}(\mathbf{k}, t) \rangle = \hat{L}_0 \langle \hat{\phi}(\mathbf{k}, t) \rangle - \alpha^2 k_j k_l \tilde{D}_{jl} \langle \hat{\phi}(\mathbf{k}, t) \rangle.$$

Transforming back into the original \mathbf{x} -domain, the full averaged stochastic conservation equation, to $O(\alpha^3 \tau_c^2)$, is

$$\frac{\partial}{\partial t} \langle \phi(\mathbf{x}, t) \rangle = -\nabla \cdot \left(\mathbf{U}(\mathbf{x}) \langle \phi(\mathbf{x}, t) \rangle - \left(D_0 \mathbf{1} + \alpha^2 \tilde{\mathbf{D}} \right) \nabla \langle \phi(\mathbf{x}, t) \rangle \right), \quad (7.11)$$

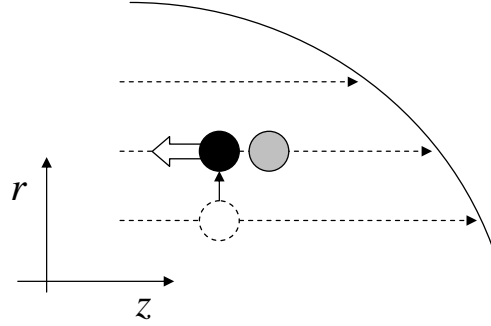


Figure 7.1: **Anisotropic diffusivity in tube flow.** A particle that moves upward ($v_r > 0$) with collide with particles moving more slowly to the right, thereby resulting in a *negative* velocity fluctuation in the z-direction ($v_z < 0$). The converse is true of a particle moving downward. Therefore, the correlation $\langle v_z(t)v_r(t - \tau) \rangle < 0$.

and $(D_0\mathbf{1} + \alpha^2\tilde{\mathbf{D}})$ is thus a *renormalized* diffusivity tensor that accounts for the fluctuations in the mean migration velocity due to particle-particle collisions. As in the constitutive equations discussed in Chapter 2, we have replaced the effect of many random, microscopic fluctuations with an averaged, or *mean-field*, parameter that emulates their effect on the macroscopic scale.

In our particular geometry, pressure driven tube flow, we expect the off-diagonal entries of $\tilde{\mathbf{D}}$ to be *negative* (Figure 7.1). To see this, assume a particle at position r is moving upward ($v_r > 0$) to position $r + dr$. There, the neighbouring particles are moving to the right more slowly, and impact with these slower moving particles results in a negative velocity fluctuation in the z-direction ($v_z < 0$). The converse is true of a particle moving downward ($v_r < 0$) to a region of faster moving particles. In that case, impact with neighbouring particles imparts a positive velocity in the z-direction ($v_z > 0$). In either case, we expect $\langle v_r v_z \rangle < 0$. The anisotropic component of the diffusivity tensor then has the form

$$\alpha^2\tilde{\mathbf{D}} = \begin{bmatrix} d_1 & -\beta \\ -\beta & d_2 \end{bmatrix},$$

where d_1 corresponds to the term dependent upon the v_r auto-correlation, d_2 corresponds to

the term dependent upon the v_z autocorrelation and d_1, d_2 and β are all positive constants. The eigenvalues for the correction matrix are,

$$\lambda_{\pm} = \frac{(d_1 + d_2)}{2} \pm \frac{\sqrt{4\beta^2 + (d_1 - d_2)^2}}{2},$$

with corresponding eigenvectors,

$$\begin{bmatrix} \lambda_- - d_1 \\ \beta \end{bmatrix}, \begin{bmatrix} \lambda_+ - d_1 \\ \beta \end{bmatrix}.$$

The projection of $\alpha^2 \tilde{\mathbf{D}}$ on the r -axis is found by first solving the linear equation,

$$c_1 \begin{bmatrix} \lambda_- - d_1 \\ \beta \end{bmatrix} + c_2 \begin{bmatrix} \lambda_+ - d_1 \\ \beta \end{bmatrix} = \begin{bmatrix} 1 \\ 0 \end{bmatrix},$$

to find

$$c_1 = -c_2 = \frac{\beta}{\sqrt{4\beta^2 + (d_1 - d_2)^2}},$$

and then forming the linear combination $c_1 \lambda_+ + c_2 \lambda_- = -\beta$. The projection of the full diffusivity tensor on the r -axis is thus,

$$D_0 \mathbf{1} + \alpha^2 \tilde{\mathbf{D}} \rightarrow D_0 + d_1 - \beta,$$

or, assuming the flow is rapid enough that $d_1 \ll \beta$,

$$D_0 \mathbf{1} + \alpha^2 \tilde{\mathbf{D}} \rightarrow D_0 - \beta.$$

To connect the formal expression $D_0 - \beta$ with the physical parameters appearing in the problem, and the empirical diffusion rate used in Chapter 5, we must examine the origin of the velocity fluctuations in more detail.

7.2 Connection to the empirical $D(\varepsilon, \phi_0)$

Fluctuations in the particle velocity arise from collisions with solvent molecules and with other particles. We assume the rapid collisions with solvent molecules to be adequately

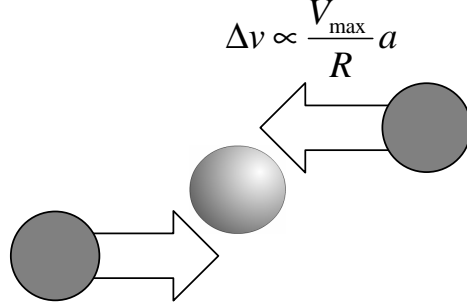


Figure 7.2: **Velocity fluctuations due to particle-particle collisions.** The change in velocity imparted to a particle after an elastic collision is proportional to the difference in the velocity before collision. The local flow velocity field changes roughly linearly near a particle, so that the velocity difference between particles scales as the mean shear rate $\frac{V_{max}}{R}$ multiplied by the particle radius a .

modeled by the Einstein-Stokes diffusion coefficient D_0 . The collisions with other particles are due to local gradients in the flow velocity field and happen on a much slower time scale, though they will carry more momentum. Very near the particle, the flow shear rate is approximately linear (Figure 7.2). If we assume the collisions are elastic, then the change in velocity imparted to a particle after collision is proportional to the velocity difference between particles *before* collision. The local shear gradient scales as $\frac{V_{max}}{R}$, so the velocity difference between particles scales as $\frac{V_{max}}{R} a$, and we write,

$$\sqrt{|\langle v_r v_z \rangle|^2} \propto \frac{V_{max}}{R} a. \quad (7.12)$$

Furthermore, the frequency of collisions depends upon the local particle number density. We therefore expect $|\langle v_r v_z \rangle|$ to be proportional to ϕ_0 ,

$$|\langle v_r v_z \rangle| \propto \phi_0. \quad (7.13)$$

Combining the square of (7.12) with (7.13), we find

$$|\langle v_r v_z \rangle| \propto V_{max}^2 \left(\frac{a}{R}\right)^2 \phi_0.$$

In terms of $\varepsilon \propto \frac{V_{\max}^2}{D_0} \left(\frac{a}{R}\right)^2$, we write the diffusion correction as,

$$\beta \propto |\langle v_r v_z \rangle| \propto D_0 \varepsilon \phi_0,$$

and the diffusion rate in the direction perpendicular to the walls is then,

$$\left(D_0 \mathbf{1} + \alpha^2 \tilde{\mathbf{D}}\right) \rightarrow D_0 - \beta = D_0 (1 - a_1 \varepsilon \phi_0),$$

with a_1 determined from experiments. From the data presented in Chapter 5, we find that $a_1 = 3.77$. Physically, we can understand the *reduction* in the rate of diffusion as the effect of fluctuations in directions other than that of the particle concentration gradient along \mathbf{e}_r . Fluctuations that carry the particle backward and forward along the tube or tangentially around the axis will slow the rate at which the particle moves away from the axis.

Finally, we note that the only other k^2 correction to the Fourier transform of the averaged conservation equation appears at $O(\alpha^4 \tau_c^3)$ [87], and it will be *positive*. As this term represents the contribution to the diffusion from triple collisions, it will be proportional to ϕ_0^2 . Further corrections will introduce higher powers of k therefore introducing third- and higher derivatives in the conservation equation. That being said, $D_0 (1 - a_1 \varepsilon \phi_0 + a_2 \varepsilon^2 \phi_0^2)$ is the best we can do with the closure scheme described above without fundamentally changing the form of the conservation equation for $\langle \phi(\mathbf{x}, t) \rangle$. In the next section, we cast further light upon the preceding derivation by adopting a semi-empirical approach akin to the classical treatment of turbulent diffusion [55, 63].

7.2.1 Semi-empirical derivation of the diffusion rate correction

As before, we assume the particle velocity is composed of a mean and fluctuating part: $u_j = \bar{u}_j + u'_j$, where $\langle u_j \rangle = \bar{u}_j$. The particle density distribution ϕ will subsequently contain an effect of the fluctuations. We assume this perturbation from the averaged particle density is small and in a similar way we write: $\phi = \bar{\phi} + \phi'$, where $\langle \phi \rangle = \bar{\phi}$. Substituting the fluctuating u_j and ϕ in the conservation equation, we have

$$\frac{\partial}{\partial t} (\bar{\phi} + \phi') + \frac{\partial}{\partial x_j} [(\bar{u}_j + u'_j) (\bar{\phi} + \phi')] = D_0 \frac{\partial^2 (\bar{\phi} + \phi')}{\partial x_j \partial x_j}.$$

Averaging the equation, using the fact that $\langle u'_j \rangle = \langle \phi' \rangle = 0$, we are left with

$$\frac{\partial \bar{\phi}}{\partial t} + \frac{\partial}{\partial x_j} (\bar{u}_j \bar{\phi}) = D_0 \frac{\partial^2 \bar{\phi}}{\partial x_j \partial x_j} - \frac{\partial}{\partial x_j} \langle u'_j \phi' \rangle,$$

(in analogy with (7.1)). Since $u'_j \sim \varepsilon a$ and $\phi' \sim \phi_0$, the correction term $\frac{\partial}{\partial x_j} \langle u'_j \phi' \rangle \sim \varepsilon \phi_0$ as we showed above. We have no obvious way to evaluate the cross-correlation directly, but we can identify it as a *flux* of particles J_j due to the velocity fluctuations, and write it as,

$$-\frac{\partial}{\partial x_j} \langle u'_j \phi' \rangle = -\frac{\partial}{\partial x_j} J_j.$$

As in any other phenomenological flux, we can assume the form

$$J_j = -K_{jl} \frac{\partial \bar{\phi}}{\partial x_l},$$

where in the study of turbulent diffusion, K_{jl} is called the *eddy diffusivity tensor*. In our case, there is no guarantee that the fluctuations will enhance the rate of diffusion. Indeed, from the reasoning above, we more properly write

$$J_j = K_{jl} \frac{\partial \bar{\phi}}{\partial x_l},$$

with the fluctuations working *against* the concentration gradient to slow the rate of diffusion. The full conservation equation, including our phenomenological diffusivity tensor, now reads

$$\frac{\partial \bar{\phi}}{\partial t} + \frac{\partial}{\partial x_j} (\bar{u}_j \bar{\phi}) = D_0 \frac{\partial^2 \bar{\phi}}{\partial x_j \partial x_j} - \frac{\partial}{\partial x_j} K_{jl} \frac{\partial \bar{\phi}}{\partial x_l},$$

that compares with (7.11) above. The comparative simplicity of this approach comes at a price, and in several ways it is inferior to the mean-field analysis of the previous section:

1. The semi-empirical method relies on a *linear relationship* between the particle distribution function and the perturbation, *i.e.* $\phi = \bar{\phi} + \phi'$. Higher-order corrections, for example the enhanced diffusion at $O(\varepsilon^2 \phi_0^2)$, cannot be derived in this way.
2. Parameterization of the cross-correlation $\langle u'_j \phi' \rangle$ involves hindsight physical arguments that really come from knowing what answer we want and adjusting the definition of the diffusivity tensor accordingly. As such, the effect of the fluctuations is determined from outside the model itself.

3. The cross-correlation $\langle u'_j \phi' \rangle$ expressed as $K_{jl} \frac{\partial \bar{\phi}}{\partial x_l}$ can only be determined by fitting to experimental data - there is no insight into the microscopic mechanism that gives rise to the enhanced diffusivity K_{jl} .

The advantage of the mean-field derivation of the diffusion coefficient is that, in principle, the correction is known once the power spectrum $S_{jl}(\mathbf{q}, \tau)$ of the fluctuations is known, and the power spectrum can be found experimentally or through numerical simulation. The shear-induced diffusion coefficient could then be estimated from microscopic information alone.

Chapter 8

Concluding remarks

The present model takes as its foundation the observation that in flow through small vessels, red blood cells align themselves along the axis. Using the results of Chan and Leal [18] describing the cross-stream migration of a single deformable droplet in tube flow, we develop a conservation equation for ϕ , the volume fraction distribution of red blood cells. At steady-state the distribution is Gaussian, characterized by the initial volume fraction ϕ_0 and a model *Péclet* number ε .

Choosing an empirical function relating ϕ to the local dynamic viscosity $\eta(r)$, and postulating a generalized Newtonian stress-tensor $\tau(r) = \eta(r)\frac{du}{dr}$, we solve the creeping flow equations for the suspension velocity $u(r)$. Equating the suspension flow rate to the flow rate of a homogeneous fluid we *define* an effective viscosity for the suspension, as measured by a capillary viscometer. Comparing with a variety of published data, we find that although simple, the model is versatile enough to capture the essential behaviour of blood flow through small tubes at physiological flow rates.

We then turn our attention to the rheology of a suspension in a co-axial cylindrical geometry, and we find *essentially* different behaviour from tube flow, casting doubt upon the practice of parameterizing *in vivo* models with Couette viscometer data.

Finally, we examine the effect of red blood cell – red blood cell collisions on the macroscopic diffusion rate by including a fluctuating velocity term in the conservation equation for ϕ . Invoking a closure scheme due to Bourret [8, 9], we find that the fluctuations add an anti-diffusion term to the macroscopic transport equation and that the form of the

empirical diffusion rate used in Chapter 5 is justified by these microscopic considerations.

The overarching theme of the dissertation is that for a suspension, the microscopic arrangement of particles in flow has important bearing on the overall rheology. The advantage of the present formulation lies in the simplicity of the central result - for tube flow, the particle distribution function can be determined exactly and it is a Gaussian parameterized by two variables ϕ_0 and ε . It is this simplicity that allows the physical consequences of the model to come through unobscured. Furthermore, the modularity of the development allows for possible model evolution. If the empirical viscosity term is found lacking, for example, it can be replaced by a more suitable expression without altering the structure of the argument. Likewise, additional flux terms including particle settling, electrostatic interactions with the walls, *etc.*, can be added to the conservation equation at the leisure of the investigator. The comparison with experimental data in Chapter 5 indicates that the present approach is worthwhile, although many interesting questions remain awaiting investigation.

The most restrictive approximation in the steady-state analysis is the assumption of zero Reynolds number, so we conclude with an outline of how the present model can be modified to include the effects of particle inertia.

8.1 Including the effect of inertia

As discussed in Chapters 4, the effective viscosity of blood decreases to a Newtonian plateau as the shear rate is increased, an effect called “shear-thinning.” At very high shear rates, however, the effective viscosity begins to increase (Figure 8.1). This region of “shear-thickening” corresponds to an observed decrease in the degree of blunting in the flow velocity profile (Figure 8.2). It seems reasonable to attribute this high flow-rate rheology to the effects of inertia on particle motion. We shall briefly outline how inertial effects are manifest in individual particle motion and how the present work can be modified to include these effects.

The non-linear momentum transport term in the Navier-Stokes equations will appear in the derivation of Einstein’s relation $\eta = \eta_0 \left(1 + \frac{5}{2}\phi\right)$ and in the expression for the migration

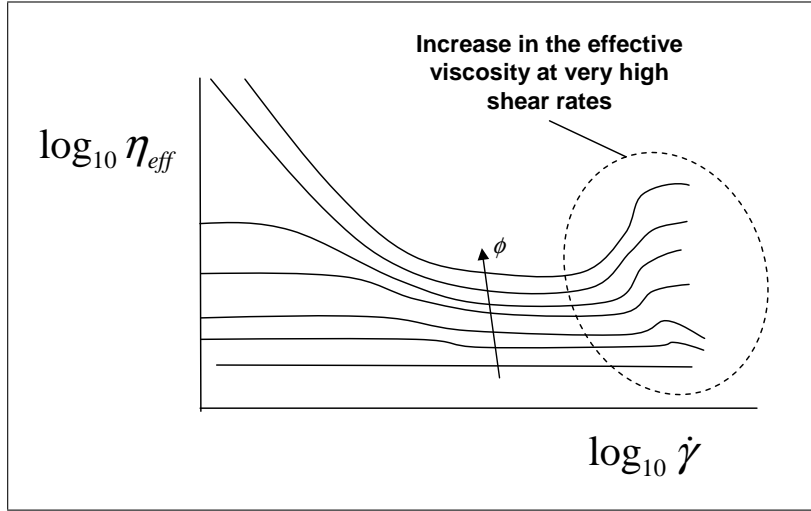


Figure 8.1: **High-Reynolds number rise in the effective viscosity.** The effective viscosity decreases to a plateau where core-annular flow is fully developed. At very high shear rates, however, a region of shear-thickening is observed. Redrawn after [45] and [81].

velocity $u_m(r)$. Here we restrict ourselves to small enough Reynolds number that the *overall* suspension is still adequately represented by the creeping flow equations.

Lin, Peery and Schowalter [60] have repeated the calculation for the effective viscosity of a homogeneous suspension as outlined in Chapter 2, but with the inertial term included in the flow equations. Their result for the observed viscosity increase in the dilute limit is,

$$\eta = \eta_0 \left(1 + \phi \left\{ \frac{5}{2} + 1.34 \text{Re}_p^{\frac{3}{2}} \right\} \right), \quad (8.1)$$

where $\text{Re}_p = \frac{V_m a^2 \rho}{R \eta_0}$ is the *particle* Reynolds number. In the notation of previous chapters, we include this correction by making the exponent T depend upon the Reynolds number in Roscoe's formula for the effective viscosity of a concentrated suspension,

$$\eta = \eta_0 \left(1 - \frac{\phi}{\phi_{\max}} \right)^{-T(\text{Re}_p)},$$

where $T(\text{Re}_p) = a + b \text{Re}_p^{\frac{3}{2}}$ and a and b are determined empirically. The expression suggests the observed shear-thickening, although (8.1) only properly applies to an unbounded ho-

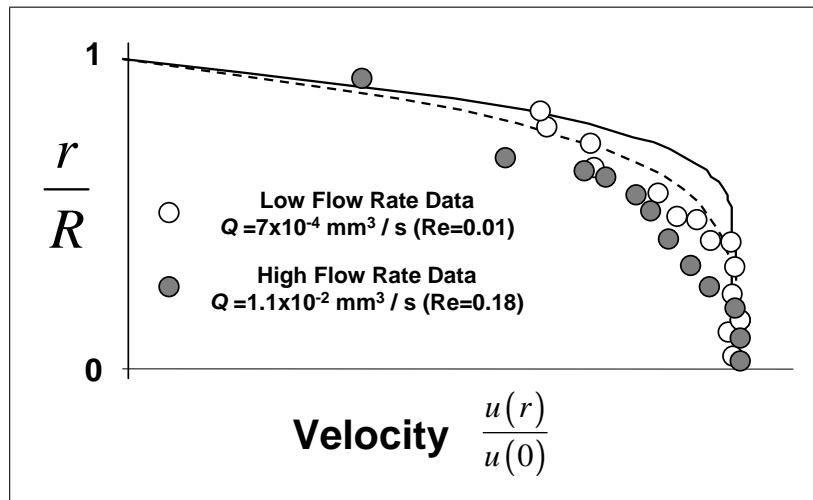


Figure 8.2: **Particle drift away from the axis at high Reynolds number.** The degree of blunting in the velocity profile of blood cell suspensions *decreases* at elevated flow rates. The present model fits the low Reynolds number data well (data - white circles, theory - dashed line). At high flow-rate, the velocity profile becomes *more* parabolic, and the theory over-estimates the width of the core region (data - filled circles, theory - solid line). The present model is reliable for $Re < 0.05$. Data from [38].

mogeneous suspension. As before, the particle distribution in the flow will no doubt play a major role in the observed rheology.

The modification of the migration velocity is straightforward. Provided the Reynolds number is not too large, the leading-order inertial corrections simply appear additively in the cross-stream migration velocity [56]. Serge and Silberberg [80] have observed the drift of rigid particles in a swift flow and have formulated a semi-empirical expression for the velocity [41],

$$u_{SS}(r) = 0.2\bar{u}\text{Re} \left(\frac{a}{R} \right)^3 \frac{r}{R} \left(1 - \frac{r}{r^*} \right),$$

where \bar{u} is the average velocity of the flow, Re is the *tube* Reynolds number and r^* is the equilibrium position the particle drifts toward, roughly $r^* = 0.6 r$. The velocity is quadratic in the radial position, and will tend to not only move particles away from the walls, but *away from the axis as well*. Thus, as the Reynolds number increases, the core is broken down with cells accumulating near $r = r^*$. As a result, the viscosity is more uniform across the tube and the velocity profile becomes more parabolic with a consequent increase in the observed viscosity.

Appendix A

Glossary

A.1 Glossary of Terms

Artery A vessel that moves blood away from the heart and toward the capillaries.

Capillary viscometer An instrument used to measure fluid viscosity. Fluid flows through a narrow tube, and from the relationship between the pressure drop along the tube and the flow rate, the viscosity is calculated (see Figure 6.1b on p. 71).

Cone-plate viscometer An instrument used to measure fluid viscosity. A cone with a very wide cone angle rotates above a flat plate. For a homogeneous Newtonian fluid, the shear rate across the gap is nearly constant (see Figure 6.1a on p. 71).

Constitutive equation An additional constraint on the relationship between the stress tensor τ , the hydrostatic pressure P and the fluid velocity field u that accounts for microscopic momentum transfer that is lost when the fluid behavior is approximated by the continuum field equations of fluid mechanics (see p. 29).

Core-annular flow A stratified flow with a high-viscosity core surrounded by a low-viscosity lubricating layer (see Figure 2.5 on p. 24).

Couette viscometer An instrument used to measure fluid viscosity. Two concentric cylinders with large radius and small gap width rotate relative to one another. For a

homogeneous Newtonian fluid, the shear rate across the gap is nearly constant (see Figure 6.1c on p. 71).

Erythrocyte A red blood cell (see Table 1.1 on p. 2).

Hematocrit The resting volume fraction of red blood cells. For healthy adults, the hematocrit lies between 0.4-0.45.

Microstructure Microscopic arrangement of blood cells in the macroscopic flow.

Newtonian fluid A fluid characterized by a stress tensor τ that is directly related to the deformation tensor through a *constant* η called the viscosity. For an *incompressible* fluid, the constitutive equation for a Newtonian fluid further simplifies to

$$\tau = \eta \left[\nabla \mathbf{u} + (\nabla \mathbf{u})^\dagger \right]$$

Plasma Watery yellow fluid that suspends the blood cells in whole blood.

Rheology The study of fluid flow properties - viscosity, flow velocity profiles, *etc.*

Rouleaux An end-to-end stacking of red blood cells (see Figure 1.4a on p. 7).

Serum Plasma with clotting proteins removed.

Thixotropy Time-dependence and hysteresis in the rheological properties of a fluid.

Vein A vessel that moves blood away from the capillaries and toward the heart.

Viscosity Proportionality constant relating the rate of strain to the stress in a Newtonian fluid. A measure of a fluid's resistance to flow.

A.2 Glossary of Symbols

A.2.1 Greek

	Description
α	Dimensionless small parameter.
δ	Dimensionless drop deformability.
ε	Model <i>Péclet</i> number. Dimensionless measure of the inhomogeneity in the particle distribution.
$\dot{\gamma}$	Shear rate in a Couette viscometer (s^{-1}).
κ	Viscosity ratio $\tilde{\eta}_0/\eta_0$.
ϕ	Blood cell volume fraction distribution.
ϕ_0	Initial volume fraction (<i>Hematocrit</i>).
ϕ_{max}	Volume fraction at maximum packing [$\phi_{max} = 1$].
ϕ^{ss}	Steady-state volume fraction distribution.
η_ϕ	Local suspension (dynamic) viscosity (Pa s).
η_0	Solvent (<i>Plasma</i>) viscosity [$\eta_0 = 1.2$ mPa s].
$\tilde{\eta}_0$	Droplet (<i>Blood cell</i>) interior viscosity (Pa s).
η_{eff}	Effective measured viscosity (Pa s).
ρ	Suspension density ($kg\ m^{-3}$).
ρ_0	Solvent (<i>Plasma</i>) density ($kg\ m^{-3}$).
σ	Interfacial tension [$\sigma = 1.24 \times 10^{-4}$ N m^{-1}].
τ	Local shear (deviatoric) stress tensor, formed by removing the pressure term from the full stress tensor S (Pa).
ω	Angular frequency of pulsatile pressure.

A.2.2 Arabic

a	Deformed red blood cell radius [$a = 3.5 \times 10^{-6}$ m].
$D(\varepsilon, \phi_0)$	Diffusion coefficient.
D_0	Einstein-Stokes diffusion constant.
G	Average shear rate in tube flow (s^{-1}) [$G = V_{max}/R$].

kT	Boltzmann energy [$kT = 4.28 \times 10^{-21}$ J at 37°C].
P	Hydrostatic pressure (Pa).
Q	Flow rate ($m^3 s^{-1}$).
r	Radial position (m).
\hat{r}	Dimensionless radial position [$\hat{r} = r/R$].
R	Tube (<i>Vessel</i>) radius (m).
Re	Tube Reynolds number [$Re = \frac{V_{\max} 2R\rho_0}{\eta_0}$].
R_ω	Strouhal number for pulsatile flow [$R_\omega = \frac{\omega R^2 \rho}{\eta_0}$].
S	The stress tensor (Pa) [$\mathbf{S} = -P\mathbf{1} + \eta [\nabla\mathbf{u} + (\nabla\mathbf{u})^\dagger]$].
t	Time (s).
\hat{t}	Dimensionless time [$\hat{t} = \frac{D}{R^2} t$].
T	Singularity exponent in the local viscosity [$T = 1.8$].
u	Suspension velocity ($m s^{-1}$).
u_m	Maximum, centerline suspension velocity ($m s^{-1}$).
V_{max}	Maximum, centerline velocity of Poiseuille flow ($m s^{-1}$).

Appendix B

Pulsatile velocity field

In the arteries of the body, the driving pressure is not constant, but rather pulses with each beat of the heart. In the small vessels, the amplitude of the pulsations is fairly small since most of the energy has been absorbed by the elastic walls of the large arteries. We model this pulsatile driving pressure as,

$$\frac{-dP}{dz} = \Delta P_0 (1 + \alpha \sin \omega t) \quad (\alpha \ll 1).$$

The time-dependent creeping flow equation then reads,

$$\rho_0 \frac{\partial u}{\partial t} = \Delta P_0 (1 + \alpha \sin \omega t) + \frac{1}{r} \frac{\partial}{\partial r} \left(r \eta(r) \frac{\partial u}{\partial r} \right).$$

Following Leal (p. 106 of [57]), we choose to non-dimensionalize the viscosity, velocity, distance and time as

$$\begin{aligned} \hat{\eta}(\hat{r}) &= \frac{\eta(\hat{r})}{\eta_0} \\ \hat{u} &= \frac{\eta_0}{\Delta P_0 R^2} u \\ \hat{r} &= \frac{r}{R} \\ \hat{t} &= t \frac{\eta_0 R^2}{\rho_0}. \end{aligned}$$

The creeping flow equation in non-dimensionalized form is then written as

$$\frac{\partial \hat{u}}{\partial \hat{t}} = (1 + \alpha \sin [R_\omega \hat{t}]) + \frac{1}{\hat{r}} \frac{\partial}{\partial \hat{r}} \left(\hat{r} \hat{\eta}(\hat{r}) \frac{\partial \hat{u}}{\partial \hat{r}} \right),$$

where we have defined the dimensionless parameter R_ω , sometimes called the *Strouhal number*, by the collection of variables

$$R_\omega = \frac{\omega \rho_0 R^2}{\eta_0}.$$

Dropping the hats, with the understanding that all variables are dimensionless, we write an analogous complex equation,

$$\frac{\partial \tilde{u}}{\partial t} = (i + \alpha e^{iR_\omega t}) + \frac{1}{r} \frac{\partial}{\partial r} \left(r \eta(r) \frac{\partial \tilde{u}}{\partial r} \right), \quad (\text{B.1})$$

so that our original solution satisfies the imaginary part of (B.1), *i.e.* $u = \Im m \{ \tilde{u} \}$. We seek a solution of the form

$$\tilde{u} = e^{iR_\omega t} G(r), \quad (\text{B.2})$$

valid for long times after the initial transients have died out. The complex equation (B.1), using the ansatz (B.2), becomes an ordinary differential equation for $G(r)$,

$$\frac{1}{r} \frac{d}{dr} \left(r \eta(r) \frac{dG(r)}{dr} \right) = iR_\omega G(r) + \tilde{P}_0,$$

$$G(1) = 0$$

$$G(0) < \infty$$

where $\tilde{P}_0 = -(ie^{-iR_\omega t} + \alpha)$ is a constant with respect to r . In the small vessels, the Strouhal number is very small, so we expand $G(r)$ as a perturbation expansion in R_ω ,

$$G(r) = G_0(r) + R_\omega G_1(r) + \dots$$

The zero-order equation,

$$\frac{1}{r} \frac{d}{dr} \left(r \eta(r) \frac{dG_0(r)}{dr} \right) = \tilde{P}_0,$$

$$G_0(1) = 0$$

$$G_0(0) < \infty$$

is identical to the equation solved in Chapter 4 with constant driving pressure (*cf.* (4.1)),

$$G_0(r) = -\frac{\tilde{P}_0}{2} \int_r^1 \frac{r_1 dr_1}{\eta(r_1)}.$$

The first-order equation is,

$$\frac{1}{r} \frac{d}{dr} \left(r\eta(r) \frac{dG_1(r)}{dr} \right) = iG_0(r) = -\frac{i\tilde{P}_0}{2} \int_r^1 \frac{r_1 dr_1}{\eta(r_1)}.$$

$$G_1(1) = 0$$

$$G_1(0) < \infty$$

Integrating twice, with application of the boundary conditions, the first-order solution is obtained,

$$G_1(r) = \frac{i\tilde{P}_0}{2} \int_r^1 \int_0^{r_1} \int_{r_2}^1 \frac{r_2 r_3 dr_3 dr_2 dr_1}{r_1 \eta(r_1) \eta(r_3)}$$

The long time solution of the complex problem is to $O(R_\omega^2)$,

$$\begin{aligned} \tilde{u} &= e^{iR_\omega t} G(r) \\ &= e^{iR_\omega t} (G_0 + R_\omega G_1) \\ &= -\frac{e^{iR_\omega t} \tilde{P}_0}{2} \left[\int_r^1 \frac{r_1 dr_1}{\eta(r_1)} \right] + \frac{ie^{iR_\omega t} \tilde{P}_0 R_\omega}{2} \left[\int_r^1 \int_0^{r_1} \int_{r_2}^1 \frac{r_2 r_3 dr_3 dr_2 dr_1}{r_1 \eta(r_1) \eta(r_3)} \right]. \end{aligned}$$

Taking the imaginary part, the long-time solution for the original velocity distribution with a pulsatile driving pressure is,

$$u = \frac{1}{2} \left\{ (1 + \alpha \sin [R_\omega t]) \left(\int_r^1 \frac{r_1 dr_1}{\eta(r_1)} \right) - \alpha R_\omega \cos [R_\omega t] \left(\int_r^1 \int_0^{r_1} \int_{r_2}^1 \frac{r_2 r_3 dr_3 dr_2 dr_1}{r_1 \eta(r_1) \eta(r_3)} \right) \right\}.$$

Or with the units partially restored and dimensionless variables written explicitly,

$$u(\hat{r}, t) = \frac{P_0}{2\eta_0} \left\{ (1 + \alpha \sin \omega t) \left[\int_{\hat{r}}^1 \frac{\eta_0 \hat{r}_1 d\hat{r}_1}{\eta_\phi(\hat{r}_1)} \right] - \alpha R_\omega \left[\int_{\hat{r}}^1 \int_0^{\hat{r}_1} \int_{\hat{r}_2}^1 \frac{\eta_0^2 \hat{r}_2 \hat{r}_3 d\hat{r}_3 d\hat{r}_2 d\hat{r}_1}{\hat{r}_1 \eta_\phi(\hat{r}_1) \eta_\phi(\hat{r}_3)} \right] \cos \omega t \right\}.$$

Appendix C

Stability of suspension Couette flow

Consider a fluid contained between two cylinders: an inner cylinder of radius R_1 and height h inside an outer cylinder of radius R_2 . The inner cylinder rotates with a constant speed $\Omega_1 rad s^{-1}$, while the outer cylinder rotates at $\Omega_2 rad s^{-1}$ (Figure C.1).

At steady-state, we write the torque T acting on a thin cylinder of fluid at a distance r from the axis of rotation as

$$T = \text{Stress} \times \text{Surface Area} \times \text{Length of the Lever Arm}$$

$$T = \tau_r (2\pi r h) r,$$

or, re-arranging for the shear-stress tensor τ_r ,

$$\tau_r = \frac{T}{2\pi r^2 h}. \quad (\text{C.1})$$

We denote by $\omega(r)$ the angular velocity of the fluid at r , so that the velocity of the fluid in the direction of rotation is $U_\theta = \omega r$, and the shear rate is given by,

$$\frac{dU_\theta}{dr} = r \frac{d\omega}{dr}.$$

Assuming a generalized Newtonian stress tensor $\tau_r = \eta_\phi(r) \frac{\partial U_\theta}{\partial r} = \eta_\phi(r) r \frac{d\omega}{dr}$, then from (C.1) it follows that

$$\frac{d\omega}{dr} = \left(\frac{T}{2\pi h} \right) \frac{1}{\eta_\phi(r) r^3}.$$

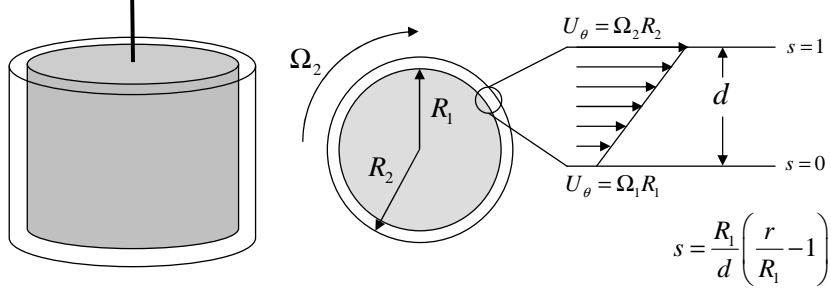


Figure C.1: **A Couette viscometer.** Two concentric cylinders rotate relative to one another. The ratio of the rotation speed to the resultant torque acting on the inner cylinder is determined by the viscosity of a *homogeneous* fluid. The gap width d is very small compared with the radii of the cylinders, and so the local background flow of a homogeneous fluid may be reasonably described by a linear shear flow between parallel plates.

This is a separable first-order differential equation and using the boundary conditions $\omega(R_1) = \Omega_1$ and $\omega(R_2) = \Omega_2$, we have

$$\omega(r) = \Omega_1 + \frac{(\Omega_2 - \Omega_1) \int_{R_1}^r \frac{dr'}{\eta_\phi(r')r'^3}}{\int_{R_1}^{R_2} \frac{dr'}{\eta_\phi(r')r'^3}}.$$

The steady velocity in the direction of rotation is then,

$$U_\theta(r) = r \left\{ \Omega_1 + \frac{(\Omega_2 - \Omega_1) \int_{R_1}^r \frac{dr'}{\eta_\phi(r')r'^3}}{\int_{R_1}^{R_2} \frac{dr'}{\eta_\phi(r')r'^3}} \right\}. \quad (\text{C.2})$$

In cylindrical coordinates the axisymmetric equations of motion with variable viscosity are,

$$\frac{D\tilde{u}_r}{Dt} - \frac{\tilde{u}_\theta^2}{r} = -\frac{1}{\rho} \frac{\partial \tilde{p}}{\partial r} + \nu(r) \left[\nabla^2 \tilde{u}_r - \frac{\tilde{u}_r}{r^2} \right] + 2 \frac{\partial \tilde{u}_r}{\partial r} \frac{\partial \nu}{\partial r},$$

$$\begin{aligned}\frac{D\tilde{u}_\theta}{Dt} + \frac{\tilde{u}_\theta\tilde{u}_r}{r} &= \nu(r) \left[\nabla^2\tilde{u}_\theta - \frac{\tilde{u}_\theta}{r^2} \right] + r \frac{\partial}{\partial r} \left(\frac{\tilde{u}_\theta}{r} \right) \frac{\partial\nu}{\partial r}, \\ \frac{D\tilde{u}_z}{Dt} &= -\frac{1}{\rho} \frac{\partial\tilde{p}}{\partial z} + \nu(r) \nabla^2\tilde{u}_z + \left[\frac{\partial\tilde{u}_z}{\partial z} + \frac{\partial\tilde{u}_r}{\partial r} \right] \frac{\partial\nu}{\partial r}, \\ \frac{\partial\tilde{u}_r}{\partial r} + \frac{\tilde{u}_r}{r} + \frac{\partial\tilde{u}_z}{\partial z} &= 0,\end{aligned}$$

where $\frac{D}{Dt} \equiv \frac{\partial}{\partial t} + \tilde{u}_r \frac{\partial}{\partial r} + \tilde{u}_z \frac{\partial}{\partial z}$, and $\nabla^2 \equiv \frac{\partial^2}{\partial r^2} + \frac{1}{r} \frac{\partial}{\partial r} + \frac{\partial^2}{\partial z^2}$. Following Taylor [85] (see also [19, 55]), we decompose the velocity and pressure into a background steady-state plus perturbation:

$$\tilde{\mathbf{u}} = \mathbf{U} + \mathbf{u}' \quad \frac{\tilde{p}}{\rho} = \frac{P}{\rho} + p', \quad (\text{C.3})$$

where $U_r = U_z = 0$ and U_θ is given by (C.2). To remain consistent with standard notation, we write: $U_\theta(r) \equiv V(r)$, then $\frac{1}{\rho} \frac{dP}{dr} = \frac{V^2}{r}$. Substituting (C.3) into the equations of motion, retaining only linear terms in the perturbation quantities,

$$\begin{aligned}\frac{\partial u'_r}{\partial t} - \frac{2V}{r} u'_\theta &= -\frac{\partial p'}{\partial r} + \nu(r) \left[\nabla^2 u'_r - \frac{u'_r}{r^2} \right] + 2 \frac{\partial u'_r}{\partial r} \frac{\partial\nu}{\partial r}, \\ \frac{\partial u'_\theta}{\partial t} + \left[\frac{dV}{dr} + \frac{V}{r} \right] u'_r &= \nu(r) \left[\nabla^2 u'_\theta - \frac{u'_\theta}{r^2} \right] + r \frac{\partial}{\partial r} \left(\frac{u'_\theta}{r} \right) \frac{\partial\nu}{\partial r}, \\ \frac{\partial u'_z}{\partial t} &= -\frac{\partial p'}{\partial z} + \nu(r) \nabla^2 u'_z + \left[\frac{\partial u'_z}{\partial z} + \frac{\partial u'_r}{\partial r} \right] \frac{\partial\nu}{\partial r},\end{aligned}$$

along with the incompressibility condition

$$\frac{\partial u'_r}{\partial r} + \frac{u'_r}{r} + \frac{\partial u'_z}{\partial z} = 0.$$

We seek solutions of the form

$$\{u'_r, u'_\theta, u'_z, p'\} = \{u(r), v(r), w(r), p(r)\} e^{\sigma t + ikz},$$

in order to characterize the growth of the normal modes. We assume a narrow gap, $\frac{d}{dr} + \frac{1}{r} \approx \frac{d}{dr}$, and a stationary marginal state, $\sigma = 0$. Under these conditions, the governing equations reduce to,

$$\nu(r) \left[D^2 + \left(2 \frac{\partial \ln \nu(r)}{\partial r} \right) D - k^2 \right] u + \left[\frac{2V}{r} \right] v = Dp, \quad (\text{C.4})$$

$$\nu(r) \left[D^2 + \frac{\partial \ln \nu(r)}{\partial r} D - k^2 \right] v - (DV) u = 0, \quad (\text{C.5})$$

$$\nu(r) \left[D^2 - k^2 + ik \frac{\partial \ln \nu(r)}{\partial r} \right] w + \left[\frac{\partial \nu(r)}{\partial r} D \right] u = ikp, \quad (\text{C.6})$$

$$-ikw = Du, \quad (\text{C.7})$$

where $D \equiv \frac{d}{dr}$ (*cf.* Chandrasekhar [19], eqs. 155-157 and 159 on p. 295). We introduce the new variable $r = sd + R_1$ where d is the gap width and non-dimensionalize the perturbation functions,

$$u \mapsto (\Omega_1 d) \left(\frac{2\Omega_1 d^2 a^2}{\nu_0} \right) u,$$

$$v \mapsto (\Omega_1 d) v,$$

$$w \mapsto (\Omega_1 d) w,$$

$$p \mapsto (2\Omega_1^2 d^2).$$

Likewise, the steady velocity and viscosity functions are nondimensionalized via,

$$V(r) \mapsto \frac{\Omega_1 (\mu - 1) d}{(1 - \eta)} \hat{V}(s),$$

$$\nu(r) \mapsto \nu_0 \hat{\nu}(s),$$

where $\mu = \frac{\Omega_2}{\Omega_1}$, $\eta = \frac{R_1}{R_2}$ (not to be confused with the dynamic viscosity) and $\nu_0 = \frac{\eta_0}{\rho} (1 - \phi_0)^{-T}$ - the kinematic viscosity of the *homogeneous* suspension. Identifying the dimensionless group,

$$T \equiv -\frac{2\Omega_1^2 (\mu - 1) d^4}{\nu_0^2 (1 - \eta)} = -\frac{2\Omega_1^2 (\mu - 1) (1 - \eta)^3 R_1^4}{\nu_0^2 \eta^4},$$

called the *Taylor number*, the governing equations are compactly written as,

$$D^3 u = a^2 Du + \frac{p}{\nu(r)}, \quad (\text{C.8})$$

$$D^2v = -Ta^2 \left[\frac{(DV)}{\hat{\nu}(s)} \right] u + a^2v - \left[\frac{\partial \ln \hat{\nu}(s)}{\partial s} \right] Dv, \quad (\text{C.9})$$

$$Dp = -[a^4\hat{\nu}(s)]u + \left[2a^2 \frac{\partial \hat{\nu}(s)}{\partial s} \right] Du + [a^2\hat{\nu}(s)]D^2u + [(\mu - 1)\hat{V}]v. \quad (\text{C.10})$$

where now $D \equiv \frac{d}{ds}$. In matrix form,

$$\frac{d}{ds} \begin{bmatrix} u \\ Du \\ D^2u \\ v \\ Dv \\ p \end{bmatrix} = \begin{bmatrix} 0 & 1 & 0 & 0 & 0 & 0 \\ 0 & 0 & 1 & 0 & 0 & 0 \\ 0 & a^2 & 0 & 0 & 0 & \frac{1}{\hat{\nu}(s)} \\ 0 & 0 & 0 & 0 & 1 & 0 \\ -T \frac{a^2 D\hat{V}}{\hat{\nu}(s)} & 0 & 0 & a^2 & -\frac{\partial \hat{\nu}(s)}{\partial s} & 0 \\ -a^4 \hat{\nu}(s) & 2a^2 \frac{\partial \hat{\nu}(s)}{\partial s} & a^2 \hat{\nu}(s) & (\mu - 1)\hat{V} & 0 & 0 \end{bmatrix} \begin{bmatrix} u \\ Du \\ D^2u \\ v \\ Dv \\ p \end{bmatrix}.$$

The steady velocity is written as a function of the variable local viscosity (see (C.2)),

$$V(r) = r \left\{ \Omega_1 + \frac{\Delta\Omega \int_{R_1}^r \frac{dr'}{\eta_\phi(r')r'^3}}{\int_{R_1}^{R_2} \frac{dr'}{\eta_\phi(r')r'^3}} \right\}.$$

Non-dimensionalizing, as the gap width vanishes ($d \rightarrow 0$ and $\eta \rightarrow 1$),

$$\hat{V}(s) = \frac{1}{(\mu - 1)} \left\{ 1 + \frac{(\mu - 1) \int_0^s \frac{ds'}{\hat{\eta}_\phi(s')}}{\int_0^1 \frac{ds'}{\hat{\eta}_\phi(s')}} \right\}.$$

For completeness, we write the derivative as well,

$$D\hat{V}(s) = \left[\hat{\eta}_\phi(s) \int_0^1 \frac{ds'}{\hat{\eta}_\phi(s')} \right]^{-1}.$$

To make contact with Chandrasekhar [19] and Kundu [55], we take the derivative of (C.8),

$$Dp = \hat{\nu}(s) \left\{ D^4u + \left[\frac{\partial \ln \hat{\nu}(s)}{\partial s} \right] D^3u - a^2 D^2u - a^2 \left[\frac{\partial \ln \hat{\nu}(s)}{\partial s} \right] Du \right\},$$

With substitution into (C.10), and some rearranging,

$$D^4u = \left[-\frac{\partial \ln \hat{\nu}(s)}{\partial s} D^3u + 2a^2 D^2u + 3a^2 \frac{\partial \ln \hat{\nu}(s)}{\partial s} Du - a^4u \right] + \frac{(\mu - 1)}{\hat{\nu}(s)} \hat{V}v.$$

We are then able to express the full mode equations in terms of u and v alone,

$$[D^2 - a^2]^2 u + \frac{\partial \ln \hat{\nu}(s)}{\partial s} [D^3 - 3a^2 D] u = \frac{(\mu - 1)}{\hat{\nu}(s)} \hat{V}v,$$

$$[D^2 - a^2] v + \frac{\partial \ln \hat{\nu}(s)}{\partial s} Dv = -T \frac{a^2}{\hat{\nu}(s)} (D\hat{V}) u.$$

In matrix form, the mode equations are

$$\frac{d}{ds} \begin{bmatrix} u \\ Du \\ D^2u \\ D^3u \\ v \\ Dv \end{bmatrix} = \begin{bmatrix} 0 & 1 & 0 & 0 & 0 & 0 \\ 0 & 0 & 1 & 0 & 0 & 0 \\ 0 & 0 & 0 & 1 & 0 & 0 \\ -a^4 & 3a^2 \frac{\partial \ln \hat{\nu}(s)}{\partial s} & 2a^2 & -\frac{\partial \ln \hat{\nu}(s)}{\partial s} & \frac{(\mu-1)\hat{V}}{\hat{\nu}(s)} & 0 \\ 0 & 0 & 0 & 0 & 0 & 1 \\ -T \frac{a^2 D\hat{V}}{\hat{\nu}(s)} & 0 & 0 & 0 & a^2 & -\frac{\partial \ln \hat{\nu}(s)}{\partial s} \end{bmatrix} \begin{bmatrix} u \\ Du \\ D^2u \\ D^3u \\ v \\ Dv \end{bmatrix},$$

along with the boundary conditions $u(0) = u(1) = 0$, $Du(0) = Du(1) = 0$, and $v(0) = v(1) = 0$. It remains to find the lowest critical Taylor number for which the eigenvalue a has positive real part – corresponding to exponential growth of the perturbation modes.

Bibliography

- [1] C. Alonso, A. R. Pries, O. Kiesslich, D. Lerche and P. Gaehtgens. Transient rheological behavior of blood in low-shear tube flow: velocity profiles and effective viscosity. *American Journal of Physiology*, 268:H25–H32, 1995.
- [2] M. Anand and K. R. Rajagopal. A shear-thinning viscoelastic fluid model for describing the flow of blood. *International Journal of Cardiovascular Medicine and Science*, 4:59–68, 2004.
- [3] M. Arakawa, T. Kondo and B. Tamamushi. Flow properties of microcapsule suspensions as a model of blood. *Biorheology*, 12:57–66, 1975.
- [4] H. A. Barnes. A review of the slip (wall depletion) of polymer solutions, emulsions and particle suspensions in viscometers: its cause, character, and cure. *Journal of Non-Newtonian Fluid Mechanics*, 56:221–251, 1995.
- [5] H. A. Barnes. Measuring the viscosity of large-particle (and flocculated) suspensions - a note on the necessary gap size of rotational viscometers. *Journal of Non-Newtonian Fluid Mechanics*, 94:213–217, 2000.
- [6] G. K. Batchelor. *An introduction to fluid dynamics*. Cambridge University Press, 1967.
- [7] G. K. Batchelor. Developments in microhydrodynamics. In W. T. Koiter, editor, *Theoretical and applied mechanics*, pages 33–35. North-Holland, 1976.
- [8] R. C. Bourret. Stochastically perturbed fields, with application to wave propagation in random fields. *Nuovo Cimento*, 26:1–31, 1962.

- [9] R. C. Bourret. Fictitious theory of dynamical systems with noisy parameters. *Canadian Journal of Physics*, 43:619–639, 1965.
- [10] H. Brenner. Dissipation of energy due to solid particles suspended in a viscous liquid. *Physics of Fluids*, 1:338–346, 1958.
- [11] F. P. Bretherton. The motion of rigid particles in a shear flow at low Reynolds number. *Journal of Fluid Mechanics*, 14:284–304, 1962.
- [12] H. C. Brinkman. The viscosity of concentrated suspensions and solutions. *Journal of Chemical Physics*, 20:571, 1952.
- [13] D. E. Brooks and G. V. F. Seaman. Role of mutual cellular repulsions in the rheology of concentrated red blood cell suspensions. In H. H. Hartert and A. L. Copley, editors, *Theoretical and clinical hemorheology*, pages 127–135. International Society of Hemorheology, Springer-Verlag, 1971.
- [14] A. C. Burton. *Physiology and biophysics of the circulation*. Year Book Medical Publishers, 1972.
- [15] C. G. Caro, T. J. Pedley, R. C. Schroter and W. A. Seed. *The mechanics of the circulation*. Oxford University Press, 1978.
- [16] R. Carr and G. R. Cokelet. Rheology of normal and hardened erythrocytes and their mixtures. *Journal of Rheology*, 25:67–82, 1981.
- [17] N. Casson. A flow equation for pigment-oil suspensions of the printing ink type. In C. C. Mill, editor, *Rheology of disperse systems*, pages 84–104. Pergamon Press, 1959.
- [18] P.C.-H. Chan and L. G. Leal. Motion of a deformable drop in a second-order fluid. *Journal of Fluid Mechanics*, 92:131–170, 1979.
- [19] S. Chandrasekhar. *Hydrodynamic and hydromagnetic stability*. Dover, 1961.
- [20] S. E. Charm and G. S. Kurland. *Blood flow and microcirculation*. John Wiley and Sons, Inc., 1974.

- [21] S. Chien. Shear dependence of effective cell volume as a determinant of blood viscosity. *Science*, 168:977–979, 1970.
- [22] S. Chien, S. Usami, H. M. Taylor, J. L. Lundberg and M. I. Gregersen. Effects of hematocrit and plasma proteins on human blood rheology at low shear rates. *Journal of Applied Physiology*, 21:81–87, 1966.
- [23] T. S. Chow. *Mesoscopic physics of complex materials*. Springer-Verlag, 2000.
- [24] E. G. D. Cohen and I. M. deSchepper. Transport properties of concentrated colloidal suspensions. In T. Kawakatsu K. Kawasaki and M. Tokuyama, editors, *Slow dynamics in condensed matter*, pages 359–369. American Institute of Physics, 1992.
- [25] B. Das, G. Enden and A. S. Popel. Stratified multiphase model for blood flow in a venular bifurcation. *Annals of Biomedical Engineering*, 25:135–153, 1997.
- [26] L. Dintenfass. Internal viscosity of the red cell and a blood viscosity equation. *Nature*, 219:956–958, 1968.
- [27] J. L. Doob. The Brownian movement and stochastic equations. *Annals of Mathematics*, 43:351–369, 1942.
- [28] P. L. Easthope and D. E. Brooks. A comparison of rheological constitutive functions for whole human-blood. *Biorheology*, 17:235–247, 1980.
- [29] A. Einstein. A new determination of molecular dimensions. *Annals der Physik*, 19:289, 1906.
- [30] A. Einstein. *Investigations on the theory of the Brownian movement*. Dover, 1956.
- [31] F. H. El-Khatib and E. R. Damiano. Linear and nonlinear analysis of pulsatile blood flow in a cylindrical tube. *Biorheology*, 40:503–522, 2003.
- [32] E. Evans, N. Mohandas and A. Leung. Static and dynamic rigidities of normal and sickle erythrocytes. *Journal of Clinical Investigation*, 73:477–488, 1984.

- [33] R. Fahraeus and T. Lindqvist. Viscosity of blood in narrow capillary tubes. *American Journal of Physiology*, 96:562–568, 1931.
- [34] N. A. Frankel and A. Acrivos. The constitutive equation for a dilute emulsion. *Journal of Fluid Mechanics*, 44:65–78, 1970.
- [35] F. J. Gauthier, H. L. Goldsmith, and S. G. Mason. Flow of suspensions through tubes. X. Liquid drops as models of erythrocytes. *Biorheology*, 9:205–224, 1972.
- [36] J. D. Goddard and C. Miller. Nonlinear effects in the rheology of dilute suspensions. *Journal of Fluid Mechanics*, 28:657–673, 1967.
- [37] J. D. Goddard and M. Alam. Shear-flow and material instabilities in particulate suspensions and granular media. *Particulate Science and Technology*, 17:69–96, 1999.
- [38] H. L. Goldsmith. The microrheology of human blood. *Microvascular Research*, 31:121–142, 1986.
- [39] H. L. Goldsmith and J. C. Marlow. Flow behavior of erythrocytes. II. Particle motions in concentrated suspensions of ghost cells. *Journal of Colloid and Interface Science*, 71:383–407, 1979.
- [40] H. L. Goldsmith and R. Skalak. Hemodynamics. *Annual Review of Fluid Mechanics*, 7:213–247, 1975.
- [41] H. L. Goldsmith and V. T. Turrito. Rheological aspects of thrombosis and haemostasis: Basic principles and applications. *Thrombosis and Haemostasis*, 55:415–435, 1986.
- [42] B. B. Gupta, K. M. Nigam and M. Y. Jaffrin. A three-layer semi-empirical model for flow of blood and other particulate suspensions through narrow tubes. *Journal of Biomechanical Engineering*, 104:129–135, 1981.
- [43] J. Happel and H. Brenner. *Low Reynolds number hydrodynamics*. Noordhoff, 1973. p. 85-88.
- [44] R. Herczynski and I. Pienkowska. Toward a statistical theory of suspension. *Annual Review of Fluid Mechanics*, 12:237–269, 1980.

- [45] R. L. Hoffman. Discontinuous and dilatant viscosity behavior in concentrated suspensions. I. Observation of a flow instability. *Journal of Rheology*, 16:155–173, 1972.
- [46] S. D. Hudson. Wall migration and shear-induced diffusion of fluid droplets in emulsions. *Physics of Fluids*, 15:1106–1113, 2003.
- [47] International committee for standardization in haematology (ICSH). ICSH - Guidelines for measurement of blood viscosity and erythrocyte deformability. *Clinical Hemorheology*, 6:439–453, 1986.
- [48] G. James. *Advanced modern engineering mathematics*. Pearson Prentice-Hall, 3rd edition, 2004. p. 380.
- [49] G. B. Jeffery. The motion of ellipsoidal particles immersed in a viscous fluid. *Proceedings of the Royal Society (London)*, 102A:161–179, 1922.
- [50] D. J. Jeffrey and A. Acrivos. The rheological properties of suspensions of rigid particles. *American Institute of Chemical Engineers Journal*, 22:417–432, 1976.
- [51] S. Kim and S. J. Karrila. *Microhydrodynamics: Principles and selected applications*. Butterworth, 1991.
- [52] M. R. King and D. T. Leighton. Measurement of shear-induced dispersion in a dilute emulsion. *Physics of Fluids*, 13:397–406, 2001.
- [53] I. M. Krieger. Rheology of monodisperse lattices. *Advances in Colloid and Interface Science*, 3:111–136, 1972.
- [54] R. Kubo. Stochastic Liouville equations. *Journal of Mathematical Physics*, 4:174–183, 1963.
- [55] P. K. Kundu and I. M. Cohen. *Fluid Mechanics*. Academic Press, 2nd edition, 2002.
- [56] L. G. Leal. Particle motions in a viscous fluid. *Annual Review of Fluid Mechanics*, 12:435–476, 1980.

- [57] L. G. Leal. *Laminar flow and convective transport processes*. Butterworth-Heinemann, 1992.
- [58] D. Leighton and A. Acrivos. The shear-induced migration of particles in concentrated suspensions. *Journal of Fluid Mechanics*, 181:415–439, 1987.
- [59] A. Lessner, J. Zahavi, A. Silberberg, E.H. Frei, and F. Dreyfus. The viscoelastic properties of whole blood. In H. H. Hartert and A. L. Copley, editors, *Theoretical and clinical hemorrheology*, pages 194–205. International Society of Hemorrheology, Springer-Verlag, 1971.
- [60] C. J. Lin, J. H. Peery and W. R. Schowalter. Simple shear flow around a rigid sphere: Inertial effects and suspension rheology. *Journal of Fluid Mechanics*, 44:1–17, 1970.
- [61] T. Loimer, A. Nir and R. Semiat. Shear-induced corrugation of free interfaces in concentrated suspensions. *Journal of Non-Newtonian Fluid Mechanics*, 102:115–134, 2002.
- [62] H. A. Lorentz. A general theorem concerning the motion of a viscous fluid and a few consequences derived from it. *Zittingsverslag Koninkl. Akad. van Wetensch. Amsterdam*, 5:168–174, 1896.
- [63] A. S. Monin and A. M. Yaglom. *Statistical fluid mechanics*, volume 1. MIT Press, 1987. p. 579.
- [64] T. Murata and T. W. Secomb. Effects of shear rate on rouleau formation in simple shear flow. *Biorheology*, 25:113–122, 1988.
- [65] J. G. Oldroyd. The elastic and viscous properties of emulsions and suspensions. *Proceedings of the Royal Society (London)*, 218A:122–132, 1953.
- [66] R. Owens. Private communication, May 2004.
- [67] S. Oyre, S. Ringgaard, S. Kozerke, W. P. Paaske, M. B. Scheidegger, P. Boesiger, and E. M. Pedersen. Quantitation [*sic*] of circumferential subpixel vessel wall position and wall shear stress by multiple sectorized three-dimensional paraboloid modeling of velocity encoded *cine*-MR. *Magnetic Resonance in Medicine*, 40:645–655, 1998.

- [68] R. Pal. Novel viscosity equations for emulsions of two immiscible liquids. *Journal of Rheology*, 45:509–520, 2001.
- [69] R. Pal. Rheology of concentrated suspensions of deformable elastic particles such as human erythrocytes. *Journal of Biomechanics*, 36:981–989, 2003.
- [70] W. M. Phillips and S. Deutsch. Toward a constitutive equation for blood. *Biorheology*, 12:383–389, 1975.
- [71] R. J. Phillips, R. C. Armstrong, R. A. Brown, A. L. Graham and J. R. Abbot. A constitutive equation for concentrated suspensions that accounts for shear-induced particle migration. *Physics of Fluids A*, 4:30–40, 1992.
- [72] Yu. N. Rabotnov. *Creep problem in structural members*. North-Holland, 1969. p. 113.
- [73] C. M. Rodkiewicz, P. Sinha and J. S. Kennedy. On the application of a constitutive equation for whole human blood. *Journal of Biomechanical Engineering*, 112:198–206, 1990.
- [74] K. Rohlf. *Theoretical studies on blood flow in small vessels*. Applied mathematics, University of Waterloo, 2002.
- [75] R. Roscoe. The viscosity of suspensions of rigid spheres. *British Journal of Applied Physics*, 3:267–269, 1952.
- [76] A. H. Sacks and E. G. Tickner. Laminar flow regimes for rigid sphere suspensions. In A. L. Copley, editor, *Hemorheology*, pages 277–303. Pergamon, 1968.
- [77] H. Schmid-Schonbein and R. Wells. Fluid drop-like transition of erythrocytes under shear. *Science*, 165 (3890):288–291, 1969.
- [78] G. W. Scott-Blair. The importance of the sigma phenomenon in the study of the flow of blood. *Rheologica Acta*, 1:123–126, 1958.
- [79] G. W. Scott-Blair. Basic equations for the flow of blood through an artificial capillary and for fibrin polymerization and softening. In A. L. Copley, editor, *Hemorheology*, pages 345–359. Pergamon, 1968.

- [80] G. Segre and A. Silberberg. Behaviour of macroscopic rigid spheres in poiseuille flow. Part 2 - Experimental results and interpretation. *Journal of Fluid Mechanics*, 14:136–157, 1962.
- [81] J. J. Stickel and R. L. Powell. Fluid mechanics and rheology of dense suspensions. *Annual Review of Fluid Mechanics*, 37:129–149, 2005.
- [82] Y. Sugii, S. Nishio and K. Okamoto. In vivo PIV measurement of red blood cell velocity field in microvessels considering mesentery motion. *Physiological Measurement*, 23:403–416, 2002.
- [83] N. Sun and D. De Kee. Simple shear, hysteresis and yield stress in biofluids. *Canadian Journal of Chemical Engineering*, 79:36–41, 2001.
- [84] V. I. Tatarski. *Wave propagation in a turbulent medium*. McGraw-Hill, 1961. Translated from the Russian by R. A. Silverman.
- [85] G. I. Taylor. Stability of a viscous liquid contained between two rotating cylinders. *Philosophical Transactions of the Royal Society (London)*, 223A:289–343, 1923.
- [86] G. I. Taylor. The viscosity of a fluid containing small drops of another fluid. *Proceedings of the Royal Society (London)*, 138A:41–48, 1932.
- [87] R. H. Terwiel. Projection operator method applied to stochastic linear differential equations. *Physica*, 74:248–265, 1974.
- [88] G. B. Thurston. Non-Newtonian viscosity of human blood: Flow-induced changes in microstructure. *Biorheology*, 31:179–192, 1994.
- [89] E. G. Tickner and A. H. Sacks. Engineering simulation of the viscous behavior of whole blood using suspensions of flexible particles. *Circulatory Research*, 25:389–400, 1969.
- [90] N. G. van Kampen. Stochastic differential equations. *Physics Reports*, 24:171–228, 1976.

- [91] N. G. van Kampen. *Stochastic processes in physics and chemistry*. North-Holland, 2003.
- [92] U. Windberger, A. Bartholovitsch, R. Plasenzotti, K. J. Korak and G. Heinze. Whole blood viscosity, plasma viscosity and erythrocyte aggregation in nine mammalian species: Reference values and comparison of data. *Experimental Physiology*, 88:431–440, 2003.